Contributions to Power Management and Dynamics Control in Hybrid Vehicles

D. Marcos

Contributions to Power Management and Dynamics Control in Hybrid Vehicles

Tesis

Para obtener el grado de Doctor
en la Escuela Superior de Ingeniería de la Universidad de Sevilla
David Marcos Rodríguez.
Ingeniero Industrial,
Máster en Automática, Robótica y Telemática,
nacido en Sevilla.

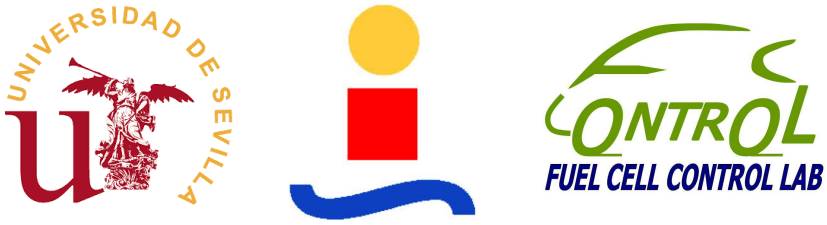

Esta tesis ha sido dirigida por:
Carlos Bordons Alba
catedrático en el departamento de Ingeniería de Sistemas y Automática de la Universidad de Sevilla.

Acknowledgements

—

I would like to thank the people I have had the pleasure to work with: Ignacio, Juanma, Luis, Silvia, Jose, Filiberto, Manuel, Ramón, Jorn, Antonio, Cristina, María, Ezequiel, Teodoro, Eduardo, Fernando, Felipe, Miguel, Marina, José Luis, Pablo, Daniel. And very specially to Carlos Montero, Elena González, Alejandro Oliva, Vicente Madero, Manuel Rodríguez, Juan Cabrera and Javier Pino. I feel very fortunate for having shared all this work and time with you.

-

I would like to thank Professors Eduardo Fernández and Miguel Ángel Ridao for all I have learnt from you, and to Professor Carlos Bordons for so many things, that would not fit this page.

-

Finally, I would like to thank my friends and family (by blood and in law) for asking, helping and supporting me. In special to my parents, for being a continuous guidance for me, and to my wife for her patience, comprehension, and love during all this time.

—

David Marcos Rodríguez,
Sevilla, July 2014.

Contents

List of Figures

List of Tables

Chapter 1

Introduction

1.1. Motivations

Road transportation has had a vital role in the history of humanity. Since the wheel invention, a large sort of vehicles have been used to transport goods, animals or people. In the 1880s, Karl Benz built the first vehicle driven by an Internal Combustion Engine (ICE). Thus, the first long trip (around 100 km, round trip) in an Internal Combustion Engine Vehicle (ICEV) was successfully done by Bertha Benz (Karl's wife) and their two children in 1888, demonstrating the feasibility of this kind of cars for personal transportation [78].

Today, the number of vehicles is continuously increasing, as shown in Figure 1.1, where the evolution of the number of vehicles in the world and in Europe is represented. Thus, in 2012 the motorization rate in Europe was of 449 vehicles per 1000 inhabitants, as pointed out by the Organisation Internationale des Constructeurs d'Automobiles (OICA) [87].

On the other hand, the excessive pollutant emissions have become an important problem. The OICA calculates that 16% of CO_2 human made emissions come from the road transport sector. In fact, road transport emissions are only exceeded by the electricity generation and heating sector, as shown in Figure 1.2 [88].

In fact, the first sector in final energy consumption in Europe is transport, as pointed out by the latest published data of the European Environment Agency (EEA), shown in

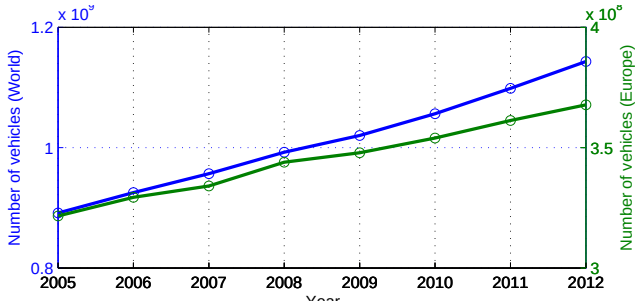

Figure 1.1: Number of vehicles in the world and in Europe.

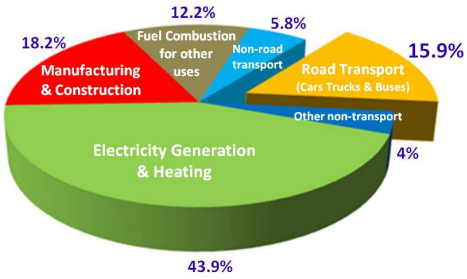

Figure 1.2: Human-made CO_2 emissions.

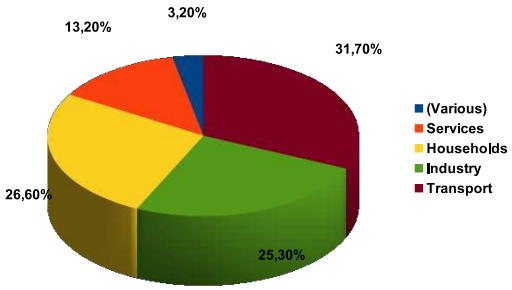

Figure 1.3: Total final energy consumption in Europe by sectors (2010).

Figure 1.3 [32]. Besides, this agency also provides information about the consumption of petroleum products, where the transportation sector represents 75.3% of the total.

Thus, one of the main goals of the new automotive technologies is precisely to reduce these numbers. To achieve that aim, the combustion engine is being substituted or complemented by electric motors. Meanwhile batteries, Ultra Capacitor (UC)s and FCs are becoming the new energy sources. Besides, the control systems of the vehicles are also becoming more sophisticated, playing a vital role in this change. On one hand, the mentioned technologies need these to operate. On the other hand, the controllers are programmed not just to enable the operation of the vehicle, but to minimize fuel consumption and pollutant emissions.

This is changing the patterns of consumption, and despite the fact that the average power of the new vehicles is increasing, the trend in fuel consumption is the opposite (Figures 1.4 and 1.5. Data taken from Association des Constructeurs Europens d'Automobiles (ACEA) [2]). This shows a higher concern about the pollution problem in customers and manufacturers. Therefore, vehicles of the future should reduce, or avoid if possible, their pollutant emissions, while they improve their performance in power, comfort and safety.

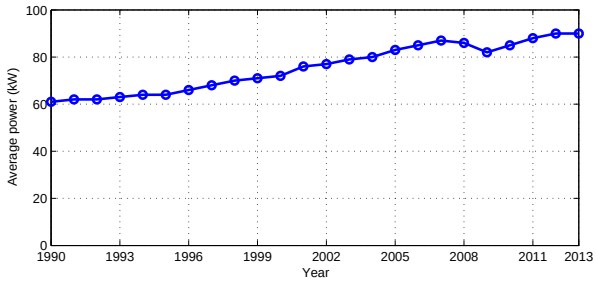

Figure 1.4: Average power of new registered cars.

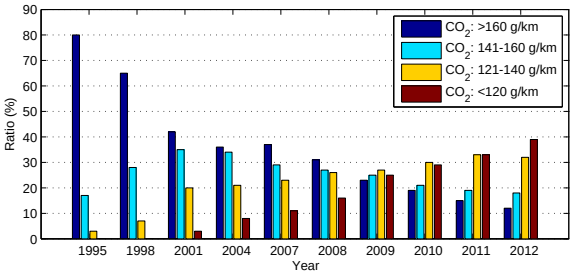

Figure 1.5: New passenger cars in the EU, by CO_2 emissions.

1.1.1. Control systems in cars

Overview

In the last decades, the development of electronics and automation hardware and software have changed our way of living. Electronics are present in almost all fields, nowadays. Evidently, a technified sector like the automotive could not obviate these advances. If a vehicle of the 1950s is compared to one manufactured today, it would have several important mechanical differences, and absolutely nothing to do in the electric/electronic system. The cars in the 50s had about 40 lines of cables, that were used just for the lights, the spark plugs and other basic devices. Today, all the systems have several sensors, a control unit, and hundreds of meters of cable supply and communicate these elements.

The first electronic advance in automotive was the injection system, in the 60s. This system sprays the fuel into the intake manifold. Even the original analog units used for the injection systems were more precise than the carburettors, achieving a better performance in power as well as in fuel consumption.

The second advance in automotive electronic was the Anti-lock Braking System (ABS) (1978) [18]. This was a huge milestone: this system did not improve the operation of the vehicle, but it actuated directly on the behaviour of the vehicle in case of an emergency brake. Today, this system is a standard.

In the following decades hundreds of electronic systems were introduced in the car. Some of them are just useful (power windows, power door locks), and some others have saved uncountable lives (airbag, seatbelt pretensioners...).

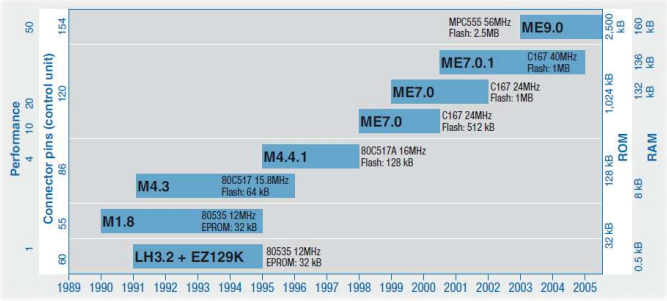

Figure 1.6: Development of ECUs.

Figure 1.7: Bosch MS 5.2 ECU.

ECU

Each of these systems needed a control unit that reads the signals from the sensors, and sends the orders to the corresponding actuators. These systems are named Electronic Control Units, and they are basically composed of a microcontroller, and different semiconductor memories (RAM, ROM) [18].

The number of ECUs has increased up to approximately 100 per vehicle nowadays.

The improvements in the electronics and semiconductors industry have made the ECUs evolute to a higher performance in a smaller size, increasing control possibilities in vehicles. Figure 1.6 shows a comparison between the Bosch ECUs from 1990 to 2007 [18].

Nowadays, the Bosch Motorsport MS5.2 ECU (Figure 1.7) wears a Freescale Semiconductor MPC5200B microcontroller, with a MPC603e series e300 core at 400 MHz [17, 39].

Sensors and actuators

As described in the definition, the ECU processes the data from sensors and sends the set points to actuators. As the ECUs, the units per vehicle of these devices have increased

Figure 1.8: Google autonomous vehicle.

significantly in the past few years.

The sensors convert a physical or chemical variable into an electric variable, while the actuators are the interface between the electric signal of the ECU and the actual process. These can be classified as:

- **Electromechanical actuators.**
- **Fluid-mechanical actuators.**
  - Hydraulic actuators.
  - Pneumatic actuators.
- **Electrical machines.**

Classification of the control systems in vehicles

The control systems of a car can be divided into three functional groups:

- **Systems that do not influence directly over the dynamics of the vehicle.**
- **Systems that help the driver.**
- **Systems that substitute the driver.**

The first group includes internal control systems (injectors [93, 122], etc.), safety systems (airbag, etc.) and several utilities (rear view mirrors positioning, alarms, etc.). On the other hand, the third group covers the systems that directly substitute the driver: in a certain task, like speed control (Adaptive Cruise Control (ACC)) [61, 110], in a manoeuvre (like the self parking vehicles [36], already available for some Volvo and Ford models) or even in the whole driving. Google has announced that at mid-2015 one hundred of their autonomous cars will be on the roads of the USA (Figure 1.8). These systems are not included in the field of study of this thesis.

The systems of the second group evaluate continuously the behaviour of the vehicle, actuating in case the car approaches to a physical limit.

Probably the best example of this group is the well-known Anti-lock Braking System. In the car without ABS, if the driver pushes violently the brake pedal, the wheels tend to get

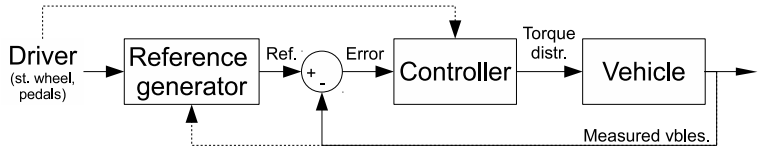

Figure 1.9: Control scheme of a four-motor vehicle.

locked. This reduces the grip of the tyres, and the driver looses control. The ABS system estimates the tyre-road friction, and it prevents locking by an actuator in each brake that can increase or reduce the braking force, avoiding wheels to get locked.

Similar to the ABS, the Traction-Control System (TCS) actuates over the engine and the brakes, in case any wheel looses grip during acceleration. Finally, the Electronic Stability Program (ESP) estimates the correct trajectory of the vehicle, by reading the data from the pedals and the steering wheel, and actuates in case the real behaviour differs excessively from the estimated. This system integrates ABS and TCS. There is a strong line of development about TCS [85, 126], and even over ABS, for more than 35 years [24, 109].

In the ICEVs, the ESP controls the torque in each wheel by actuating on the brakes, and communicating the main ECU a new set point for the engine torque. This implies that this system cannot be used continuously, due to the excessive wear of the brakes and the constraint of the minimum speed of the engine idle speed. Therefore, the program will only actuate in extreme situations, like emergency brakings or violent obstacle avoiding.

The actuation differs in an Electric Vehicle (EV) for these issues, due to the characteristics of the motors. In contrast with the ICEs, the electric motors:

- Have good response in all their working range (the vehicle does not need a gearbox).
- Have good response idle/in low speed (no idle speed needed).
- Can work as a motor or as a generator (regenerative braking). The negative and the positive torque has a similar degree of magnitude (depending on the energy storage system).

Moreover, the development of vehicles with one motor per wheel allows a better and simpler torque control in each wheel. The torque in each motor is completely independent from the rest. This allows a continuous torque distribution control that improves the behaviour of the vehicle in standard driving, as well as in extreme situations, where the mechanical brakes may also be used. The most common control scheme consists on a high level controller that generates the reference for the vehicle and a low level controller that sets the torque in each wheel for the vehicle to behave the closest to the reference [23, 33, 123, 124] (Figure 1.9).

The control of vehicles with in-hub wheels opens many challenging issues. Some of them are dealt within this thesis.

1.1.2. Hybrid cars

Definition of hybrid vehicle

All the ***road*** vehicles must have an energy source storage system. The most common source nowadays is a fossil fuel, like gasoline or diesel. A car is considered hybrid if it has more than one kind of energy source store, independently of its type [40, 44, 51]. These sources can be [51]:

- Fuel.
  - Fossil fuels (gasoline, diesel, LPG).
  - Hydrogen.
- Batteries.
- Ultra capacitors.
- Flywheels.
- Hydraulic accumulators.
- Pneumatic systems.

Motivations of the hybrid car

A hybrid car has more than one kind of energy source store. Therefore, the vehicle must have at least two systems that convert their corresponding stored energy into the final kinematic energy for the vehicle. This increments the complexity of the whole system and increases the weight of the system. These disadvantages are compensated by several advantages compared to the non hybrid cars. The most important of them are listed below [40, 51].

- **Downsize of the engine/motor.** A second device may supply the rest of the mechanical power. For example, the engine of a fossil fuel/batteries hybrid can be downsized, considering that an electric motor will actuate in case the driver demands more power than the limit of the engine. Another interpretation for this point is the upgrading of the vehicle. Thus, in the previous example, if the engine is powerful enough, the driver will have even an extra power source for any particular requirement. This would happen in hybrid race cars or in high end hybrid vehicles.
- **Regenerative braking.** Despite injection cars do not consume fuel while braking (unless the vehicle is not clutched), the fuel can never be recovered. On the contrary, if the car includes a rechargeable electric power source (batteries/ultracapacitors), part of the braking energy can be saved, instead of being wasted in friction braking.
- **Optimize the power distribution.** If the vehicle has more than one mover, the system has several options to reach the power set point of the driver, and that implies that the losses can be reduced by controlling the power supplied by each mover.

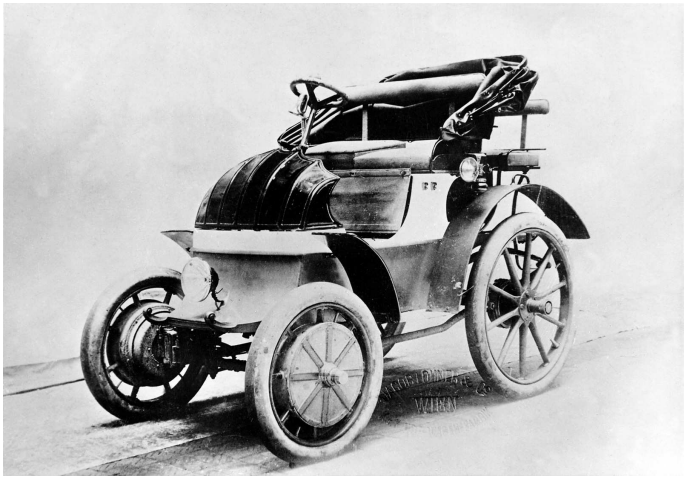

Figure 1.10: Lohner-Porsche Elektromobil.

- **Eliminate the idle fuel consumption.** Hybrid vehicles with electric motors do not need to keep the engine on when the car is idle, and that reduces significantly the fuel consumption, mainly in urban driving.

History

In the late 1800s and early 1900s, a person who wanted to acquire a car could choose between electric and internal combustion engine vehicles. This was equivalent to choosing between reliability or comfort. Thus, a failure in a ICEs was not an exceptional situation, while in the case of the electric cars, the charging process was too slow.

In 1901 Ferdinanz Porsche modified his *Lohner-Porsche Elektromobil* by adding an ICE, to recharge the batteries while the vehicle was being used, becoming the first hybrid car. In the same year some prototypes were shown in Paris Automobile Salon [40].

In the following decade, Woods designed his gas-electric car and introduced it into the market of the USA. The vehicle did not succeed due to its high price, compared with the non-hybrids, and in particular with the popular *Ford T*.

At that point, ICEs started to be more reliable and ICEVs became not the main but practically the only option, for approximately eight decades.

The first hybrid vehicle to be massively produced was the first generation of *Toyota Prius*, in 1997. The improvements in batteries as well as the possibility of having a powerful processor at a relatively low price have made the Prius to be a reliable vehicle. Despite its price being still higher than average vehicles of its segment, the lower consumption and the increasing environmental concerns have made Toyota Prius to be a relatively popular car.

The success of *Toyota Prius* has forced the car companies to focus on the fuel consumption problem. As a consequence, almost all the most important companies have at least one micro-hybrid vehicle (see Section 1.1.1).

Despite the fact that the number of hybrid cars is still low compared to the non-hybrids, it is increasing continuously. *Toyota Prius* is still the most popular hybrid car, but it is not

Figure 1.11: Ferrari Laferrari.

difficult to see the models of other companies (*Honda Insight*, *Ford Fusion Hybrid*, or Opel Ampera/Chevrolet Volt...) and the hybrid versions of other cars from Toyota (Auris and Yaris [111]) in the streets. Probably the most surprising hybrid car is Ferrari Laferrari: a limited edition 963 HP hybrid car (800 HP ICE, 163 HP Electric Motor (EM)) [67].

Hybridness has also reached the *Formula 1* competition. In 1999 the Federation Internationale de l'Automobile (FIA) authorised the teams the use of the Kinematic Energy Recovery System (KERS). This device stores energy when the vehicle is braking, and can be used by the driver as an extra power source in a certain moment of the race [57].

Classification

The first classification for hybrid vehicles is made regarding *how hybrid the vehicle is*. To measure this ratio, a new parameter is defined: the DoH. The DoH is the relation between the power of the batteries an the total power of the energy sources. Thus, Equations 1.1 and 1.2 show the expressions for a FCHV and an ICEHV respectively.

$$DoH = \frac{Battery\,power}{Battery\,power + Fuel\,cell\,power} \tag{1.1}$$

$$DoH = \frac{Battery\,power}{Battery\,power + ICE\,power} \tag{1.2}$$

The closest the DoH is to 0.5, the more hybrid the vehicle is. For instance, for the latter equation, if the DoH is close to 0, the car is almost an ICEV, while on the contrary, if the value is 1 it is a pure EV.

Regarding the DoH, the hybrid vehicles can be defined as:

- **Micro hybrids.** These are usually ICEVs with a higher battery capacity and different auxiliary devices (like an alternator that provides a higher regenerative braking power) that enables the possibility to stop the engine in idle situations (traffic jams, traffic lights, etc.). This will reduce the fuel consumption in urban driving. These cars

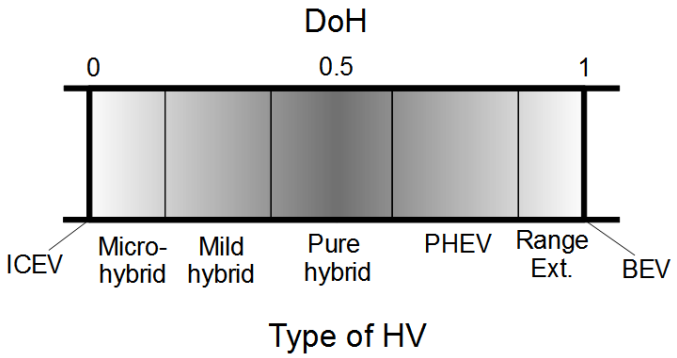

Figure 1.12: DoH for an ICEHV.

are becoming popular, and the new models of companies like BMW or Renault are including this specification.

- **Mild hybrids.** In these vehicles, the electric motor is able to supply an additional power to the powertrain, but it is not powerful enough to move the vehicle in acceptable conditions for themselves. Two examples of these hybrids are the Laferrari and the 2009-2014 Formula 1 cars mentioned in Section 1.1.2.
- **Full hybrid.** The DoH of these cars is close to 0.5. The importance of both power sources is similar, so they allow a great range of configurations (pure electric, boosted ICEHV, etc.). Toyota Prius could be an example of a full hybrid vehicle.
- **Plug-in Hybrid Electric Vehicles.** These vehicles are similar to the full hybrid, with the difference that it is possible to recharge the battery from the grid, like an EV. This characteristic, that the user may see as an extra option, changes the internal control of the power management due to the differences in price and in emissions between charging the batteries with the internal generator and charging the batteries from the grid. Chevrolet Volt is a commercial PHEV.
- **Extended-Range Electric Vehicle (EREV).** These are EVs with an auxiliary power unit which is activated in case an additional electric power is needed (to recharge the batteries or to track a power demand peak). The first hybrid vehicle (Lohner-Porsche Elektromobil) was one of this kind.

Figure 1.12 shows the different kinds of Hybrid Vehicle (HV)s versus the DoH. In the figure, the borders are illustrative. This classification is more functional than quantitative, so there are not predefined threshold that differentiate the types of cars.

Architectures of the hybrid cars

There are three basic architectures for hybrid cars: series, parallel and combined [51].

In the series architecture, the electric motor is coupled with the transmission, while the engine is only activated when the batteries need to be recharged or in a high demand of power. The advantage of this configuration is that the engine can recharge the batteries

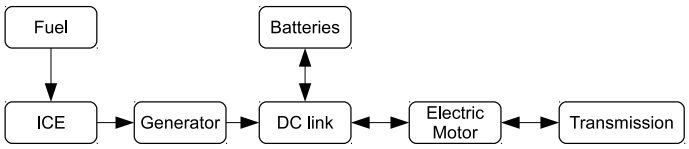

Figure 1.13: Series configuration.

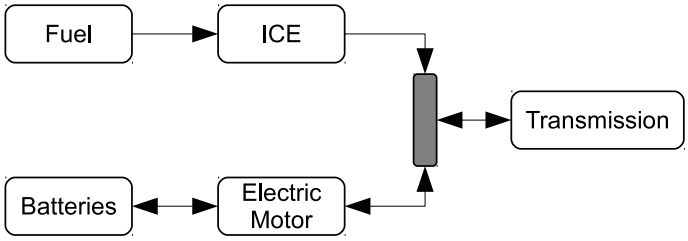

Figure 1.14: Parallel configuration.

when it is stationary and in low emissions conditions, reducing the consumption (Figure 1.13).

In the parallel configuration, both the engine and the motor can supply traction to the transmission, independently or at the same time (Figure 1.14).

Finally, the combined architecture uses one ICE and two electric motors. One is used as a tractive/regenerative braking motor and the second one as a generator, coupled with the engine (Figure 1.15).

A fourth kind of architecture would be the dual mode [44] in which the front an the rear powertrains are driven by two different power sources.

Fuel Cell Hybrid Vehicles

A FC is an electrochemical component that converts the chemical energy of a fuel into electric energy [72]. Like a battery, the fuel cell is composed on two electrodes: cathode and anode, separated by an electrolyte. However, fuel cells generate the electrical power from a fuel (hydrogen) and an oxidant (oxygen). The fuel cell consumes oxygen from the air and hydrogen from a tank (or any other supplier).

There are several types of FCs: alkaline, direct methanol, molten carbonate, etc. Table

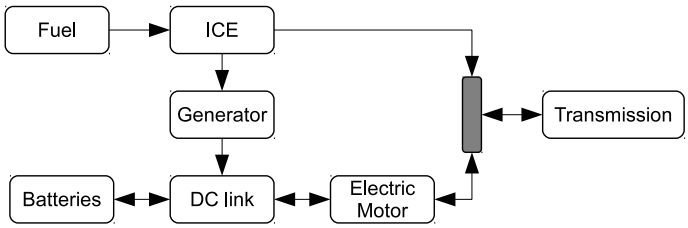

Figure 1.15: Combined configuration.

1.1 shows some types of FCs and their main characteristics [77].

Table 1.1: Most important types of FCs and their main characteristics.

Fuel Cell Type	Operating Temperature (^{o}C)	System Output (kW)	Electrical Efficiency (%)	Combined Heat and Power (CHP) (%) Efficiency (%)	Applications	Advantages
Alkaline (AFC)	90-100	10-100	60	>80	Military, Space	Cathode reaction Can use a variety of catalysts faster in alkaline electrolyte leads to higher performance
Phosphoric Acid (PAFC)	150-200	50-1000	>40	>85	Distributed generation	Higher overall efficiency with CHP Increased tolerance to impurities in hydrogen
Solid Oxide (SOFC)	600-1000	<1-3000	35-43	<90	Auxiliary power Electric utility Large distributed generation	High efficiency Fuel flexibility Can use a variety of catalysts Solid electrolyte reduces electrolyte management problems Suitable for CHP Hybrid/GT cycle
Molten Carbonate (MCFC)	600-700	<1-1000	45-47	>80	Electric utility Large distributed generation	High efficiency Fuel flexibility Can use a variety of catalysts Suitable for CHP
Polymer Electrolyte Membrane (PEM)	50-100	<1-250	53-58	70-90	Backup power Portable power Small distributed generation Transportation	Quick start-up Solid electrolyte reduces corrosion and electrolyte management problems Low temperature
Direct Methanol Fuel Cell (DMFC)	60-200	0.001-100	40	80	Replace batteries in mobiles, computers and other portable devices	Reduced cost due to absence of fuel reformer

In this thesis all the FCs used or simulated are PEMs, due to their power density and low operating temperature. The operation of a PEM FC is briefly explained in Figure 1.16.

In the anode, the hydrogen molecules are divided into protons (H^+) and electrons. The protons pass the membrane to the anode, while the electron travel through the external circuit, producing current to the anode. In the anode, these protons and electrons react with the oxygen, producing water:

$$2H^+ + 2e^- + \frac{1}{2}O_2 \rightarrow H_2O \tag{1.3}$$

Given the definitions of FC and HVs, it is easy to guess that a FCHV is a hybrid vehicle which energy source stores are batteries and hydrogen. The fuel cell can be used as the main or an auxiliary power source, depending on the degree of hybridness of the car. Both the batteries and the fuel cell supply electric energy, but while the first one can be ”recharged” instantaneously (refuelling), the latter has the possibility of recovering part of the braking energy (regenerative braking).

A comparison between hydrogen and gasoline is shown in Table 1.2.

Hydrogen has bigger lower and higher heating values. However, its density is much lower than the density of gasoline. What is more, gasoline is a liquid in ambient conditions, while hydrogen is a gas. The storage of this gas is specially complicated due to the small size of the H_2 molecule.

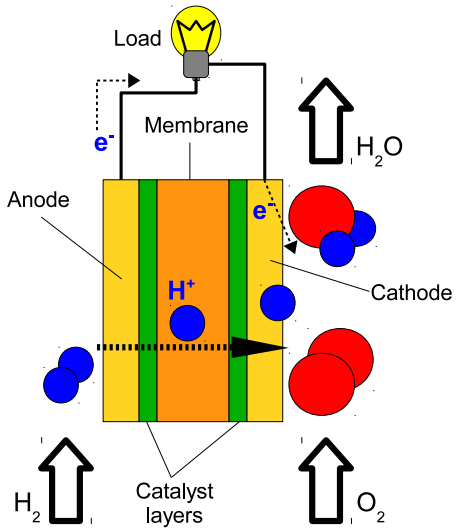

Figure 1.16: Operation of a PEM fuel cell.

On the other hand, the use of hydrogen instead of gasoline brings the advantage of using a fuel that can be obtained from renewable resources, unlike fossil fuels, which are limited. Moreover, the only product of the chemical reaction in the FC is water, which is far from being a pollutant. Therefore, Fuel Cell Vehicle (FCV)s are considered Zero Emission Vehicle (ZEV)s, and that is their main advantage. Even when the vehicle does not produce any harmful compound, if the production of hydrogen implied pollutant emissions, there would not be a big difference with the use of fossil fuels. Despite the fact that this is not studied in this thesis, it is important to show that there is an important open line of

Table 1.2: Comparison of fuel data for hydrogen and gasoline.

	Hydrogen	Gasoline
Molecular weight (g/mol)	2.016	107
Boiling point (K)	13.308	310-478
Vapor density at normal conditions (g/m3)	84	4400
Liquid density (kg/m3)	70.8	700
Higher heating value (MJ/kg)	141.86	48
Lower heating value (MJ/kg)	119.93	43.5
Gas constant (J/kg/K)	4124	78.0
Flammability limit in air (vol. %)	4.0-75	1.0-7.6
Detonation limit in air (vol. %)	18.3-59.0	1.1-3.3
Auto-ignition temperature (K)	858	501-744
Adiabatic flame temperature in air (K)	2318	2470
Flame front speed in air (cm/s)	≈ 300	37-43

Figure 1.17: Toyota FCV.

development about hydrogen production using renewable resources. Some of them are the reforming of glycerol under different catalysts [27, 116], bio-butanol [20], or from tar from biomass pyrolysis [70]. There are also researches about the convenience of one or other renewable method for different zones [105].

In the last two decades, a great number of automotive companies have developed FCVs, trying different degrees of hybridness, from pure FCV to pure hybrid or range extenders, and several hydrogen storage scenarios (gaseous, liquid, metal hydride, methanol...). Some examples of prototypes are the Daimler Necar series, the Opel HydroGen3 series, GM Provoq and Hy-Wire, Ford Focus FCV Hybrid and HySeries edge , Nissan X-Trail FCV, Citaro bus, Mazda Demio FCEV, Honda FCX, Mitsubishi SX4-FCV, Fiat Panda, etc. [5, 51].

Toyota has developed its own fuel cells as well as a 70 *MPa* compressed hydrogen storage system [112]. After more than twenty years of research [113], the company will launch the *FCV* model next year(Figure 1.17). In fact, 2015 has always been considered as a milestone for FCVs market production.

Power management in HVs

Since hybrid vehicles have more than one energy source store, there must be a controller that manages the flow of power from each device. Thus, the 1901 *Lohner-Porsche Elektromobil* had a simple system that implemented the power management algorithm, that consisted on three operational modes [40]. In the first one, the battery was connected only to the motor. In the second mode, the battery was connected only to the generator. In the third mode, the motor was short circuited to act as a brake. Note that the last mode is a 0% efficiency regenerative braking.

Nowadays the embedded controllers allow an advanced control of the flows of power. This brings the option of choosing an optimal operational mode in which a certain goal is achieved, which is usually the lowest fuel consumption, considering the constrains of the system and the driver requirements. In [70], Li describes this list of problems that an ICEHV has to manage:

- Have the ICE work on the optimal operating points.
- Minimize ICE dynamics.

- Optimize ICE operation speed
- Minimize ICE turn on/off times.
- Optimally manage the SOC of the batteries.
- Optimize power distribution.
- Follow zero emissions policy, in certain situations (tunnels, etc.).
- Optimally control Hybrid Electric Vehicle (HEV) transmission system.

A great number of control strategies have been used for power management in ICEHVs and HEVs: optimal control [4, 25, 64], neural networks [12], heuristic algorithms [26, 49] or Model Predictive Control (MPC) [16]. In a HEV the controller must keep the SOC between certain limits, or closed to its initial state.

On the contrary, in the case of a PHEV the batteries can be discharged until their security limit. The controller should administrate this stored energy in order to minimize the equivalent consumption. This makes the controllers use different strategies, like the Charge Depleting - Charge Sustaining (CD-CS), in which the car behaves like a Battery-powered Electric Vehicle (BEV) until the batteries reach a threshold (Charge Depleting, CD), after which the controller keeps the SOC in the minimum level (Charge Sustaining, CS). In contrast, the "blended mode" distributes the energy of the batteries along the cycle, depending on the driver requirements and the optimal operational points of the devices.

These strategies can be implemented with different control algorithms, mainly Equivalent Consumption Minimization Strategy (ECMS) [107, 115] and heuristic. A comparison between CD-CS and blended modes is presented in [121], while in [104] nine PHEV controllers are compared in terms of performance, fuel consumption and computational performance.

In the case of the FCHVs, not only different controllers are being studied (fuzzy [52, 86], MPC [15, 80], etc.), but also different vehicle sizes [41, 106] or power sources [41, 82], even involving external power devices [114].

The power management is the main issue for a HV. However, the conversion from ICEVs to HVs brings another kind of difficulties. Thus, in an ICEV the residual heat of the cooling system of the engine was the heating source for the HVAC, while the compressor of the air conditioning system was powered by the engine, which was always active, even if the vehicle was idle. As seen in this subsection, not all the hybrids vehicles have an ICE, and in case they do, it is not always active. Therefore, the HVAC needs to be redesigned in order to fit the new characteristics of the vehicle.

Moreover, this issue is coupled with the power management problem. In the ICEV, the heating system did not consume any additional power (it was fed by residual heat), and a clutch connected or disconnected the compressor of the ACS from the motor depending on the temperature. In the case of the HVs, the heat must be produced, and the compressor is driven by an electric motor. This affects not only to consumption, as in the case of the ICEVs, but also to power management, due to the high consumption of the HVAC.

This thesis studies several HVs in terms of power management and HVAC consumption. These HVs are of different types (range extenders, and a PHEV), different power sources (batteries, fossil fuel, hydrogen) and different architectures (series, combined).

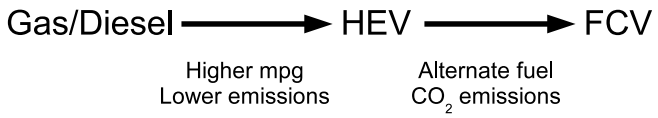

Figure 1.18: Energy sources in future automobiles.

Future

At present time, most of the automobiles in the world are ICEVs. However, there are several signs of a big change coming in the sector. The success of Toyota Prius is pushing the rest of the companies to hybridness or other alternatives, like the BEVs (Peugeot Ion, Renault Twizzy, etc.) or micro hybrids. Actually, the latter option is already included by default in all the models of several important companies. It is not easy to predict how the car of the future will be. But it is known that fossil fuels reservoirs are limited, so the present scenario will not be valid in the far future. Substituting the ICEs is not an option.

The ICEHVs can be considered as the first step of this process, as they do not have a complete dependency on fossil fuels. In [40], it is assumed that future vehicles will be driven by fuel cells (Figure 1.18).

Perhaps it is too soon to predict what the car of the future will be like. However, it is very significant that the most important motor companies are researching about this energy source, and the first commercial vehicles are about to be released. Maybe in some years a new technology will arrive, or batteries will solve their charging time problem and become the future energy source for vehicles. But, at the moment, fuel cells seem to be the best option for the future, while ICEHVs represent the present.

In any case (ICEHV, FCV or EV), the role of control systems will become **vital** in the future. New features, like autonomous driving or coordination with the traffic control centre or with other vehicles will be based on a control platform; while the solutions to the main issues (dynamics control, HVAC and power management) will have to evolute with the cars and be adapted to the nature of the own vehicles.

1.2. Goals

As exposed in Section 1.1.1, the importance of control systems in the cars is increasing, specially since the hybrid and electric cars have become a real option. This thesis will deal with some of the most important aspects of control for the HVs nowadays: power management, HVAC and dynamics control.

The power management is a need in HVs. This issue will be covered in this thesis by a MPC and a rule-based control strategy for three HVs with different configurations, degrees of hybridness and power sources: a range extender FCHV, a pure hybrid FCV and a ICE PHEV.

Regarding the HVAC issue, in this thesis the influence of the HVAC system over a HV will be address. Thus, a thermal model of a vehicle and a ACS model will be developed and integrated into the models of the power systems of a FCHV and a ICE PHEV to calculate the differences in performance and consumption in both vehicles when the HVAC system is

active.

Finally, a complete mechanical model of a four in-wheel independent driving vehicle will be presented and validated. Moreover, two differential torque controllers will be designed and implemented to improve the performance of the vehicle in normal driving.

In summary, the goal of this thesis is to cover the main issues of control in three kinds of vehicles: ICE PHEVs, FCHVs and four in-wheel independent driving vehicles, that represent the main trends for vehicles in the short and medium term.

1.3. Thesis overview

This thesis is organized as follows:

- In **Chapter 2**, the control systems for two series FCHVs are presented. The first vehicle is a commercial BEV that was hybridized by the addition of a 12 kW fuel cell, a hydrogen storage system, a power converter and an embedded PC. A specific software was designed to control the operating modes of the FC and the converter and to manage the flows of power between the devices. A second configuration is presented for this vehicle, with different batteries and converters, and two 2.4 kW FCs. For both configurations, **real tests were performed to validate the controllers**.

  The second vehicle is a prototype FCHV with a 56 kW fuel cell. In this case, the power system of the vehicle was modelled, and a MPC strategy was used for its management. Two variants were added to the model: one with UC substituting the batteries, and another one with both kinds of power sources. The three configurations are compared in terms of efficiency and performance.

- In **Chapter 3** a power management controller is designed for the model of a combined architecture (series-parallel) PHEV (Chevrolet Volt) provided for a special benchmark session at Ecosm'12. The vehicle has one ICE and two EMs that can be combined in four modes of operation, that correspond to three degrees of hybridness: 1 or 2 motor pure electric, range extender, and power split. And also different series/parallel architectures. It is assumed that a Global Positioning System (GPS) device supplies approximate data of the total distance and average speed of the cycle.

  The philosophy of the controller is to estimate the energy required to complete the cycle and compare it to the energy stored in the batteries. A higher level controller distributes the energy of the batteries to fulfil the requirements, and in case this energy is not enough, the ICE will supply the rest in the most efficiency way. Meanwhile, a lower level controller guarantees the good performance of the car.

- In **Chapter 4** the problem of thermal management in HVs is addressed. As a first step, a thermal model of the cabin of a hybrid vehicle is presented. The aim of this model is to estimate the heat fluxes in the cabin, being used as a part of a more complex HV model. The heat fluxes taken into account in this chapter have been: the solar irradiation to the external surfaces of the cabin and to the internal elements, the convection in the external and internal surfaces of the cabin, the conduction between the external and the internal surfaces, the human heat and the air mass flow from the ambience.

The temperature of the air of the cabin in the simulations was compared with real data, taken from a temperature sensor network installed in a real vehicle. The model was validated with several tests in different ambient conditions: solar irradiation, external air temperature, car occupants and driving cycles.

- In **Chapter 5**, the influence of a HVAC system in a HV is studied, in terms of performance and energy/fuel consumption. For this aim, the model of an ACS is designed. This system, coupled with the thermal model of the cabin of a vehicle presented in Chapter 4, estimates the power required to keep the temperature of the air of the cabin in a constant value.

  This system was integrated into the models of two HVs with different energy sources, degrees of hybridness and series/parallel configurations. The first one is a BMW 1 series FCHV: a series range extender HV with a MPC strategy to control the power management. The second HV is the ICEHV Chevrolet Volt, which is a combined series/parallel PHEV with a rule-based controller based on energy estimation. The results in both vehicles are discussed and compared.

- In **Chapter 6**, the dynamics control of a four in-wheel independent driving vehicle is presented. A mechanical model in this vehicle was made for this thesis, in a 3D Computer-Aided Design (CAD) software. Two different versions of the steering systems were introduced, so the model could be ported to *Matlab-Simulink Simmechanics* and ADAMS/ADAMS Car software.

  The *Matlab-Simulink Simmechanics* is also presented in this chapter. This model was validated with data taken from tests performed with the real vehicle. Finally, two torque distribution controllers were designed and tested on the simulator.

- In **Chapter 7** the conclusions and contributions for this thesis are summarized, as well as the future lines of research in the fields of study of this work.

Chapter 2

Power management in fuel cell hybrid vehicles

2.1. Introduction

FCHV are being investigated in many research and development programs motivated by the urgent need for more fuel-efficient vehicles that produce fewer harmful emissions. Hybridization can greatly benefit FC technology. There are many potential advantages such as the improvement of transient power demand, the ability of regenerative braking and the opportunities for optimization of the efficiency of the vehicle. The coordination among the various power sources requires a high level of control in the vehicle.

The objective of a hybrid vehicle power management is to control the power flows accordingly to operational objectives, usually related to fuel consumption minimization, taking into account other aspects, like the final state of charge of batteries or driving comfort, while satisfying operating constraints and ensuring that variables as engine torque and speed, SOC, etc., are within their limits. Many different approaches have been used to implement power management strategies for hybrid electric vehicles [51].

Most of the practical controllers in real vehicles are heuristic rules based [71, 97, 119, 120]. These strategies are based on the requested drive torque and on the speed of the vehicle. Most of these approaches try to maintain the state of charge of the batteries between an upper and a lower limit. An algorithm for a hybrid vehicle with combustion engine, trying to operate the engine in the highest efficiency range is presented in [101]. The main advantage of these controllers is that they are intuitive and easy to implement but they present a limited robustness. Some other approaches are based on optimal or suboptimal control strategies. A method to define and calculate an equivalence factor that weighs the fuel energy with the electrical energy is presented in [51, 102]. Then, the cost function is defined taking into account the fuel energy and the fuel equivalent of the electrical energy. This strategy is called ECMS. The main problem in this approach is the computation of the equivalence factors, because they are different in battery charge and discharge phases and depend on energy conversion efficiencies. Adaptive approaches, where the equivalence factors are computed during the real time operation are presented in [66] and [89]. Also, the

Figure 2.1: GEM eL car.

T-ECMS [103] approach estimated continuously the control parameters on-board by using data from the static features of the route and from a telemetry system.

Recently, MPC [21] is appearing as a practical alternative for power management method in hybrid vehicles. Different applications can be found in [7, 13, 95]. A hybrid MPC strategy has been proposed for the Hercules Project with the objective of preserving battery lifetime by imposing charging and discharging strategies.

Other optimal control strategies, like the one based on the Pontryagins minimum principle is suggested as a viable real- time strategy in [65]. However, it has not been tested on vehicles.

2.2. Delfín projects

The goal of these research projects is to prove the feasibility of the use of hydrogen as an energy source for automotive applications. For this aim, a commercial electric car (GEM eL, Figure 2.1) was acquired as an experimental platform. This vehicle was used in two projects (Delfín I and II). In both projects, a fuel cell, a hydrogen storage system and a power converter were installed in the vehicle. Additionally, a control system has been developed for the power management tasks, and to guarantee a safe operation of the vehicle. Both projects and their tests are detailed and explained in the following subsections.

The main characteristics of the original vehicle are shown in Table 2.1 [42].

2.2.1. Delfín I

Description

The original power train of the vehicle has been used. The power of the D.C. electric motor is 3.72 kW at 72 Volts, with 6 gel batteries of 12 V each. The PEM fuel cell is the HyPM-12XR, supplied by Hydrogenics, which main characteristics are shown in Table 2.2.

Hydrogen is stored on board at 200 bar using a tank supplied by Dynetek (model L033), with a capacity of 5.8 Nm^3, equivalent to 476.25 grams of hydrogen and 33 litres of volume. The hydrogen storage system includes pressure sensors, electro valves, regulators and the

Table 2.1: GEM eL specifications.

Curb Weight	1,285 lb
GVW	2,300 lb
Payload Capacity	1,015 lb
Length	144”
Height	70”
Width	55”
Wheelbase	114”
Cubic Feet of Cab	47 ft^3
Turning Radius	17 ft
Tires	12-inch
Top Speed	25 mph
Ground Clearance	8”

Table 2.2: Hydrogenics HyPM-12XR specifications.

Maximum output power	12.5 kW
Otuput voltage range	37-57 V
Maximum current	350 A
Dimension	96 x 50 x 32 cm.
Volume	153.6 l
Weight	90 kg

outlet connection for refuelling. Figure 2.2(a) shows a scheme of the disposition of the fuel tank and the rest of the devices of the vehicle, while Figure 2.2(b) shows the real vehicle.

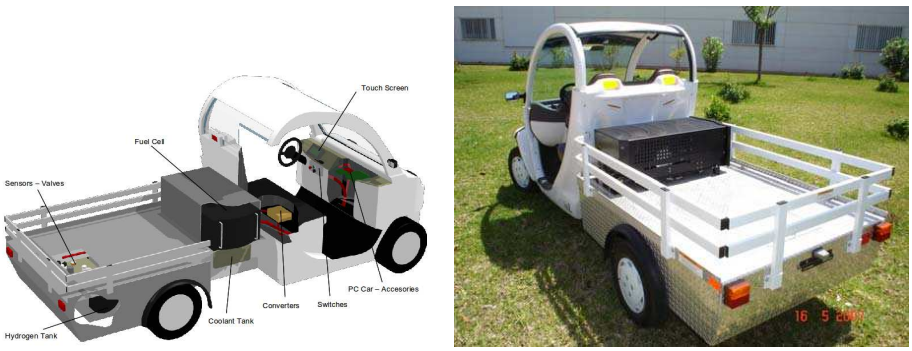

(a) Delfín I scheme.

(b) Delfín I (vehicle).

Figure 2.2: Delfín I

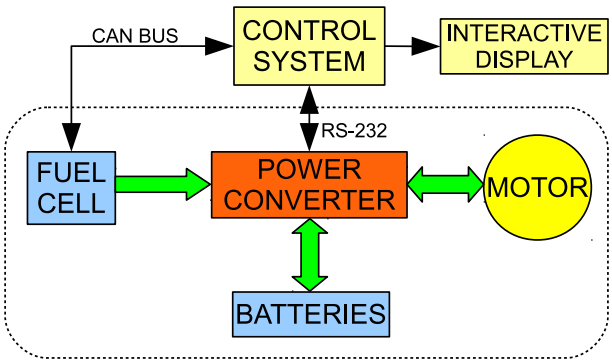

Figure 2.3: Control system scheme.

Control System and integration

The controller must determine how to operate the different power units (fuel cell, batteries and converters) to fulfil the power demanded by the motor in the most convenient way. Also, the most important parameters of the system are monitored and historical data are stored.

The control system is based on an embedded controller located in the dashboard of the car. Figure 2.3 shows a scheme with the different modules of the system and communication among them. CANBus protocol (CAN 2.0A) has been implemented for linking the control system and the fuel cell, allowing the operation of the fuel cell and the reception of its status and parameters for control and monitoring purposes, with a communication speed 250 kbits/s. Communication between the control system and the power converter is performed using a RS-232 protocol.

The main tasks of the control system are:

- Start-up and shut-down procedures: The start-up procedure has been designed to efficiently start up the different units in an ordered way, taking into account security aspects. That includes the hydrogen storage system, power converter and, in communication with the electronic control unit (ECU) of the fuel cell, switch among the different states of the fuel cell. Also, procedures have been implemented to shut-down the system.

- Power management: Power management is the most important task. It consists of computing the power that must be demanded to the fuel cell in real time. This computation is done in order to satisfy the power demand of the electric motor taking into account the state of charge of the batteries and the operating regime of the fuel cell. This is accomplished by manipulating the electronic converter which demands the power that the fuel cell supplies to the batteries. In this case, the aim was to develop a simple power management, as a preliminary step. The controller checks the SOC of the batteries continuously, recharging them in case they do not reach a certain threshold.

- Monitoring: The control system monitors fuel cell and other systems operating conditions. Most of the variables of the system (voltages, currents, temperature and

Figure 2.4: Display of the driver.

hydrogen pressure) are shown under user request and historical data are stored and are available for studying the vehicle performance. Also, the operator is informed of any critical system condition to facilitate user intervention when needed.

- HMI: Control actions can be executed and the system status is displayed in a touch screen. Figure 2.4 shows one of the screens, where the general status of the vehicle can be seen, including alarms in different subsystems and buttons to launch start-up and shut-down procedures.

Experimental results

The control system has been tested under several driving conditions and it has shown that it is able to fulfil the requested objectives, showing useful information to the driver about system functioning. The software stores a sort of data, useful for the developers: converter input and output current, voltage of the batteries, hydrogen pressure, etc. Analysing this information it is possible to see the performance of the system, previewing hypothetical problems, and correcting possible developing mistakes.

Figure 2.5 shows a graphic that represents some of the stored variables.

The graphic shows the first minutes of operation of the car. Several time windows can be identified corresponding to different situations:

- Window A-B: The system has been started. The car is stopped until the driver/passengers are ready, or it is running at low speed.

- Window B-C: At 'B' the batteries voltage reaches the threshold. The fuel cell enters run mode; therefore its voltage increases fast from 0 to 52 volts. The system waits some time for the fuel cell to stabilize before requesting any power, so the fuel cell current is still zero. The oscillations of the voltage of the batteries are produced by the driving cycle. The driver may be accelerating and braking the car continuously.

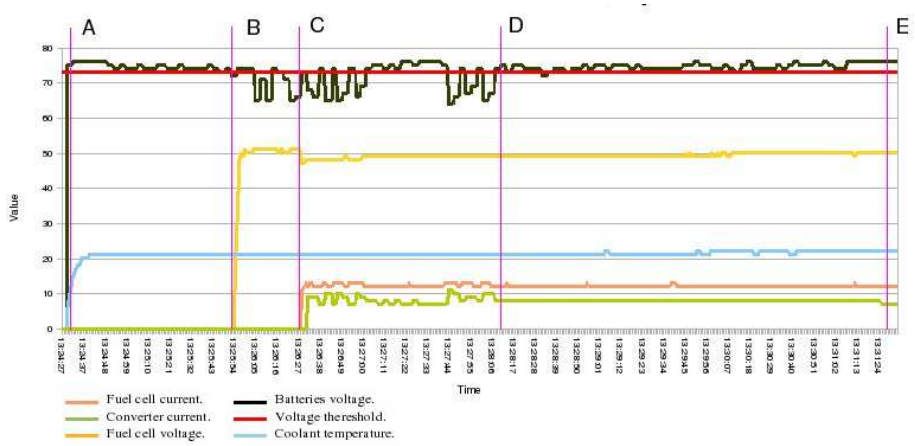

Figure 2.5: Evolution of electrical variables.

- Window C-D: At 'C' the converter starts requesting power to the fuel cell, so its current experiences a fast increase, until it reaches 12-14 A approximately. The oscillations of the current correspond to the ones of the voltage, caused by the aggressive driving mode. The falling of the voltage means that the motor requires more power; therefore the current from the fuel cell must be increased. The electronic power converter turns the fuel cell voltage from about 50 volts to more than 70, so its current is lower than the output current of the fuel cell as it is shown in the graphic.

- Window D-E: Everything is still the same except for the driving. The batteries voltage has very little oscillation, which means that the car is set to a constant and moderated speed. Consequently, current suffer very low variations. Despite the voltage keeps higher than the threshold for a period of time, the fuel cell continues running and power is still being required for charging the batteries. Actually, the fuel cell will work until the batteries voltage reaches a higher threshold; and it will not be stopped until the voltage falls again lower than the threshold shown in the figure, as previously explained.

Coolant temperature: During the time that the fuel cell is running, the coolant temperature increases about two degrees. However, the fuel cell will not get damaged unless the temperature reaches 75^oC, and this is not supposed to happen. Nevertheless, if the limit temperature is exceeded the fuel cell would automatically be stopped by the controller. The Figure 2.6 shows the evolution of the coolant temperature in a longer experiment (about five hours long).

In the same test it is possible to see how the batteries voltage increases from about 73 to 77 volts. Figure 2.7 shows the oscillations of the first few minutes caused by a testing driving (accelerating and braking continuously), and a constant evolution when the car is running at cruise speed.

Another interesting variable is hydrogen consumption. Figure 2.8 shows the evolution of the tank level, that decreases at 0.625 g/min average. Assuming that the tank capacity is 476.25 grams, the system could be working for more than twelve hours.

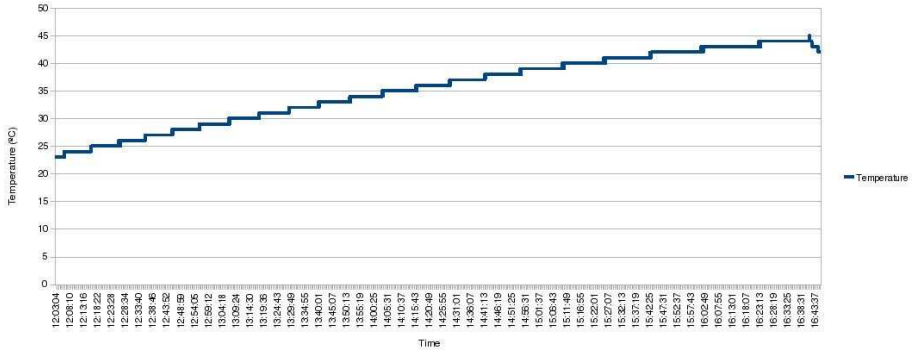

Figure 2.6: Coolant temperature.

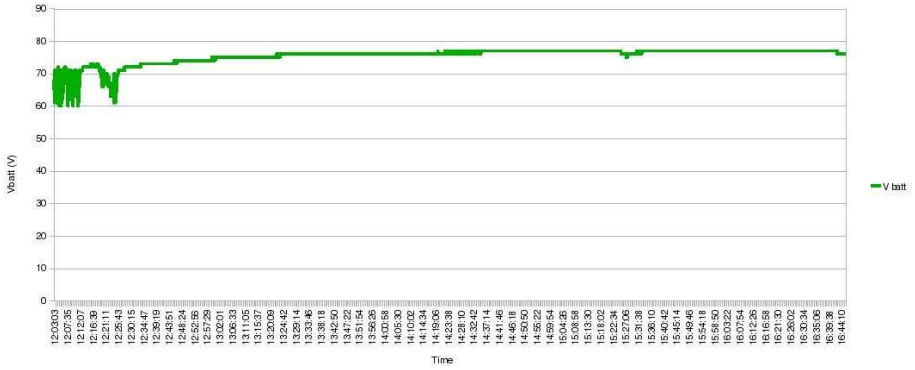

Figure 2.7: Battery voltage evolution.

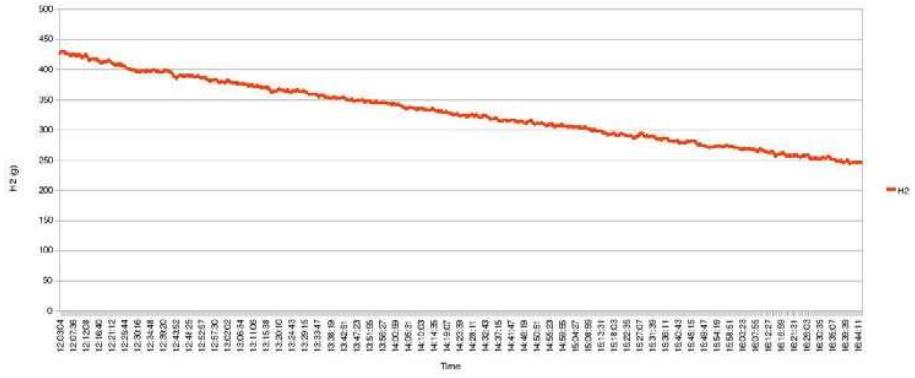

Figure 2.8: Hydrogen consumption.

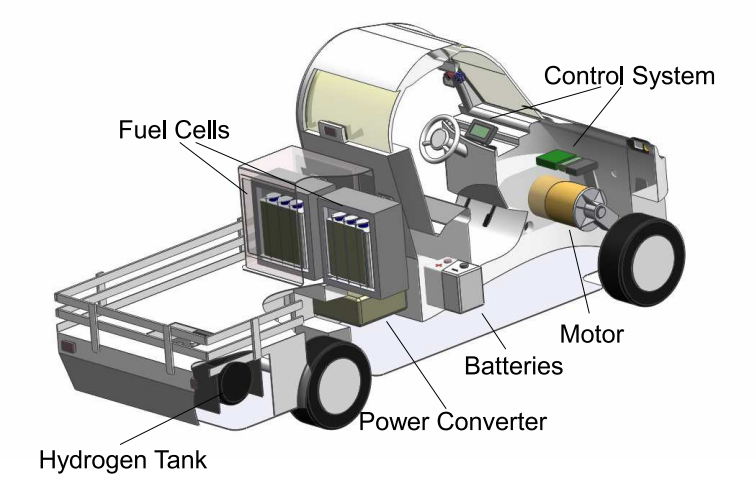

Figure 2.9: Vehicle components.

2.2.2. Delfín II

Description

Based on the same vehicle as the Delfín I project (a GEM eL electric car), the motor and the hydrogen storage system are the only elements remaining from the previous project. Figure 2.9 shows the new disposition of the devices of the vehicle.

The new devices are listed and described here:

- Batteries: The vehicle includes four VRLA E8G100-12/12-100G gel batteries:
  - Nominal voltage: 12 V.
  - Capacity: 100 Ah.
  - Dimensions: 305x168x215 mm.
  - Weight: 31 kg.
- Fuel cells: The fuel cells consist of two 56 cell 1020ACS Ballard stacks from whose auxiliary systems have been completely developed.
  - Nominal output power: 2.4 kW
  - Output voltage range: 34-56 V
  - Maximum current: 75 A
  - Dimension: 351x363x103 mm
  - Weight: 11.06 kg
- Power converter: This device was designed and built for this project by the Electronic Technologic Group (GTE) of University of Seville and modified by the company Win Inertia. The converter guarantees the motor voltage (current) to be maintained at 80 V (50A, max.), the batteries voltage (current) at 50 V (-30 A min.; +50 A max.), and each fuel cell at its corresponding voltage, depending on its current (max. 30 A).

Figure 2.10: Vehicle.

- Controllers and Human Machine Interface: The controllers were programmed in POSIX C language, and were embedded into a PC-104 running a QNX operating system image. The Human Machine Interface (HMI) was programmed using LabView, and was embedded into a VIA-EPIA MII 10000E board, running Windows XP, and connected to a touch screen display.

Figure 2.10 shows the prototype.

System and Integration

The control system of the vehicle consists of three controllers operating at different levels. The upper level is devoted to the global power management among the different subsystems of the vehicle. It receives the throttle position as a reference (which means an estimation of the power required by the driver) and sends the power references to the fuel cells controllers and the power converters. The second controller splits the power computed by the upper controller between the two fuel cells, that is the power reference for each one of the fuel cells. Finally, the lower level controllers perform the internal control of the two fuel cells (temperature and air supply as shown in Figure 2.11). The real-time control system is implemented on an embedded controller (PC-104) located in the dashboard of the car. Figure 2.11 shows a scheme with the different modules of the system and communication among them. Controller Area Network (CAN) protocol (version 2.0A) has been implemented for linking all the devices. The following paragraphs describe the main tasks of the control system in a more detailed manner.

Start-up and shut-down procedures

The start-up procedure has been designed to efficiently start up the different units in an ordered way, taking into account security issues. Also, procedures have been implemented to shut-down the system.

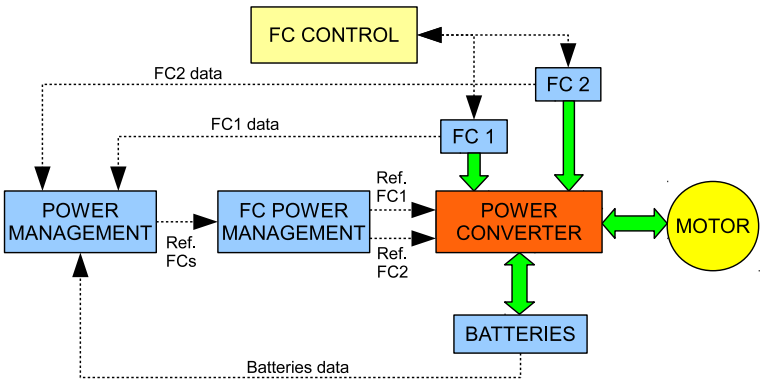

Figure 2.11: Control system scheme.

Power management

The power management mainly computes the power that must be provided by the fuel cells in real time. This computation is done in order to satisfy the power demand of the electric motor taking into account the state of charge of the battery and the operating regime of the fuel cells.

The algorithm takes the reference of the driver (P_{ref}) and the operating point, and calculates the region of the possible solutions (yellow region on Figure 2.12), according to the constraints (value and rate) of the fuel cells and the battery. This step is done in every iteration. The controller differences three scenarios, depending on the allocation of the reference respect to the region of possible solutions.

In *Case a*, the reference is above the region, and the system will provide its maximum available power (point A in Figure 2.13(a)). On the other hand, in *Case b* the reference is below the region, and the system will provide its minimum possible power (point B in Figure 2.13(a)).

Finally, if the reference crosses the area (*Case c*), the solution will depend on the battery SOC, where three states are defined: high, medium and low charge (Figure 2.13(b)). If the state is low the fuel cell will provide its maximum power inside the region of the possible solutions, in order to avoid the battery discharge. On the contrary, if the state is high, the batteries will provide their maximum power to avoid an overcharge. In other case, the manager will choose the closest point to the current operating point (points C_1, C_2 and C_3, respectively in Figure 2.13(b)).

Fuel Cell stacks control

Low level fuel cell control is individually executed to ensure an independent operation between stacks. In this way, FC stacks are isolated both electrically and operationally between them. The specifications on normal operation given by the manufacturer have been followed, but they have been modified in some cases due to several alterations observed in the behaviour. These alterations are mainly caused by particular deviations of each stack and by degradations suffered in function of storage and working times.

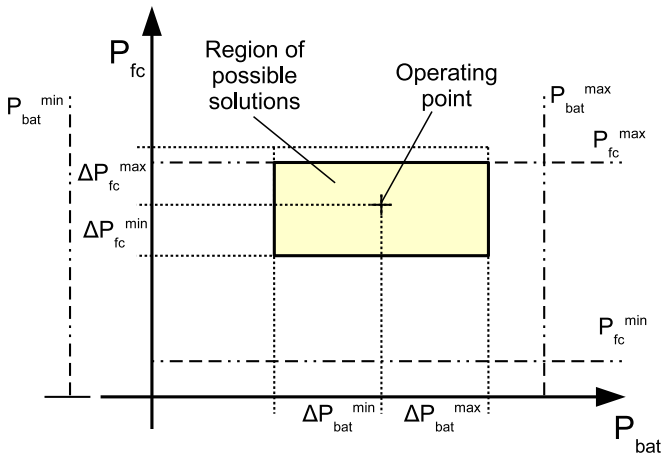

Figure 2.12: Power management scheme.

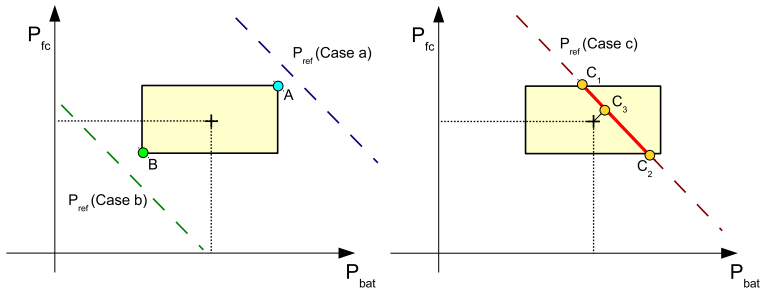

(a) Power management, Cases *a* and *b*.

(b) Power management, Case *c*.

Figure 2.13: Different cases in the power management of Delfín II.

The controller is designed to regulate two variables: temperature and oxygen excess ratio. Besides, a correct voltage in the cells must be kept for every current drawn from each stack at any time. This voltage must be in a certain range to avoid the loss of performance, degradation, and even the total failure.

The voltage between the terminals of each FC is measured by the DC/DC converter. However, for a better monitoring, a Cell Voltage Monitor (CVM) system has been developed, measuring the voltage by pairs of cells, as the manufacturer recommends. To monitor the air temperature, each stack has two temperature sensors, allocated in the cathode inlet and in a middle point of the stack, respectively.

This model of stack admits cooling and oxidant in the same air flow. The air is blown into the cathode by two fans, situated in the side of an enclosure where the stack stands. The hydrogen flow is set in a dead-end configuration, channelling from the tank to a buffer accumulator, which is aimed to avoid pressure drops during the purges, feeding both stacks in parallel. The output pressure of the tank and the input pressure of the anodes are adjusted by manual valves, while a solenoid valve opens and closes the fuel flow. Finally, there are

two purge valves at both anode outlets, controlled by the controller. In summary, control is handled in two sections: acting over the fans, the correct cooling/oxidation level is ensured. On the other side, the actuation over the opening and closing of the purge valves regenerates the fuel inside the anode.

1) Oxygen stoichiometry / stack temperature control:

The controller actuates over the fans of each fuel cell, with two goals: keep the temperature of the stack around the specified optimal value and guarantee the oxygen feeding. For these aims, an override controller was designed, where the main task is to control the temperature of the stack.

A PID controller is used to track the temperature set point, calculated using Equation 2.1, provided by the manufacturer [11].

$$T_{opt} = \frac{I}{2} + 26 \tag{2.1}$$

Where T_{opt} is the optimal temperature in the stack (^oC) and I is the current drained from the stack (A).

On the other hand, the controller supervises the stoichiometry to prevent oxygen starvation. This phenomenon may happen in certain situations in which the air flow is reduced to reach stabilization (like start ups or large increments of current). The stoichiometry is calculated using the mass flow equations provided by the manufacturer [11] 2.2 and 2.3, and its value should never be lower than 50.

$$\dot{m}_{coolant} = \frac{(1.25 - V_{avg}) \cdot n \cdot I}{T_{st} - T_{amb} \cdot C_p} \tag{2.2}$$

$$\dot{m}_{oxidant} = I \cdot n \cdot 0.0166(slpm1/A1/cell) \tag{2.3}$$

Therefore:

$$Stoich = \frac{\dot{m}_{coolant}}{\dot{m}_{oxidant}} = \frac{1.25 - V_{avg}}{(T_{st} - T_{amb}) \cdot C_p \cdot 0.0166} \tag{2.4}$$

Where V_{avg} is the average voltage in the cells (V), T_{st} is the stack temperature (^oC), T_{amb} is the ambient temperature (^oC), I is the current in the stack, n is the number of cells and C_p is the heat capacity of the air.

Figure 2.14 shows an scheme of the override controller.

2) Purge control:

The duration of the purges (time between opening and closing of the exhaust valve) is constant during the operation. The interval between purges changes depending on the drawn current and it is established in a ratio of $2750(A \cdot s)$.

Fuel Cell stacks power allocation

Once the power manager calculates the total power to be provided by the stacks, other algorithm is responsible of deciding the allocation of such power between them. This is a very open algorithm, since several work plans can be used for the stacks. In this case, a master-slave strategy has been implemented, i. e., one of them (master) will provide all the needed power within its capabilities, and the other one (slave) will come into play when the

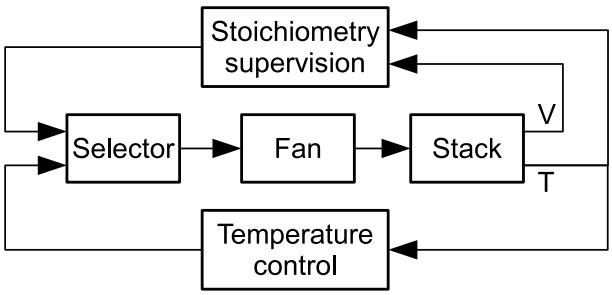

Figure 2.14: Temperature/oxidant override control.

requirements rise high. This is similar to the behaviour of some hybrid commercial vehicles, in which one of the sources provides the power in usual working while the other one does it in more demanding situations (sloping, hard accelerating, loading low batteries...). The decision about which of them is master is also very open. In each startup, the one with less accumulated working time has been assigned as master, in order to match between them the degradation caused by the use. Other possibilities include last working date (degradation by storage), number of startups/shutdowns or past behaviour. The final step is sending the current set point to the converters of the stacks corresponding to their assigned power.

Monitoring

The control system monitors the fuel cells and the power converter operating conditions. Most of the variables of the system (voltages, currents, temperature and hydrogen pressure) are shown under user request and historical data is stored and available for studying the vehicle performance. Also, the operator is informed of any critical system condition to facilitate user intervention when needed.

HMI

Control actions can be executed and the system status is displayed in a touch screen. Figure 2.15 shows one of the screens, where the general status of the vehicle can be seen, including alarms in different subsystems.

Experimental Results

The electric vehicle has been experimentally tested in the Fuel Cell Control Lab sited in *Escuela Técnica Superior de Ingeniería* of University of Seville. The experiments were focused on demonstrating the correct operation of the three-level control described in section III. Figure 2.16 shows experimental results of the lowest control level, controlling each fuel cell using the air supplied to the cathode by the two fans as input variables. The graph shows the voltage and current supplied by the fuel cell, the hydrogen purge solenoid valve which is opened to completely renew the hydrogen anode in each corresponding time interval and other interesting variables such as fans or voltage stack temperature and manufacturer recommended operation temperature.

Figure 2.15: Main display of the HMI.

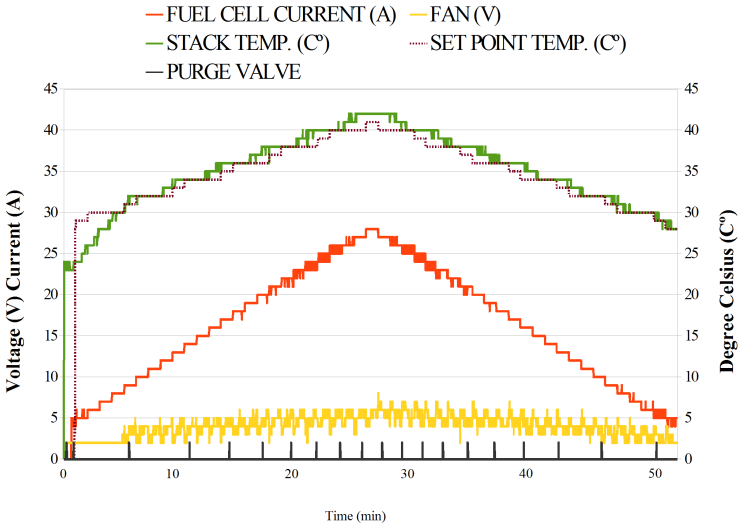

Figure 2.16: Fuel cell control.

The first experiment, used to obtain a standard type of polarization curve, lasts about one hour and starts increasing gradually the current demand to the stack to provide approximately 30 A and then decreases gradually, returning to the minimum operating current of 5 A. It can be seen that as the power provided by the fuel cell increases, the intervals between purges of hydrogen, represented by vertical lines along the horizontal axis, become smaller.

The set point temperature of the stack (the line represented by a magenta dashed line) is tracked by the temperature of the stack due to the fan control action, providing a consistent performance. Another experiment, represented in Figure 2.17, shows other important variables for the correct operation of the stack, like the average voltage of the 56 cells of each one of the two fuel cell stacks and their individual deviation. The voltage of the cell

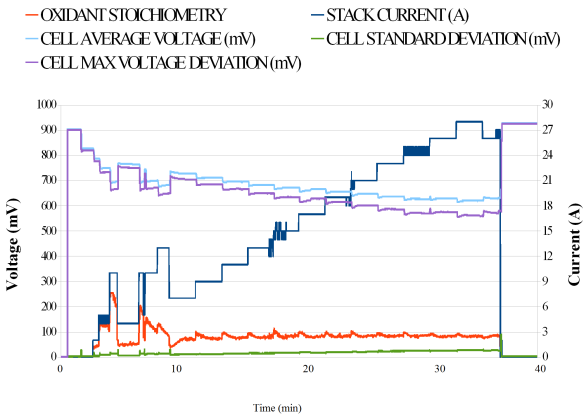

Figure 2.17: Cell control.

with a larger deviation from the mean voltage (variable 'Cell Max Voltage Deviation') is also represented.

The controller will continuously try the average voltage of the cell to resemble the values recommended by the manufacturer as a current value of the stack. The controller forces the stack to provide its maximum performance with an oxidant stoichiometry between 50 and 200.

Once the operation of a single fuel cell stack has been exposed, the way the second-level controller manages both fuel cell stacks together is shown below. Figure 2.18 shows the case of a low state of charge of the battery. In this case it is observed that Fuel Cell Stack 2, which operates as master, provides most of the energy and Fuel Cell Stack 1, which operates as a slave, begins operating at its minimum until the master cannot provide more power. At that moment, the slave provides the rest needed to achieve the demand of power.

Finally, the results of power management of the entire system, comprised of battery and fuel cells, will be discussed. The control manages the power delivered from each source to the electric motor of the vehicle at any time. Besides, the controller can decide to recharge the battery with the energy provided by the fuel cells if necessary.

Figure 2.19 shows the power of the fuel cells, the power of the DC-LINK (the power consumed by the motor) and the power of the batteries for a low-level SOC scenario. The batteries will track sudden changes in energy demand from the electric motor because of their faster dynamics. The demand signal is represented by the throttle as a percentage. The power in the DC-LINK is updated according to the command captured from the throttle, and then the power management system distributes the power in order to satisfy their energy demands. In this case, the fuel cells provide power directly to the electric motor and also provide power to recharge the batteries, which power is positive only in the peaks.

Figure 2.20 shows a case of medium-level SOC. Here, the fuel cell stacks start running in idle state until they start to charge the battery, while the motor does not demand power. After the second minute of the test, the driver requests power, and it is supplied mainly by the battery. During the third part of the test (after four minutes), the driver releases the

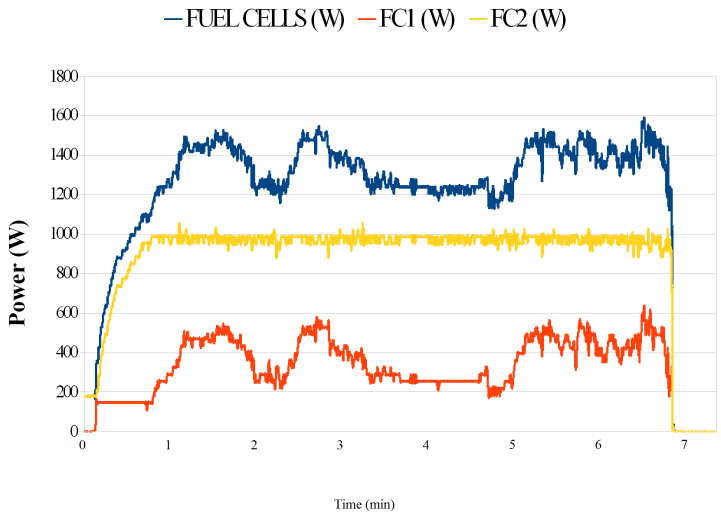

Figure 2.18: Fuel cells management. Fuel Cell Stack 1 as slave and Fuel Cell Stack 2 working as master.

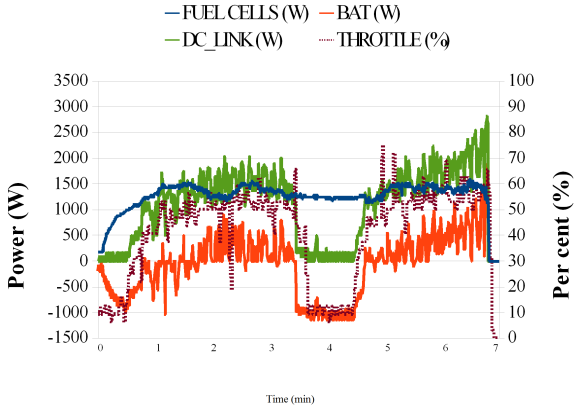

Figure 2.19: Power management in a low-level SOC scenario.

330 throttle but the fuel cells continue charging the batteries.

Figure 2.21 shows a case of high-level SOC. Like in the previous case, the fuel cells start running in idle state. However, when the driver requests power the fuel cells remain in idle state. The batteries supply the rest of the power in order to diminish their state of charge, avoiding a full charge state that could last in an undesirable overcharge.

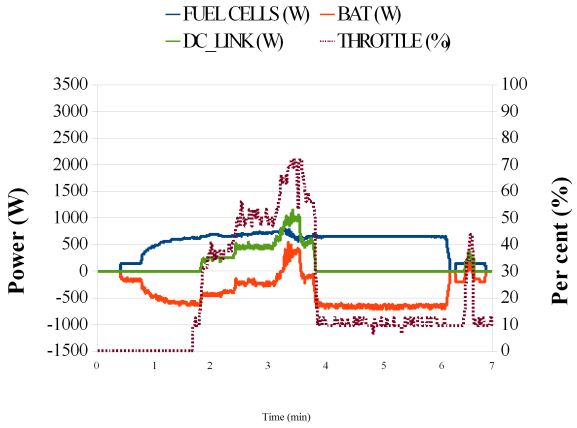

Figure 2.20: Power management in a medium-level SOC scenario.

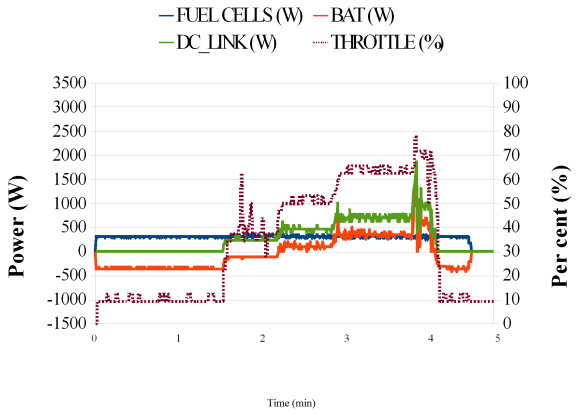

Figure 2.21: Power management in a high-level SOC scenario.

2.3. Hércules Project

2.3.1. Introduction

The development of a free-emission vehicle is the objective of Hercules Project, as detailed in [8]. It is a proof project that implies the development and integration of technology throughout the hydrogen value chain, including renewable hydrogen production, distribution and supply of hydrogen as vehicle fuel and finally, the design, development and test of a fuel cell car prototype. Hercules Project uses photovoltaic panels to generate electrical energy, which areused in a electrolyzer for the production of renewable hydrogen. A refuelling station to supply the electrical vehicle with hydrogen was installed. This section is focused on the hybrid fuel cell vehicle developed in Hercules Project and specifically in the power management control system. The goal of a hybrid vehicle power management is to control the power flow accordingly to control objectives, usually related to fuel consumption minimization, taking into account other aspects, as the final state of charge of batteries or driving comfort, while satisfying operating constraints, ensuring that variables as engine torque and speed, state of charge, etc., are within their limits. Many different approaches have been used to implement power management strategies for pure [75] or hybrid electric vehicles [3, 41, 51, 80].

This section presents a multivariable MPC approach for power management in Hercules hybrid fuel cell vehicle that will minimize hydrogen consumption and will keep the state of charge of the battery around a desired level. The strategy is compared with two common approaches: a heuristic algorithm and the ECMS method. In addition, the powering system has been compared with another in which the batteries are substituted by UCs, and a third one composed of both types of power sources.

2.3.2. Vehicle description

The vehicle is based on a commercial Santana 350 SUV (Figure 2.22).

In this vehicle the engine and its auxiliary devices have been removed. In their place, the following devices have been installed:

- A PEM fuel cell: Nuvera with a maximum peak power of $56kW$ (Figure 2.23(a)).
- A pack of Lithium-ion Batteries: four modules of 13 Li-ion 3.7 V cells in series, model Kokam SLPB 125255255H. The specifications of each cell are shown in Table 2.3.
- A Permanent Magnet Synchronous Motor (PMSM): the nominal power is 66 kW and the maximum torque is $460Nm$ (Figure 2.23(b)).
- A hydrogen storage system: it consists on two tanks of $33l$ and one of $24l$, the three of them with a maximum pressure of 350 bar. This system could store up to $2.4kg$ of hydrogen (Figure 2.23(c)).

As explained in Section 2.3.1, the possibility of substituting the batteries for UCs, or combining both types of sources is also studied. In the first case, two modules in parallel of 126 Maxwell BCAP 2000 capacitors in series would substitute the pack of batteries. For

Figure 2.22: Hércules vehicle.

Nominal capacity	75 Ah
Nominal voltage	3.7 V
End of discharge	3.0 V
Max. charging voltage	4.15 V
Max. charging current	225 A
Max. discharging current	450 A
Operating temperature ranges	Charge: 10 to 45 ^oC; Discharge: -20 to 55 ^oC
Weight	Max. 1.73 kg
Dimensions	262x257x12,3 mm

Table 2.3: Specifications of the batteries.

the second, only two of the four modules of batteries and one of the two modules of UCs would be used.

A scheme of the Hercules vehicle is shown in Figure 2.24. The fuel cell and the lithium-ion batteries feed an electrical motor through DC/DC converters to connect the different systems to the DC bus. The DC/DC converter which connects the fuel cell to the DC bus is unilateral and rises the fuel cell voltage to the DC bus voltage. The other two converters are bidirectional, allowing regenerative braking and battery recharging.

2.3.3. Model description

The objective of the vehicle submodel is to obtain the power demanded by the electric motor to achieve a certain pre-specified driving cycle. This submodel is not required for the control design but it is necessary to calculate the motor power demand which the power

(a) Nuvera 56*kW* fuel cell. (b) Electric motor. (c) Hydrogen tanks in the vehicle.

Figure 2.23: Hércules devices.

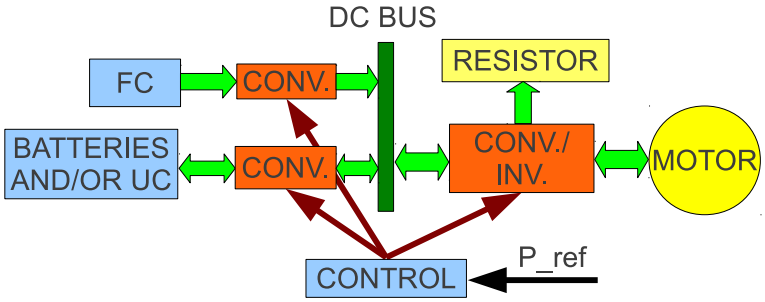

Figure 2.24: Hércules scheme.

management control must satisfy to achieve the desired driving cycle. Its inputs are speed, acceleration and road slope profiles and its output is the motor power demand. The speed profile depends on the driving pattern, for instance urban or highway patterns.

The model starts with the balance of the forces that actuate over it (Ecuation 2.5).

$$F_t(t) = m_v \cdot a_v(t) + F_a(t) + F_r(t) + F_g(t) \tag{2.5}$$

Where F_t is the tractive force in the wheels, m_v is the mass of the vehicle, a_v is the linear acceleration of the car, F_a the air resistance, F_r the rolling resistance and F_g the force of gravity. These forces are calculated with the expressions 2.6, 2.7 y 2.8:

$$F_a(v) = \frac{1}{2} \cdot \rho_a \cdot a_v(t) \cdot A_f \cdot c_d \cdot v^2 \tag{2.6}$$

$$F_r = c_r \cdot m_v \cdot g \cdot \cos(\alpha), v > 0 \tag{2.7}$$

$$F_g(\alpha) = m_v \cdot g \cdot \sin(\alpha) \tag{2.8}$$

Where c_d is the drag factor, A_f the front area, ρ_a the air density, c_r is the rolling resistance coefficient, g is the gravitational acceleration and α is the slope. From the force F_t the torque is calculated ($T(t)$).

$$T(t) = F_t(t) \cdot r \tag{2.9}$$

ρ_a	$1.204 kg/m^3$
A_f	$1.9675 m^2$
c_d	0.32
m_v	$1850 kg$
c_r	0.011
g	$9.8 m/s^2$
r	$0.32 m$

Table 2.4: Parameters of the model of the car.

Where r is the radius of the wheel. The rotational speed of the wheel can be calculated from the linear speed: 2.10.

$$\omega(t) = \frac{v(t)}{r} \tag{2.10}$$

The values of these parameters are shown in Table 2.4.

The wheels are connected to the transmission, which is also connected to the motor by a gearset, which is defined by the parameter γ:

$$\gamma = \frac{\omega_e \cdot r}{v(t)} \tag{2.11}$$

Where ω_e is the speed of the motor. In this case, $\gamma = 4.021$.

Once γ is known, the rotational speed and the torque of the motor can be calculated:

$$\omega_e(t) = \gamma \cdot \omega(t) \tag{2.12}$$

$$T_e(t) = \frac{T(t)}{\gamma} \tag{2.13}$$

Where T_e is the torque of the motor.

The poqer of the motor is given by Equiation 2.14.

$$P_e(t) = T_e(t) \cdot \omega_e(t) \tag{2.14}$$

Finally, the motor losses are given by equations 2.15 to 2.17.

If $\omega_e < 2000 rpm$:

$$P_{perd} = 0.0016 \cdot T_e^2 + 0.0082 \cdot \omega_e^2 \tag{2.15}$$

If $\omega_e \geq 2000 rpm$:

$$P_{perd} = 4.05 \cdot T_e^2 \cdot \omega^2 + 0.0082 \cdot \omega_e^2 \tag{2.16}$$

Therefore, the net power of the motor is:

$$P_m = P_e + P_{perd} \tag{2.17}$$

The batteries were modelled from their datasheet, as described in [98]. The UCs were modelled using the basic equations of behaviour of a capacitor, and from their datasheet. The model of the FC was taken from [28], and for the electric motor a first order behaviour, with a time constant of 0.1s was assumed; since the motor has not been characterized by the vendor. The response of the power converters is much faster than the response of the other devices. Therefore, a static behaviour was assumed for this device.

2.3.4. Controller description

Model Predictive Control

The MPC controller minimizes a cost function, predicting the future outputs with an internal model, taking into account the present and the predicted values of the inputs (in a certain interval of time). Always respecting the constraints of all the variables. The cost function is a quadratic function that penalises the error in the system outputs (total power and batteries SOC) and the difference to the target value of the manipulated variables (MV) and their rates, as shown in Equation 2.18:

$$J = \min_{\Delta u(k|k),\ldots,\Delta u(m-1+k|k),\varepsilon} \left\{ \sum_{i=0}^{p-1} \left(\sum_{j=1}^{n_y} |w_{i+1,j}^{y}(y_j(k+i+1|k) - r_j(k+i-1))|^2 + \right.\right. \\ \left.\left. + \sum_{j=1}^{n_u} |w_{i,j}^{\Delta u} \Delta u_j(k+i|k)|^2 + \sum_{j=1}^{n_u} |w_{i,j}^{u}(u_j(k+i|k) - u_{jtarget}(k+i))|^2 \right) + \rho_\varepsilon \varepsilon^2 \right\} \tag{2.18}$$

where the subscript j indicate the output/MV number, n_y is the number of outputs, n_u the number of manipulated variables, p is the prediction horizon, w are the weights and the expression $X(k+i|k)$ is referring to the calculation of the parameter X at the moment $k+i$, with the information known at the moment k. The variable $\varepsilon \geq 0$ and its weight ρ_ε determine the constraint softening.

Equations 2.19 to 2.22 show the constraints of the system, where variables V represent the Equal Concern for the Relaxation (ECR) vectors. These values set the priority of the softness of each constraint.

$$u_{j_{min}}(i) - \varepsilon V_{jmin}^{u}(i) \leqslant u_j(k+i|k) \leqslant u_{jmax}(i) + \varepsilon V_{jmax}^{u}(i) \tag{2.19}$$

$$\Delta u_{j_{min}}(i) - \varepsilon V_{jmin}^{\Delta u}(i) \leqslant \Delta u_j(k+i|k) \leqslant \Delta u_{jmax}(i) + \varepsilon V_{jmax}^{\Delta u}(i) \tag{2.20}$$

$$y_{j_{min}}(i) - \varepsilon V_{jmin}^{y}(i) \leqslant y_j(k+i|k) \leqslant y_{jmax}(i) + \varepsilon V_{jmax}^{y}(i) \tag{2.21}$$

where:

$$\Delta u(k+h|k) = 0, h = m, \ldots, p-1 \tag{2.22}$$

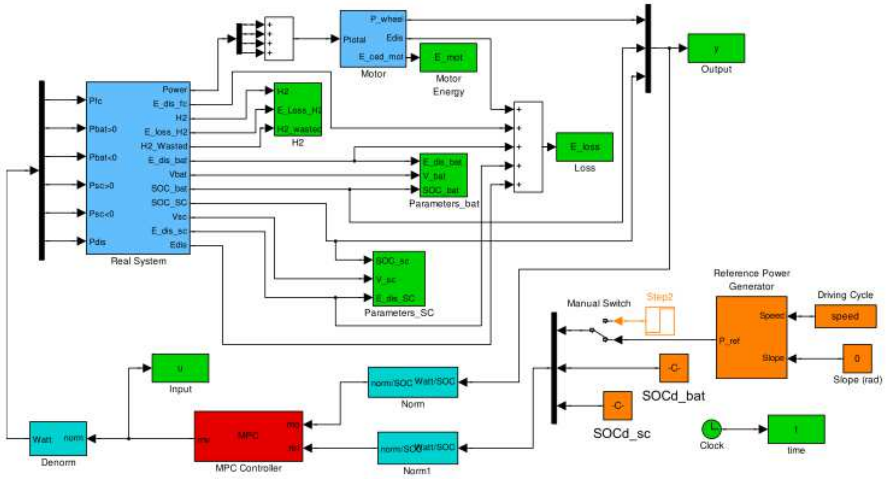

Figure 2.25: Simulink scheme.

MPC for the power management of a FCHV

The aim of the control strategy is to compute the power that must be supplied by each power source (fuel cell, UC and/or batteries) to fulfil the mechanical power demanded by the driver while the operational constraints are fulfilled. The control actions are computed in real time solving a multivariable MPC problem that will minimize fuel consumption and will keep the state of charge of the batteries at the desired level. The power system of the vehicle is composed on several subsystems, some of them non linear (like the fuel cell or the losses in the vehicle). The aim of the power management controller is to track a sort of parameters (SOC of the energy storage devices and power demand), avoiding the violation of some constraints (maximum/minimum power and power rate of each device) and minimizing the fuel consumption. This kind of system fits the philosophy of the MPCs, described in Section2.3.4.

The controlled variables of the MPC are the power required by the vehicle to track the cycle (Section 2.3.3) and the SOC of the batteries and/or UCs. The manipulated variables are the power transferred or absorbed by all the devices as well as the power dissipated for braking the car in case the storage devices cannot absorb it all.

A scheme of the Simulink model is shown in Figure 2.25.

The MPC controller was used by Pérez et al. [15] to compare this approach with a heuristic and a ECMS control strategy. Three tests were performed to make this comparison. For the first and the last one, a NEDC was tracked by the vehicle. The difference between both cycles is the initial value of the batteries SOC (0.4 and 0.8 respectively). In the second test a highway cycle was tracked by the car. The speed profiles of both tests are shown in Figures 2.26(a) and 2.26(b).

The final SOC for each test is shown in Table 2.5, while the hydrogen consumption is shown in Table 2.6

In order to make a better comparison, both fuel consumption and final SOC are combined in the computation of the equivalent fuel consumption, which is the sum of the fuel

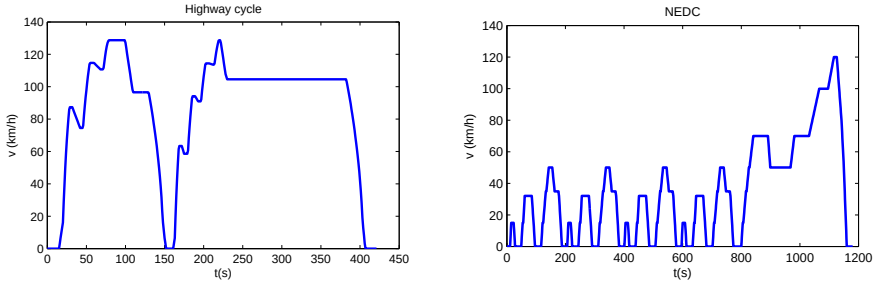

(a) Highway cycle. (b) New European Driving Cycle.

Figure 2.26: Tests cycles

Table 2.5: Final SOC.

	ECMS	MPC	Heuristic
Test 1	0.4689	0.3855	0.5083
Test 2	0.4798	0.4562	0.5045
Test 3	0.6312	0.6423	0.6491

that is actually consumed during the experiment and the remaining energy in the battery (translated to kg of hydrogen). This remaining energy can be positive (in the case that the final SOC is higher than the initial one) or negative. The fuel required to generate this energy is computed considering that the energy contained in a kg of hydrogen is 120 MJ (lower heating value) and that the fuel cell efficiency is 50%. Figure 2.27 shows the equivalent consumptions for all the cases.

From Figure 2.27 it can be seen that the equivalent fuel consumption of the MPC is the lowest one in two out of the three cases (in the other case ECMS is the best one) following the trend of the fuel consumption (Table 2.6), since the contribution of the energy stored in

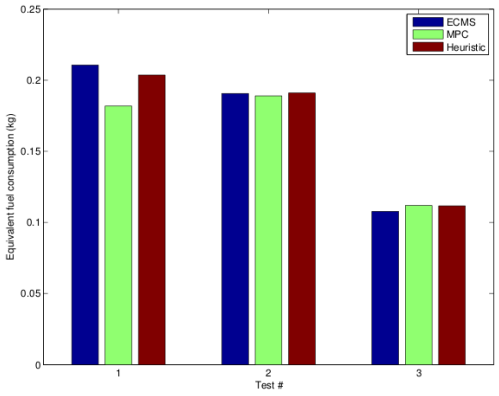

Figure 2.27: Equivalent consumptions.

Table 2.6: Hydrogen consumption (kg).

	ECMS	MPC	Heuristic
Test 1	0.245	0.178	0.261
Test 2	0.183	0.169	0.215
Test 3	0.0272	0.0357	0.0417

the battery is small. This comparison shows that the performance of MPC on the Hercules vehicle is similar to the one obtained with ECMS. The results depend on the experiment and also on the MPC parameters. Besides, these parameters can be retuned to favour a certain point, and can be easily enlarged with more output and manipulated variables in case new devices are installed.

Manipulated variables and outputs

The manipulated variables are related to the power devices of the vehicle. These are the batteries and/or UC, the fuel cell and the hydraulic brakes:

- Fuel cell power.
- Batteries power.
- UC power.
- Braking power.

On the other hand, the system outputs are:

- Motor power.
- Batteries SOC.
- UC SOC.

where the variables of the batteries and the UCs are present only if their respective device is present. All the variables were normalised to ease the setting of the target function weights.

Variable constraints

Table 2.7 show the constraints of the system variables. The power variables are expressed in watts, the power rate variables in watts per second and the SOC in per-unit.

The constraint softening parameter (ε) is set to 0.75, where a bigger ε means harder constraints. The ECR values for each variable is shown in Table 2.8. They can vary between 0 and 1, but as opposed to ε, a bigger ECR implies a softer constrain.

Variable	Min.	Max.	Var. min.	Var. max.
FC power	4000	56000	-7000	7000
Batt. power	-18000	18000	-10000	10000
UC power	-50000	70000	-30000	30000
Braking power	$-\infty$	0	-10000	∞
Motor power	-65000	65000	-	-
SOC (Batt.)	0.4	0.9	-	-
SOC (UC)	0'5	0'95	-	-

Table 2.7: Controller variables constraints.

Constraint	**ECR**
Pow. FC	0.7
Pow. FC rate	0.1
Pow. Bat.	0.4
Pow. Bat. rate	0.3
Pow. UC	0.4
Pow. UC rate	0.3
Pow. Brake	1
Pow. Brake rate	1
Pow. Motor	1
SOC Bat.	0.01
SOC UC	0.1

Table 2.8: ECR parameter.

Controller setup

Here is the criteria followed to tune the controller:

- The weight of the motor power variable should be bigger than the rest, in order to track the power reference.
- The weight of the braking power should be much bigger than the weights of the energy storage systems. This way, the braking system will only actuate when the storage systems are complete or limited by a constraint.
- The weight of the braking power rate should be almost null, as it is assumed that the hydraulic brake is powerful enough to track the decelerations of the standard cycles.
- The weight of the SOC should have a high value (same order as the braking power). With a lower value the system focuses only in tracking the motor power, dismissing the fuel consumption optimization.

The parameters of the controller are shown in Table 2.9

2.3.5. Batteries/ultracapacitors comparative

Once the use of an MPC is justified for this work, three possible energy storage systems are compared. These are: only batteries, only UC and a combination of both, as explained in Sections 2.1 and 2.3.2.

Several standard cycles, that cover all kind of driving environments (city, road and highway) were used to compare the three configurations. The results of these simulations are too long to be detailed here, and can be summarized using a mixed cycle, like the NEDC (Figure 2.26(b)).

For comparing the three configurations, three simulations were run for each one (a total of 9 simulations), changing the initial SOC. The results of the first simulation (only batteries, $SOC_0 = 0.9$) are shown in the Figures 2.28 and 2.29, where:

$$H_{2\,wasted} = H_{2\,theoretical} - H_{2\,consumed} \tag{2.23}$$

The numerical results are summarized in Table 2.10,
where:

$$Error\,ratio = \frac{\int \left(P_{motor} - P_{requested}\right) dt}{\int P_{requested}\, dt} \tag{2.24}$$

$$H_{2\,perf} = \frac{H_{2\,theoretical}}{H_{2\,consumed}} \tag{2.25}$$

The most important parameter for this system is the error ratio. In all cases this ratio is very low (about 0.5%), so any of the three types of storage could be used.

For the higher initial SOC case, the system with the best response is the one that only uses batteries. It has the worst hydrogen performance, but it fits better the reference and consumes less fuel. However, hydrogen consumption increases when the initial SOC is

Parameter	Variable type	Variable	Batteries case	UC case
Weights	Manipulated variables	FC power	10	20
		Storage syst. pow.	5	5
		Braking pow.	500	200
	Man. var. rate	FC pow. rate	80	50
		Storage syst. pow. rate	10	5
		Braking pow. rate	0'01	0'01
	Outputs	Motor pow.	1000	500
		SOC	500	100
Target points	Manipulates vars.	FC pow. (W)	8000	8000
		Storage syst. pow.	0	0
		Braking pow.	0	0
Horizons	Prediction	Pred. horiz.	10	10
	Control	Ctrl. horiz.	4	4

Table 2.9: Controller setup.

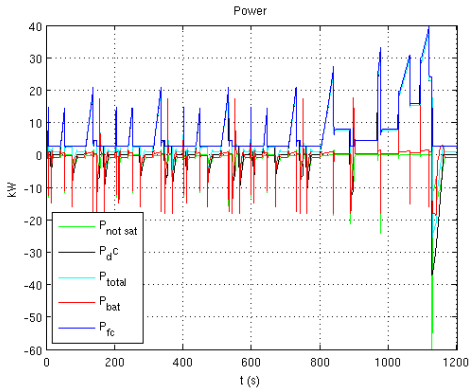

Figure 2.28: Power management in a NEDC.

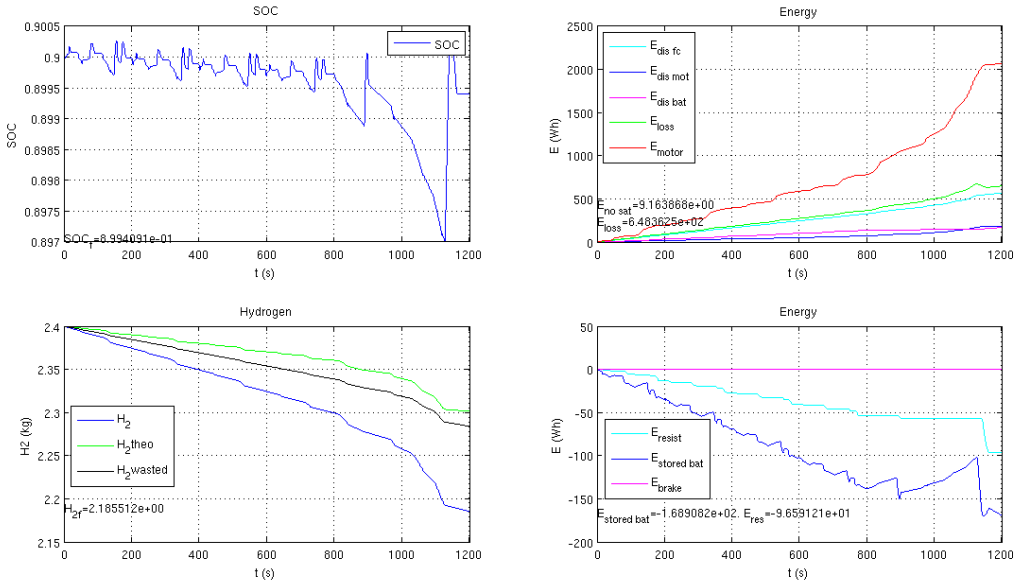

Figure 2.29: System behaviour during NEDC.

lower. On the other side, it always dissipates more energy than the other solutions, but it stores much more energy; so the hydrogen performance is better.

When the UCs are the only storage device, the system behaviour is hardly influenced by the initial SOC, due to the lower storage capacity of the UCs. However, their higher maximum recharging power allows a stronger regenerative braking, reducing the energy dissipated with the mechanical brakes. Regarding the consumption, this system has the best results in the low and medium initial SOC cases.

Finally, when both devices are used at the same time, the system does not respond as

Table 2.10: NEDC results.

Storage device	SOC_0	SOC_f	Stored E. (Wh)	H2 Cons. (kg)	Braking E. (Wh)	Error ratio	H_2 perf.
Batteries	0.90	0.90	-168.91	0.21449	648.36	0.43%	45.96%
UC	0.90	0.95	-131.96	0.21473	295.04	0.55%	46.02%
Both (Bat)	0.90	0.90	-39.34	0.21634	352.58	0.45%	46.06%
Both (UC)	0.90	0.95	-65.52	”	”	”	”
Batteries	0.70	0.74	-697.33	0.21624	749.52	0.54%	46.20%
UC	0.70	0.95	-284.49	0.21533	411.40	0.55%	46.07%
Both (Batt.)	0.70	0.75	-493.47	0.21746	668.73	0.51%	46.18%
Both (UC)	0.70	0.95	-122.67	”	”	”	”
Batteries	0.40	0.44	-736.25	0.21897	752.17	0.55%	46.47%
UC	0.50	0.95	-399.58	0.21575	493.68	0.57%	46.17%
Both (Batt.)	0.40	0.45	-469.61	0.21944	678.20	0.52%	46.40%
Both (UC)	0.50	0.95	-186.02	”	”	”	”

expected. The values do not improve in most of the cases, and sometimes they are even worse.

The simulations results show very few differences between the three energy storage systems. However, in the physical vehicle, using both batteries and UC is much more complex than using just one kind of device. Technically the system would have not only two storage devices instead of one: it would need one more converter, and this implies more work, and more potential problems. Besides, the volume of these converters will be bigger than just one, even when having a higher nominal power. Therefore, the combination of batteries and UC is not the best option. Comparing the results for the vehicles with only batteries or UCs, the latter has a slightly better response in sharp accelerations. On the other hand the higher peak power of the UCs implies a bigger power converter. In consequence, the use of these storage systems can be considered equivalent.

The differences between the other two possibilities are practically negligible. The UC system behaves better for low initial SOC, but the batteries store more energy with a better hydrogen performance, so the SOC increases to higher values, which leads to a better response. Consequently, any of both systems would be a good choice.

2.4. Conclusions

In this chapter, two real FCHVs were described. In the first case, a market electric vehicle was used as a platform to prove the feasibility of the use of hydrogen as an energy source for automotive applications. A control system was designed and tested in order to perform all the operations related to the coordinated operation of the fuel cell, the intermediate electrical storage and the power train. Experimental results obtained during the operation of the vehicle show that the power demanded by the driver is supplied in a coordinated manner using the fuel cell and the battery.

This chapter also presented an alternative configuration for this FCHV, as well as the control system developed and the experimental validation on the real vehicle. In this configuration, two FCs are used to supply power to the motor and charging the batteries in case it is needed. The control system was designed in three levels: low level controllers for each one of the fuel cell stacks, the power split between the two fuel cell stacks and a general power management system including the battery. The hybrid vehicle has been tested under real driving conditions with a good performance of the developed controllers.

A second FCHV was presented in which, using the physical structure of a commercial fossil fuel car, an electric motor was installed, powered by a FC and a set of batteries. This project was made in collaboration with several automotive and research companies (National Institute for Aerospace Technology (INTA), Santana Motor, Abengoa Hidrógeno, GPTech...). This vehicle and its power devices were modelled in Matlab-Simulink, where a MPC strategy power manager was designed. Finally, three energy storage configurations were simulated and compared.

Chapter 3

Power management of a plug-in hybrid electric vehicle based on cycle energy estimation

3.1. Introduction

Awareness about environment and the continuous rising of the fuel price have forced car manufacturers to search for alternative sources of power, with a better efficiency and decreasing harmful emissions. Some companies have launched production of full electric vehicles, like Renault Fluence, and Twizzy, or Peugeot Ion. But these vehicles are just usable in the city because of their limited autonomy, so the vehicle is not acceptable for most of the drivers. New kind of batteries and UCs are being developed with the aim of increasing the autonomy, but it seems that nowadays the best way to extend the range is by means of hybridizing, adding an extra power source such as an internal combustion engine or a fuel cell.

These new technologies will be fully operational in a few years. Users want their vehicles to perform the same or better than any Internal Combustion Engine Vehicle (ICEV). Combustion engine/electric motor hybrid vehicles have similar specifications than a ICEV, with a significant lower consumption. The first hybrid vehicles (first generations such as Toyota Prius or Honda Insight) included an electric motor that sent part of the braking energy to the batteries and powered the vehicle, helped, if necessary, by the engine.

The objective of a hybrid vehicle power management is to control the power flows accordingly to operational objectives, usually related to fuel consumption minimization, taking into account other aspects, as the final SOC of batteries or driving comfort, while satisfying operating constraints, ensuring that variables as engine torque and speed, SOC, etc., are within their limits.

The current generations of hybrid cars include the possibility of plugging the vehicle, and recharge the batteries with an external source, giving extra degrees of freedom to the control design. This is the case of the Chevrolet Volt, which is the car being studied in this chapter.

The solution proposed in this work is based on the knowledge of the operational maps of the units (motors and engine) and journey information and it tries to optimize efficiency while fulfilling driver's request. In order to do that, a two-level control scheme is proposed in this work that minimizes a cost function that penalizes the use of fuel in the engine as well as it tries to track a certain value in the SOC. It will be discussed in detail in Section 3.

3.2. System description

As told in the introduction, this chapter deals with the power management of a PHEV, in particular the Chevrolet Volt (Figure 3.1). The controller is tested on a simulator, which has been provided by the organizer of a special benchmark session scheduled at E-Cosm 2012. The simulator is quasi-static and it accounts for longitudinal vehicle dynamics and battery SOC dynamics, while the engine and electric machines are modelled using stationary maps. The Chevrolet Volt model implemented has been obtained using data made available by its manufacturer, General Motors (see for instance [48]).

Figure 3.1: Chevrolet Volt.

This simulator consists of three blocks. The first one is the *driving cycle* block. It reads the data from a driving cycle, and a virtual driver sends the torque set point to the *control strategy* block for the vehicle to track the cycle. This block is explained in section 3.3. The third one is the *vehicle model* block, which runs a quasi-static model of the powertrain and the vehicle dynamics, which is briefly explained in this section.

The powertrain architecture powering the Chevrolet Volt consists of a power-split, planetary-based system, named Voltec and shown in Figure 3.2. The system integrates three machines: an internal combustion engine (ENG), an electric generator (GEN) and the main traction machine, which is an electric motor (MOT). Both electric machines can actually work in both motoring and generating mode. The connection or disconnection of these machines is achieved by three clutches (C1, C2, C3), giving rise to four possible modes, shown in table 3.1.

The planetary gear set is implemented using static relationships among speeds and torques of each axis, neglecting the dynamics of the machines and the inertia of the gears. The generator is connected to the ring, the motor is connected to the sun and the transmission output is the satellite carrier.

The engine and electric machines are represented by their efficiency maps and the battery model implemented is based on a simple circuit model composed of a voltage source and a resistance, both functions of the SOC.

Table 3.1: Operating modes.

Mode	Engine	Clutch 1	Clutch 2	Clutch 3
1. One-motor EV	Off	Closed	Open	Open
2. Two-motor EV	Off	Open	Closed	Open
3. Range-extender	On	Closed	Open	Closed
4. Power-split	On	Open	Closed	Closed

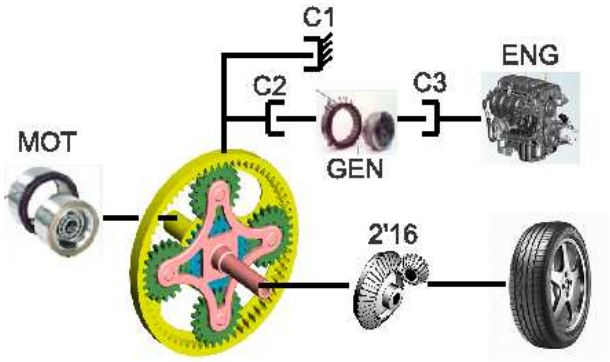

Figure 3.2: Voltec planetary gear set.

The total torque generated by the powertrain is applied to the vehicle and the actual speed is computed by integrating the standard longitudinal dynamics equation:

$$m\frac{dv}{dt} = \frac{T_{pwt} + T_{brake}}{r_{wheel}} - mg\sin\alpha - c_0 - c_1 v - c_2 v^2 \tag{3.1}$$

where m is the vehicle mass, v the speed, T_{pwt} is the powertrain torque at the wheels, T_{brake} is the mechanical braking torque, r_{wheel} the wheel radius, α the road slope and c_0, c_1 and c_2 the road load coefficients. Real operation constraints are added to the model, such as idle speed in the engine or rate limitation in the generator speed.

3.3. Controller description

The controller is divided into two levels: the upper one calculates the power that must be supplied by the engine at each moment taking into account the estimation of the energy that must be supplied by the powertrain until the end of the journey. The lower one manages the torque/speed set points for all the devices. Besides, the operation modes are changed according to some heuristic rules.

The controller receives from the driver the torque set point, and from the vehicle model the vehicle speed and the batteries SOC. It also has three more inputs. One of them is the maximum braking torque that the system is able to regenerate at any time. The rest of the braking torque should be given by the mechanical brake. The other two inputs are

approximations of the distance and the average speed of the complete cycle, which are supposed to be obtained by a GPS device.

The outputs of the controller are the set points for the speed of the generator and the torques of the motor, the engine and the mechanical brake. It also has four binary outputs, that represent the states of the three clutches and the engine on/off state.

3.3.1. Global description

The controller has two high level sub-controllers. One of them chooses the best possible mode at that moment. The second calculates the power the engine must supply, taking into account an estimation of the energy the vehicle needs for the rest of the cycle, and the batteries SOC.

As described in section 3.2, the models of the engine and the motors are based on their consumption maps. The controller should power the devices trying always to get the maximum possible efficiency, taking into account the torque set point of the driver and the constrains of the system.

Four operating modes are available. The controller must choose the best for each moment, and the power that each device must supply. The battery at the beginning of the cycle is supposed to be at its maximum value (95%), and the benchmark rules allow it to finish at 30%. Therefore, it is possible to estimate the energy that the batteries are able to supply to the vehicle.

The energy of the engine and the motors is dissipated in the friction with the air and in the mechanical brake, if its use is necessary. Some of it will also be lost by the electric devices, and part of it may be transformed into potential energy, in case the cycle starts and finishes at a different height.

The motors can only supply the energy that is stored in the battery. The rest of the demanded energy must be supplied by the engine. Some of it will be recovered by the motors in regenerative braking, but it must be obtained from the fuel.

$$E_{cycle} = E_{batteries} + E_{fuel} \tag{3.2}$$

The energy supplied by the batteries is supposed to be 'cleaner' and cheaper than the one supplied by the fuel besides being less efficient. Actually, in the *Energy and economy* section of the benchmark rules, they are weighted as shown in table 3.2.

Table 3.2: Energy and economy weights.

Total energy use (fuel+electricity)	15%
Fuel consumption	20%
Well-to-wheel CO_2 emissions	15%

Even when the *well-to-wheel* emissions per energy unit are a little higher in the case of the batteries, it is clear that the energy obtained from the fuel penalizes more than the energy obtained from the batteries. It is then obvious that the batteries should supply all the energy they are able to. Spending all this energy at the beginning of the cycle starting the engine if necessary would be an option. However, there are some inputs that will help the controller

to manage the energy in a more efficient way. These are the approximations of the distance of the cycle and the average speed. Having these data, the controller is able to estimate the energy the car needs to complete the cycle. Therefore, it is known the energy the battery can supply and an estimation of the energy for the whole cycle, so using equation 3.2, the controller will have an estimation of the energy the engine must give, supplying it in the most efficient way.

In summary, the controller has two high level sub-controllers. One of them chooses the best possible mode at that moment, and the second one calculates the power the engine should supply. A set of low level controllers manage the torque/speed set points for all the devices in the defined mode.

3.3.2. Mode selector

This module will choose the best mode at each moment in the cycle. The election will depend on the speed of the vehicle, the torque set point of the driver, the SOC of the batteries and the engine power calculated (sec. 3.3.3).

Mode description

Before describing how this selector works, it is important to explain the characteristics of all the cycles, sorted by efficiency, as well as their transitions, shown in figure 3.3.

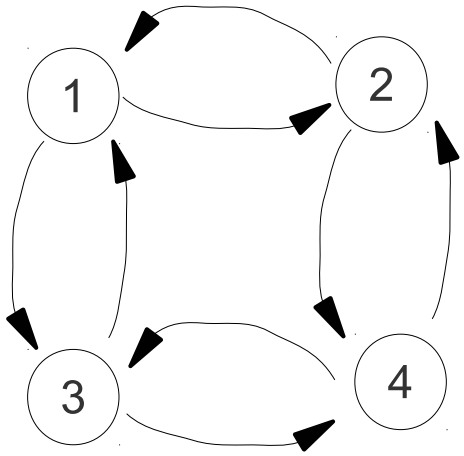

Figure 3.3: Transitions graph.

These transitions are all immediate except if the motor switches its state to 'ON'. In that case the generator is set to, at least, the engine idle speed, and the command to start the engine is set. The generator powers the engine during one second until it launches.

Mode 2: This is the most efficient mode. It will be set by default.

Mode 2 to mode 1: The torque limitation of the generator is lower than the limitation in the motor. If the driver torque set point exceeds the limit in the generator, mode 1 must be set, so the motor can supply the torque.

Mode 2 to mode 4: Both modes are similar, but in mode 4 the engine is on and it helps

the generator which can be even recharging the batteries. Fuel consumption makes mode 2 more convenient than mode 4. This transition will only take place if the batteries SOC falls below the SOC threshold (0.37) or the calculated engine power reaches the engine power threshold (20 kW).

Mode 1: The electric motor is the only one working. It is the configuration of a classic pure electric car. The motor is not as efficient as the generator, but it can give more torque and power to the powertrain.

Mode 1 to mode 2: This transition will take place if the torque set point is low enough for the generator to work.

Mode 1 to mode 3: Even when the motor is able to reach its limits in this mode, the battery could limit the power before it happens, as shown in figure 3.4. In this case, mode 3 will be set, the engine would power the generator and this new electric power will be sent to the motor, enabling it to supply the required power.

The engine is off in mode 1, so if the SOC is under the SOC threshold, mode 3 will be set.

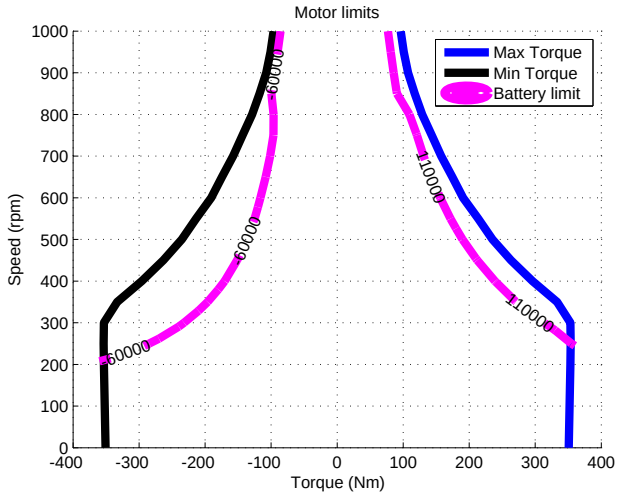

Figure 3.4: Motor limits.

Mode 3: This mode is the only in which all the torque and the power of the motor can be supplied.

Mode 3 to mode 1: This transition will take place if the batteries SOC is high enough (> 0.37) and the motor does not need more than the maximum power of the batteries.

Mode 3 to mode 4: The generator is coupled to the engine, but it is disconnected to the powertrain. This has the advantage that the engine can give the required power in the most efficient point. However, part of this power is lost due to the generator, batteries and motor efficiencies. In mode 4 the controller cannot always choose the most efficient point of work, but the torque of the engine is directly transmitted to the powertrain. Modes 3 and 4 will switch constantly when the batteries SOC gets low enough (under the SOC threshold).

Mode 4: *Mode 4 to mode 2:* This transition happens if the batteries SOC increases and reaches the threshold.

Mode 4 to mode 3: See mode 3 to mode 4.

3.3.3. Engine power controller

As described in section 3.3.1, this module calculates the power set point for the engine. This calculation is based on the energy of the batteries and on the estimation of the remaining energy of the cycle, which is the subtraction of the total energy of the cycle (sec. 3.4) and the energy already used.

The power set point is calculated minimizing the following normalized cost function:

$$J = W_{eng}\left(\frac{P_{eng}}{P_{eng\,max}}\right)^2 + W_{bat}\left(\frac{E_{bat} - E_{bat\,sp}}{E_{bat\,tot}}\right)^2 + \\ + W_{cycle}\left(\frac{E_{cycle\,rem}}{E_{cycle\,tot}}\right) \tag{3.3}$$

Where W_x is the weight of each term, P_{eng} is the set point power to the engine and $P_{eng\,max}$ is the maximum power the engine can supply. This term penalizes the fuel consumption, which, as explained in 3.3.1, should be minimized.

The SOC of the batteries may change depending on the engine energy. Therefore, it is important to include a term (the second one in eq. 3.3) where this parameter is taken into account. There, E_{bat} represents the remaining energy of the batteries, which can be easily calculated from the SOC, $E_{bat\,sp}$ is the target remaining energy (equivalent to target SOC) and $E_{bat\,tot}$ is the total energy the batteries are able to store.

The third term penalizes the remaining energy of the cycle. If this term was not included, the controller would try to deplete the batteries, and it would then supply the rest of the energy with the engine. With this term, the energy the engine supplies is better distributed, increasing the system efficiency. $E_{cycle\,rem}$ represents the remaining energy of the cycle, and $E_{cycle\,tot}$ the total energy of the cycle (sec. 3.4).

Once the cost function minimization is done, and the power is found, lower and higher limits are applied. The power cannot be higher than the maximum power of the motor. It neither can be lower than a certain value, which has been set to 18 kW. This constraint will prevent the engine from working in the lowest efficiency zone (fig. 3.6). On the other hand, if SOC gets too close to the lower limit, the current driver requested power is added to the power calculated by the controller, in order to avoid the complete discharge of the batteries.

3.3.4. Low level control

Mechanical brake torque.

The mechanical brake converts the kinetic energy of the vehicle into heat. This energy is dissipated, so the mechanical brake should be used only when the driver requires a braking torque lower (higher in absolute value) than the lowest torque limit (power limit) of the motor (battery).

$$T_{brake} = T_{sp} - T_{regen} \tag{3.4}$$

The mechanical brake torque can never take a positive value.

Motor torque.

The motor is always connected to the sun, and this is connected to the carrier by the planetary gear set. This forces the motor to track the driver's set point, taking into account the drive gearing and the efficiency of the gears. This is mandatory for the motor whatever the mode is: in case it gave less torque, the simulation of cycle would fail, and the controller would not pass the minimum performance limit and that test would not be valid.

Generator speed and engine torque.

Mode 1: In this mode, both C2 and C3 clutches are open. It means, the generator is not connected to any other mechanical device. However, the controller does not set its speed to zero, but to the engine launch speed. Some power is wasted, but it has several benefits. If the engine needs to be started, the generator has already its minimum operational speed, so it starts faster. On the other hand, speed rate is limited in the generator, and the engine launch speed is probably closer to any set point speed than the idle state. The engine is off.

Mode 2: In this mode both motor and generator are connected to the powertrain. The engine is off. The torque in the carrier is set by the driver's set point. The torque in the motor is set proportional to this value, and the torque in the ring, which in this case is the same as the torque of the generator due to the inactivity of the engine, is proportional to the set point too (eq. 3.5).

$$\frac{T_r}{\rho} = \frac{T_c}{\rho + 1} = T_s \tag{3.5}$$

Where ρ is the gear ratio. $\rho = 83/37$.

The torque in the generator is set by the torque of the motor. But the speed of the generator is directly set by the controller. Once it is set, the speed of the motor will depend on the speeds of the ring (generator) and the carrier (locked to the powertrain), so the speed of the motor, once the speed of the generator is chosen, is known (eq. 3.6).

$$\rho\omega_r + \omega_s = \omega_c(\rho + 1) \tag{3.6}$$

The speed of the generator con vary between zero and the speed of the carrier (multiplied by the gear ratio) or the speed limited by the generator speed rate constraint. The controller will choose the possible speed that minimizes the total power consumption. This is, the addition of the electric power of the motor and of the generator.

An example is illustrated in fig. 3.5. The blue line in the motor represents its torque. Eq. 3.5 forces the generator to work in the blue line shown in its graph. Each point in the generator blue line is corresponded by another in the motor line (color points in the figure). From all the possible points, the controller chooses the one that minimizes the total electric power ($P_{elgen} + P_{elmot}$).

Mode 3: In this mode the engine is on, C3 is locked and C2 is open. This is, both generator and engine are connected. The engine power controller sends a power set point. In mode 3, the engine torque and the generator speed can be controlled. The working point will be the one in which the required power is generated in the most efficient possible way.

This is, following the line plotted in fig. 3.6, which is the optimal operation line.

Mode 4: In this mode the three tractive devices are connected to the powertrain. The idea of the controller is similar to the one explained in mode 2. In this case, the generator speed and the engine torque must be set to supply the required power, in the most efficient way. The operation line of the motor is a straight line as in mode 2. However, the operation line of the engine is more difficult to find.

First, the mechanical power required at that moment is calculated, by eq. 3.7.

$$P_{mech} = T_{spring}\omega_{carrier}\frac{\rho+1}{\rho} \tag{3.7}$$

This power is subtracted to the power set point of the engine, previously calculated by the controller explained in section 3.3.3. The result of this operation is the electric power the generator has to supply. The curve of this electric power is found, and the set point torque is added. Finally this line is cut by the constrains of the generator. The resulting line will be the operation line, as shown in fig. 3.7.

3.4. Cycle energy estimation

3.4.1. Energy estimation

As mentioned before, the controller calculates the power that must be delivered by the engine based on the estimation of the energy for the complete cycle. It must be computed from the only data the controller has about the complete cycle: the approximations of the

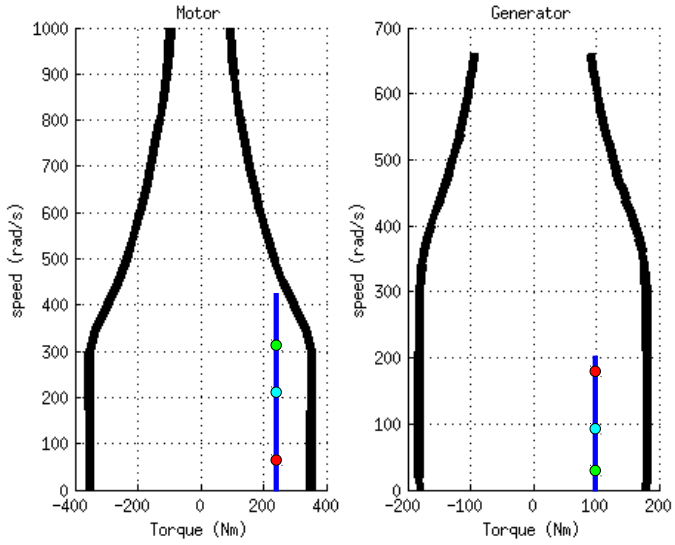

Figure 3.5: Mode 2 generator speed controller.

total distance and the average speed. This energy, generated by the engine and the battery, is lost by the non regenerative forces that interact with the car. We take them from eq. 3.1:

$$F_{nr} = c_0 + c_1 v + c_2 v^2 \tag{3.8}$$

where v is the vehicle speed.

And the power they dissipate:

$$P_{nr} = F_{nr} v = (c_0 + c_1 v + c_2 v^2) v \tag{3.9}$$

Therefore, the energy of the cycle is:

$$E_{cycle} = \int_0^{t_f} (c_0 v + c_1 v^2 + c_2 v^3) dt \tag{3.10}$$

where t_f is the final time, which can be estimated using equation 3.11.

$$t_f = \frac{D_{tot}}{V_{avg}} \tag{3.11}$$

A first approach to the solution of this integral is assuming the speed is constant during all the cycle. However, the quadratic and cubic powers will make this solution differ too much from the real value.

A second method was tried, dividing the integral into past and future time. This method had the problem that its solution depended too much on the final time approximation. And if it was lower than the real final time, the results were unacceptable.

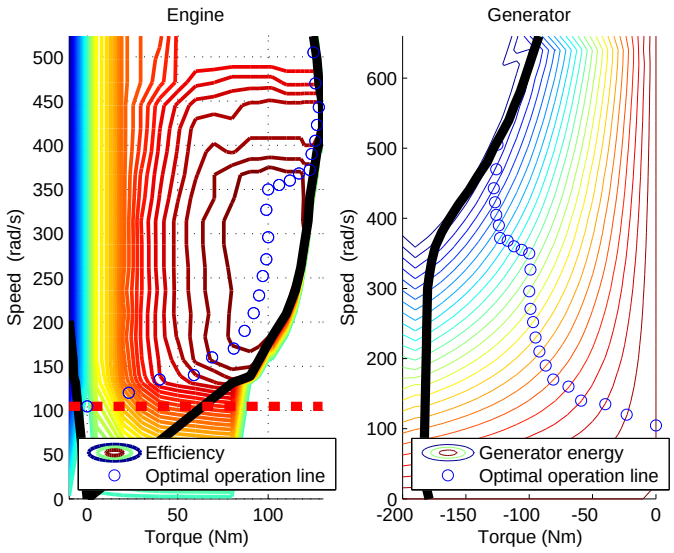

Figure 3.6: Mode 3 engine-generator optimal operation line.

A third algorithm was used. First, the integral was divided in three parts:

$$\int_0^{t_f} (c_0 v + c_1 v^2 + c_2 v^3) dt =$$
$$= \int_0^{t_f} c_0 v dt + \int_0^{t_f} c_1 v^2 dt + \int_0^{t_f} c_2 v^3 dt \tag{3.12}$$

For the first part, the solution is known:

$$\int_0^{t_f} c_0 v dt = c_0 D_{tot} \tag{3.13}$$

This will not happen for the rest of the parts, where a substitution was done:

$$v' = v - \overline{v} \tag{3.14}$$

Where v' is the new variable and $\overline{v}$ is the average speed.
For the second integral:

$$\int_0^{t_f} v^2 dt = \int_0^{t_f} (v'^2 + \overline{v}^2 + 2v'\overline{v}) dt \tag{3.15}$$

Splitting the integrals, we have:

$$\int_0^{t_f} v'^2 dt + \int_0^{t_f} \overline{v}^2 dt + \int_0^{t_f} 2v'\overline{v} dt \tag{3.16}$$

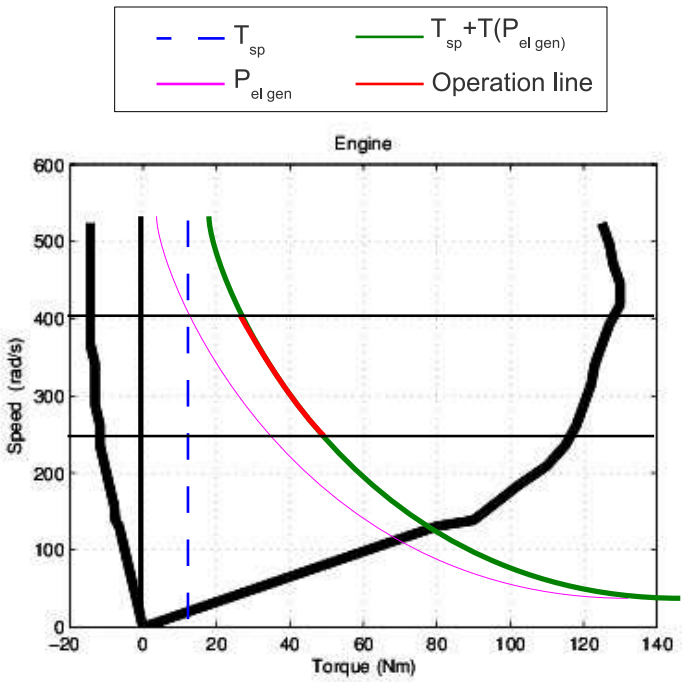

Figure 3.7: Mode 4 operation line.

Taking into account eq. 3.14:

$$\int_0^{t_f} v' dt = 0 \tag{3.17}$$

$\overline{v}$ is constant, so the second term can be solved:

$$\int_0^{t_f} \overline{v}^2 dt = \overline{v}^2 \int_0^{t_f} dt = \overline{v}^2 t_f \tag{3.18}$$

For the first term, we split the integral into past and future.

$$\int_0^{t_f} v'^2 dt = \int_0^{t_1} v'^2 dt + \int_{t_1}^{t_f} v'^2 dt \tag{3.19}$$

The first term is known. For the second term it is assumed:

$$\int_{t_1}^{t_f} v'^2 dt \approx \overline{v'}^2 (t_f - t_1) \tag{3.20}$$

Where:

$$\overline{v'} = \frac{1}{(t_f - t_1)} \left[\int_0^{t_f} v' dt - \int_0^{t_1} v' dt \right] \tag{3.21}$$

Considering eq. 3.17:

$$\overline{v'} = -\frac{\int_0^{t_1} v' dt}{t_f - t_1} \tag{3.22}$$

Concluding:

$$\int_0^{t_f} v^2 dt \approx \overline{v}^2 t_f + \int_0^{t_1} (v - \overline{v})^2 dt + \frac{\left(\int_0^{t_1} (v - \overline{v}) dt\right)^2}{(t_f - t_1)} \tag{3.23}$$

The cubic integral is solved with the same method:

$$\begin{aligned} \int_0^{t_f} v^3 dt \approx \overline{v'}^3 (t_f - t_1) + \\ + \int_0^{t_1} (v - \overline{v})^3 dt + \overline{v}^3 t_f + 3\overline{v} \int_0^{t_f} v'^2 dt \end{aligned} \tag{3.24}$$

$\overline{v'}$ was calculated in eq.3.22. So, the total energy is:

$$\begin{aligned} E_{cycle} \approx c_0 D_{tot} + \\ + c_1 \left[\overline{v}^2 t_f + \int_0^{t_1} (v - \overline{v})^2 dt + \frac{\left(\int_0^{t_1} (v - \overline{v}) dt\right)^2}{(t_f - t_1)} \right] + \\ + c_2 \left[\overline{v'}^3 (t_f - t_1) + \int_0^{t_1} (v - \overline{v})^3 dt + \overline{v}^3 t_f + 3\overline{v} \int_0^{t_f} v'^2 dt \right] \end{aligned} \tag{3.25}$$

3.4.2. Efficiency estimation

Up to this point the energy of the cycle has been calculated. However, the efficiency of the devices has not been considered. This value depends not only on the speed of the vehicle, but on how power is managed. A constant value could be considered, but it would not be a good approach.

The average efficiency of the system is easy to be measured at any time, dividing the power of the non-regenerative forces (eq. 3.9) over the power consumption of batteries and fuel. However, this value may change too much along time, so it will only be useful at the end of the cycle.

In this thesis an estimator based on the average efficiencies of other cycles is proposed. The efficiency of seven cycles were measured, as well as their average speeds. The results are shown in table 3.3.

Table 3.3: Efficiency.

Cycle	Efficiency	Average speed (m/s)
Artemis Extra Urban	0.6515	16.76
Artemis Highway	0.7032	27.64
Artemis Urban	0.2821	4.856
FHDS	0.8127	21.58
FUDS	0.533	8.752
NEDC	0.6392	9.325
US06	0.682	21.44

Based on these results, a quadratic correlation is proposed:

$$\text{Eff} \approx -0.0015 + 0.0647V + 0.0658V^2 \tag{3.26}$$

Fig. 3.8 shows the real efficiency values (black circles) and the correlation curve (blue line).

The estimator calculates the average efficiency at each moment with real data, and corrects the estimated one, increasing its weight as time passes. That is, efficiency is computed as a weighted sum of the measured value up to now and the estimation depending on the

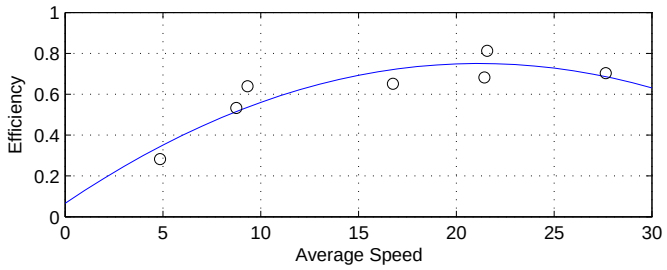

Figure 3.8: Efficiency correlation.

cycle average speed. The energy consumption will be approximated dividing the estimation of the energy for the complete cycle over the estimated efficiency.

$$\text{Efficiency} \approx \text{Eff}_{est}\frac{t_f - t_1}{t_f} + \text{Eff}_{measured}\frac{t_1}{t_f} \tag{3.27}$$

The energy consumption of the cycle will be approximated dividing the estimation of the energy for the complete cycle over the estimated efficiency.

3.5. Simulations

Two kind of tests were done:

3.5.1. Acceleration tests

In these tests the torque set point of the driver is set at its maximum or minimum value. There are two tests that measure the time the vehicle needs to change its speed from two given values: from 0 to 100 km/h and from 70 to 120 km/h. These are the most used tests in the industry.

3.5.2. Driving cycles

The car will have to track different cycles. It is mandatory not to exceed a speed error limit (1.5 m/s), an average speed error limit (0.15 m/s) and a minimum SOC threshold (0.3). A long and realistic cycle, 'VAIL2NREL' will be tracked to show how the power management is done.

3.6. Analysis of Results

3.6.1. Acceleration tests

0-100 km/h. This test was completed in 9.0 seconds.

In fig. 3.9 it is shown how the motor torque is always at its maximum value. The controller starts at mode 1 (green point at the bottom of the torque saturation line of the motor), but it switches immediately to mode 3, due to the high torque requirement. This is the limit of the system. Actually, the real car has the same performance (9.0 seconds) as the simulated model.

70-120 km/h: This acceleration test is a bit different from the others. When the car is moving at 70 km/h, the electric motors are able to supply the power, so the engine is off. However, in a certain moment, the torque set point becomes so high that the batteries' power reach its maximum limit during the time the engine needs to turn on (1 second). Therefore, the result of this test is not the best possible. A better result would have been obtained if the engine was on all the time. However, this kind of controller would entail a notable fuel consumption increment in regular cycles. Figure 3.10 show how the motor set point does not violate the power limit of the batteries, until the engine finally turns on.

3.6.2. Cycle tests

The 139 km 'VAIL2NREL' cycle was simulated. The numerical results are shown in table 3.4

Table 3.4: VAIL2NREL cycle.

E_{batt}	20.80 MJ/100km
$l/100km$	2.89
SOC_f	0.398
$v_{error\ max}$	0.245 m/s
$v_{error\ RMS}$	0.031 m/s

None of the benchmark conditions for the error and the final SOC described in section 3.5.2 are violated, so the simulation is valid. This is not a short cycle, so it needs some engine energy. This can be seen not only in table 3.4 but in figure 3.11, where the operation modes for every moment of the cycle are shown.

At the beginning of the cycle, SOC is very high, so only electric power is used, switching between mode 1 and mode 2. Then, the engine will switch on or off, as explained in section 3.3.2. Notice that the system is continuously switching between modes 1 and 2 or modes 3 and 4. But the transitions between modes 1 and 3 or 2 and 4 are not so usual. Starting the engine lasts one second, and it entails some power waste, so the controller does not order these switches the same as it requires the others.

The working points visited during the test for all the devices are shown in figure 3.12. In the graph of the motor, it is easy to see how in the zone of high torque only modes 1 and 3

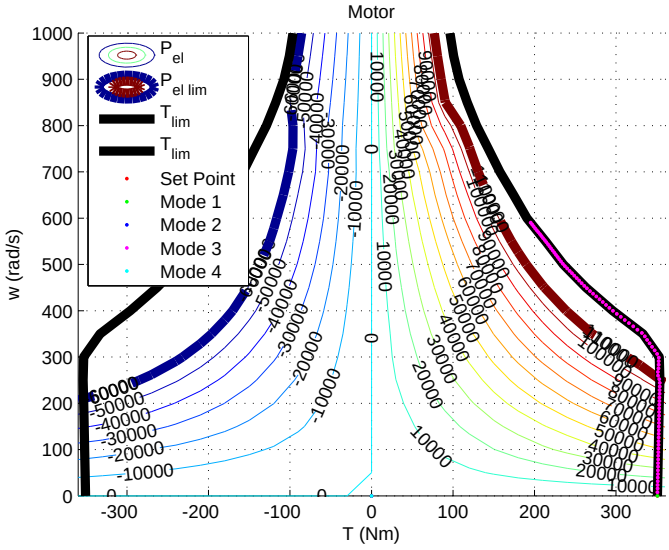

Figure 3.9: Motor working points for 0-100 km/h acceleration test.

are set, while the space in the center is shared by modes 2, 3 and 4. In the generator and the engine graphs it is shown how in mode 3 the requested engine torque and generator speed trend to fit the optimal operation line (fig. 3.6)

3.7. Conclusions

In this chapter a two-level power management controller is proposed. Two upper level controllers were designed. The first one changes the operation mode depending on the state of the vehicle (SOC, vehicle speed) and on the torque requested by the driver. The second one calculates the power required to the engine, depending on the same parameters than the first and on the estimation of the remaining energy to finish the cycle. For this variable an estimator was implemented. It calculates the cycle energy not only with the initial data of total distance and average speed: the estimation is refreshed every sample time, converging in almost the real value. The lower level is composed on a set of controllers that manage the devices minimizing the wasted power.

Several tests were simulated, in which the controller has been able to perform high accelerations and low fuel energy consumption.

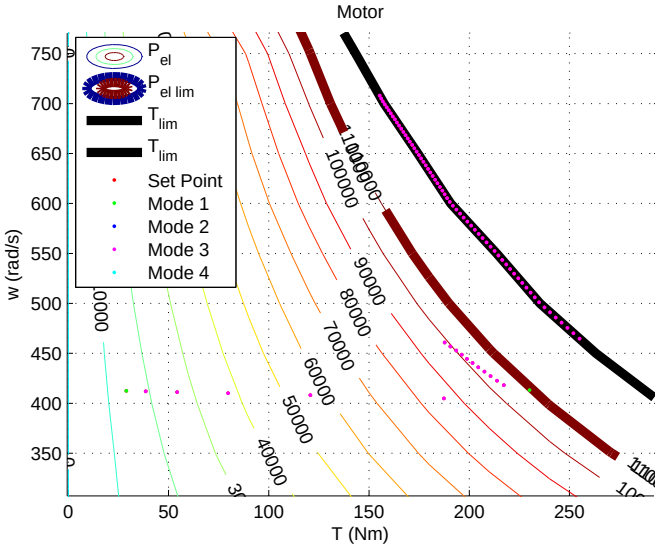

Figure 3.10: Motor working points for 70-120 km/h acceleration test.

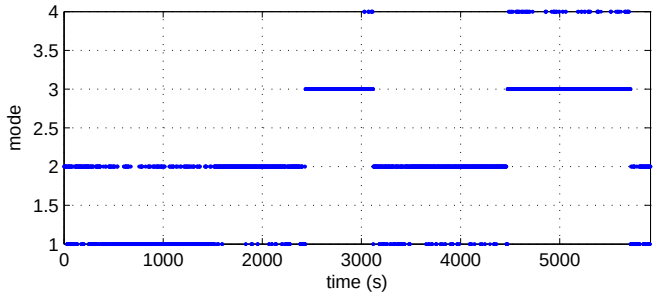

Figure 3.11: Mode switching for VAIL2NREL Cycle.

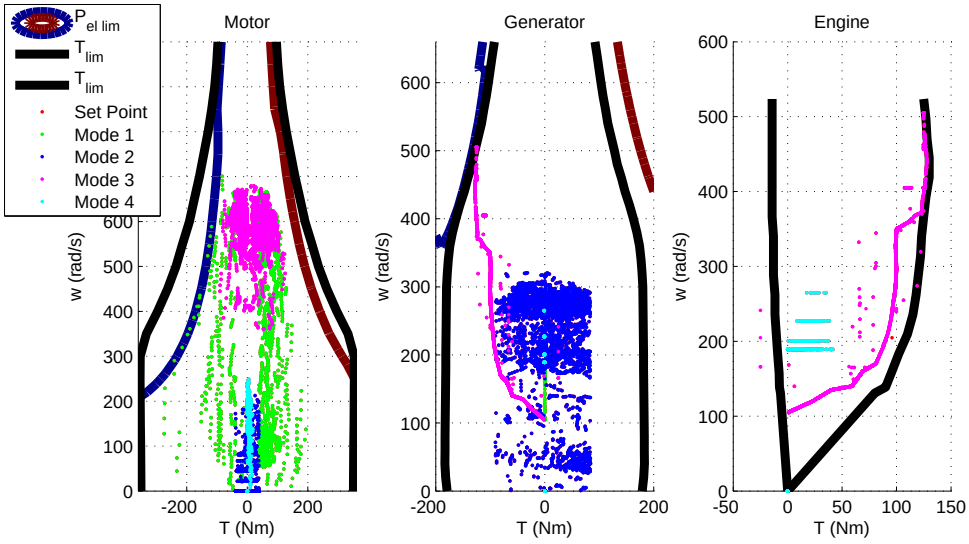

Figure 3.12: Devices working points for VAIL2NREL Cycle.

Chapter 4

The development and validation of a thermal model for the cabin of a vehicle

4.1. Introduction

Over the past few years, research has focused on the electric HV, including those vehicles with internal combustion engines or fuel cells [53, 83]. The main aim of this research has been the design of an electric system capable of running an electric motor to yield the same or similar performance as an ICEV. This research is the first step in substituting the ICEV for the HV because the final user will not accept any downgrades.

In this context, the majority of research efforts have focused on vehicle mobility and performance, which are important parameters for drivers. In addition, cars provide other types of services that make vehicles more comfortable, such as air conditioning. Even the smallest modern vehicles must include a HVAC system. Therefore, the HVAC system and its effect on the energy management of a vehicle must be accounted for in the design of a hybrid or pure EV. In particular, heating in these kinds of vehicles is different from that in the ICEV case, in which a large amount of exhaust heat is freely available. In fact, several types of HVAC systems are being studied for use in these types of vehicles. Lee et al. [68] analysed the effect of using different refrigerants for the HVAC system. Miranda et al. described a thermoelectric chip-based HVAC in [81], whereas Pethaiaha et al. proposed an HVAC system powered by an auxiliary fuel cell [94]. In addition, Ibrahim et al. [54] focused their work on developing an efficient controller. The HVAC modelling and control issue was thoroughly examined in studies by Kayyam and Farzaneh [37, 58] for conventional ICEV. However, the issue remains open for EVs and HVs.

The power consumption of HVAC systems directly depends on the thermal load of the vehicle cabin. The load in an EV or an HV is similar to that in other cars as long as the cabins do not differ from each other. The thermal model developed should be coupled with an electric compression air conditioning cycle model (under development) and other models intended for analysing power management in HVs.

Other analytical thermal models for car cabins have been established. Sanaye et al. [100] developed a thermal model coupled with an air conditioning evaporator model to simulate the control strategy for indoor air temperature. Levinson et al. [69] used a simplified thermal model to analyse the use of solar reflective car shells and explain their benefits, such as fuel savings and emission reduction. Mezrhab and Bouzidi [79]described a thermal model of a car cabin (with higher complexity) in which surfaces and the indoor air volume are divided into nodes. Fayazbakhsh et al. [38] estimated the thermal load of a vehicle cabin using a lumped-body approach. However, in none of these cases were the simulation results compared with experimental data.

4.2. Model description

The external and internal surfaces of the cabin considered in this study have been simplified. All surfaces are considered flat. This simplification has been successfully adopted in several thermal cabin models, such as those of Khayyam et al. [58], Fayazbakhsh et al. [38] and Wang et al. [118].

The car cabin used is shown in Figure 4.1, where only the indoor air and the lower base have thermal inertia. The lower base simulates the contact area between the dashboard and the seats and the indoor air.

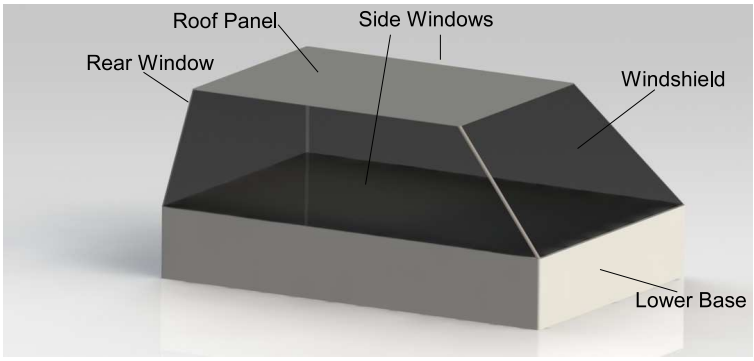

Figure 4.1: Surfaces considered in the car cabin.

The variation in the indoor air temperature is calculated by Equation 4.1:

$$m_{air} C_{p_{air}} \frac{dT_{air}}{dt} = Q_{windows} + Q_{ceiling} + Q_{base} + Q_{human} \tag{4.1}$$

where m_{air} and $C_{p_{air}}$ are the mass and the heat capacity of the indoor air respectively, T_{air} is the temperature of the indoor air, $Q_{windows}$, $Q_{ceiling}$, and Q_{base} are the convective heat flows between the indoor air and the cabin surfaces, and Q_{human} is the sensible heat supplied by the car occupants (calculated using ISO 7730 norm). The cabin scheme is presented in Figure 4.2.

The lower cabin base surface represents the dashboard, seats, and other surfaces that come in contact with the indoor air. The area of the base surface is the sum of the areas

of all of the elements considered, whose surfaces are assumed to be flat to facilitate the calculation of the convective heat transfer coefficient.

For the convective heat transfer from the windows, four different surfaces are considered: the windshield (ws), rear window (rw), left side window (lsw) and right side window (rsw). The convective heat transfer from the windows is calculated using the following equations:

$$Q_{ws} = h_{ws}A_{ws}(T_{ws} - T_{air}) \tag{4.2}$$

$$Q_{rw} = h_{rw}A_{rw}(T_{rw} - T_{air}) \tag{4.3}$$

$$Q_{lsw} = h_{lsw}A_{sw}(T_{lsw} - T_{air}) \tag{4.4}$$

$$Q_{rsw} = h_{rsw}A_{sw}(T_{rsw} - T_{air}) \tag{4.5}$$

$$Q_{windows} = Q_{ws} + Q_{rw} + Q_{lsw} + Q_{rsw} \tag{4.6}$$

where h is the convective heat transfer coefficient (see Section A), T is the temperature of the surfaces and A is the area of the window. Heat transfer from the door panels is considered negligible compared with the heat transfer from the windows.

To obtain the temperature of the windows surfaces, heat balances must be performed. The heat balances for the windshield are described by Equations (4.7) to (4.9). The heat balances for the rear window and side windows are similar. The heat fluxes are illustrated in Figure 4.3.

$$Q_{cv,e} + Q_{rd,e} = Q_{cd} + A_{ws}G_{ws,a} \tag{4.7}$$

$$Q_{cd} = Q_{ws} \tag{4.8}$$

$$G_{ws,inc} = G_{ws,r} + G_{ws,a} + G_{ws,t} \tag{4.9}$$

where: $Q_{cv,e}$ is the external convective heat flow, $Q_{rd,e}$ is the long-wave radiative heat flow and Q_{cd} is the conductive heat flow inside the window. The incident solar irradiance ($G_{ws,inc}$) is calculated using the horizontal global irradiance and the normal beam irradiance (both measured) via the method described in [30] and is discomposed into three terms: reflected ($G_{ws,r}$), absorbed ($G_{ws,a}$) and transmitted ($G_{ws,t}$) solar irradiance. The heat flows are calculated using the following equations:

$$Q_{cv,e} = h_e A_{ws}(T_{ws,e} - T_{ext}) \tag{4.10}$$

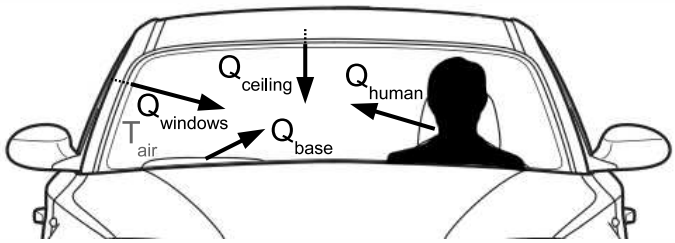

Figure 4.2: Cabin heat fluxes.

$$Q_{rd,e} = \varepsilon_{ws}\sigma A_{ws}({T_{ws,e}}^4 - {T_{sky}}^4) \tag{4.11}$$

$$Q_{cd} = \frac{k_{ws}A_{ws}}{e_{ws}}(T_{ws,e} - T_{ws}) \tag{4.12}$$

$$G_{ws,r} = \rho_{ws}G_{ws,inc} \tag{4.13}$$

$$G_{ws,a} = \alpha_{ws}G_{ws,inc} \tag{4.14}$$

$$G_{ws,t} = \tau_{ws}G_{ws,inc} \tag{4.15}$$

where T_{ext} is the ambient air temperature and T_{sky} is the sky equivalent temperature (calculated using the method proposed in [56]). The external convective heat transfer coefficient is h_e. The properties of the windows are: Area (A), thickness (e), thermal conductivity (k), long wave emissivity (ε), reflectivity (ρ), absorptivity (α), and reflectivity (τ). The Stefan-Boltzman constant is σ.

Heat transfer from the ceiling to the indoor air is calculated from a heat balance for the ceiling element:

$$Q_{cv,roof} + Q_{rd,roof} = Q_{cd,ceiling} + \alpha_{roof}A_{roof}G_{roof,inc} \tag{4.16}$$

$$Q_{cd,ceiling} = Q_{ceiling} \tag{4.17}$$

where $Q_{cv,roof}$ is the convective heat flow between the roof and the ambient air, $Q_{rd,roof}$ is the radiative heat flow between the roof and the sky and $Q_{cd,ceiling}$ is the conductive heat flow inside the ceiling. $G_{roof,inc}$ is the incident solar irradiance of the cabin roof. The absorptivity of the external surface is α_{roof}, and A_{roof} is the area. The corresponding heat flows are modelled using the following equations:

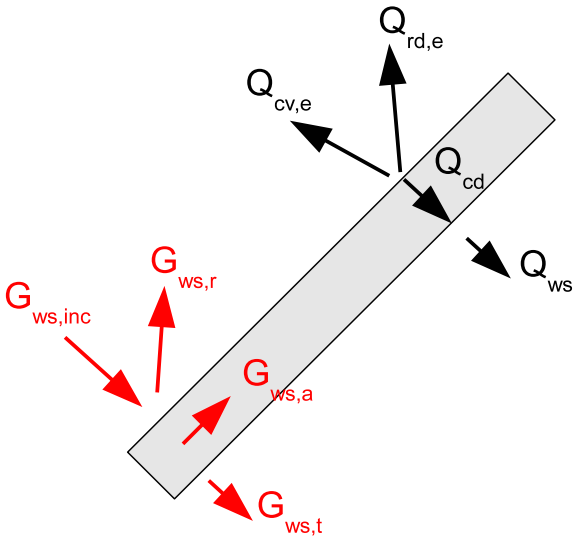

Figure 4.3: Heat fluxes in windshield.

$$Q_{cv,roof} = h_{roof} A_{roof} (T_{roof} - T_{ext}) \tag{4.18}$$

$$Q_{rd,roof} = \varepsilon_{roof} \sigma A_{roof} ({T_{roof}}^4 - {T_{sky}}^4) \tag{4.19}$$

$$Q_{cd,ceiling} = \frac{k_{ceiling} A_{ceiling}}{e_{ceiling}} (T_{roof} - T_{ceiling}) \tag{4.20}$$

$$Q_{ceiling} = h_{ceiling} A_{ceiling} (T_{ceiling} - T_{air}) \tag{4.21}$$

where h_{roof} and $h_{ceiling}$ are the roof and the ceiling convective heat transfer coefficients respectively.

The temperature of the lower base is calculated using the following equation:

$$C_{base} \frac{dT_{base}}{dt} = \alpha_{base} (A_{ws} R_{ws,t} + A_{rw} G_{ws,t} + A_{sw} (G_{lsw,t} + G_{rsw,t})) - Q_{base} \tag{4.22}$$

where T_{base} is the temperature of the lower base and C_{base} is the thermal inertia of the base elements (dashboard, seats and panels).

The assumption is that all of the solar irradiance transmitted through the windows reaches the lower base, whose bottom is adiabatic. The radiative heat transfer between the lower base, windows, and ceiling is considered negligible.

Q_{base} is the convective heat flow between the lower base and the indoor air:

$$Q_{base} = h_{base} A_{base} (T_{base} - T_{air}) \tag{4.23}$$

The convective heat transfer coefficient between the lower base and the indoor air is h_{base}.

The procedure for calculating the indoor air temperature of the cabin is illustrated schematically in Figure 4.4. The first step is to determine the solar irradiance incident on the windows and the roof, which is calculated using the global horizontal irradiance and the direct normal beam irradiance, the cars position, the cars orientation and slope (all measured), and the cabin geometry. Next, the indoor air temperature of the cabin is calculated using the incident solar irradiance determined previously, the car speed, the sky and ambient air temperatures, the cars occupants, the properties of the cabin elements, and the geometry of those elements. The secondary results obtained from the model are the internal and external window temperatures, the base temperature, the roof and ceiling temperatures, and all of the convective heat transfer coefficients. These calculations are performed for each step. The indoor air temperature of the cabin must be recirculated in a second module due to the thermal inertia of the indoor air and the lower base.

4.3. Experimental setup

The modelled vehicle is a BMW 1 series with five doors and chassis code, E87, *Spacegrau* grey (Figure 4.5).

For each surface, the radiation and conduction properties of the glass and the roof are shown in Tables 4.1 and 4.2. The radiation properties of the glass were obtained from [90],

whereas the rest of the properties were obtained from [55]. The reflectivities of the side and rear windows were readjusted, according to the experimental results.

The properties of the cabin lower base are presented in Table 4.3. The thermal inertia of the base has been adjusted based on the results of several experimental tests in which the vehicle was parked inside an underground parking garage.

A GPS device (model: MIO C230) was installed in the vehicle so that the latitude and longitude of the vehicle could be determined for every instance. The latitude and longitude of the vehicle can be used to calculate the speed and the heading angle, which provide the direction of the velocity vector. These calculations were performed using the online tool

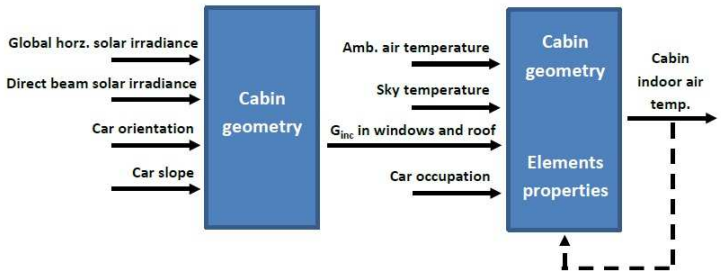

Figure 4.4: Algorithm scheme for cabin indoor air temperature calculation.

Table 4.1: Radiation properties.

Material	ε	ρ	τ	Position
Glass	0.90	0.246	0.452	Windshield
		0.100	0.311	Rear window
		0.200	0.475	Side windows
Paint	0.90	0.740	0	Roof panel

Table 4.2: Conduction properties.

Panel	Angle φ	Length (m)	Width (m)	Thickness (mm)	k (W/mK)
Windshield	60^o	0.63	1.30	6.0	1.4(Glass)
Rear Window	55^o	0.29	1.00	5.0	
Side Windows	20^o	1.45	0.29	3.0	
Roof Panel	90^o	1.80	1.10	0.5	14.9 (Steel)
				0.1	$26.3 \cdot 10^{-3}$ (Air)
				5.0	0.06 (Cotton)

GPS Visualizer [47].

The cabin temperature data were logged using Maxim DS18B20 digital thermometers, which were connected to an Arduino Duemilanove board. The main characteristics of the DS18B20 are listed in Table 4.4. The small size (Figure 4.6) of the DS18B20 provides the ability to install a temporary temperature sensor network in the vehicle. Moreover, the DS18B20 does not require calibration, and its digital communication protocol facilitates measurement, which prevents possible errors due to wire connections (noise, resistance, etc.).

Seven sensors were placed in the vehicle as shown in Figure 4.7. These sensors were arranged at different heights and were placed at a distance from each other to measure the different temperature changes in the cabin.

However, the model assumes the temperature to be homogeneous for the entire cabin. The only temperature used for the model is the temperature measured by sensor 5. This sensor was placed at an intermediate height to measure a representative temperature. The logs of the remaining sensors were used for verification, as detailed in Section 4.4.2, where the validity of the sensor 5 measurements for the cabin temperature is discussed.

4.4. Model validation

4.4.1. Testing and Simulation

Several tests were performed to establish and validate the thermal model. The first test and the corresponding simulations were performed on 6/21/2013. The external conditions (solar irradiance and ambient air temperature) are shown in Figure 4.8. The vehicle was located outdoors and had no passengers inside. The results of the simulation are shown and discussed in Section 4.4.2.

Two other tests were performed to demonstrate the validity of the model for different

Figure 4.5: Vehicle.

Table 4.3: Lower base properties.

Area	ρ	α	C_{base}
$6m^2$	0.3	0.7	144.24 kJ/K

Table 4.4: DS18B20 main characteristics.

Precision	Size	Signal
$<0.07^{o}$C	4.2x5.2x5.2 mm	Digital (1-wire protocol)

scenarios. Thus, the second test was performed under similar conditions to those of the first test, and the only difference was that the vehicle was parked indoors (no sun radiation). The external air temperature is shown in Figure 4.9. For the third test, the vehicle was in motion and had one passenger. The solar irradiance and external air temperature are illustrated in Figure 4.10, and the vehicle speed is shown in Figure 4.11.

4.4.2. Results

In this section, the results of the tests are presented and discussed. The measured and simulated values for the temperature are compared, demonstrating the variation in the temperature over the experiment/simulation time. The difference between the values presented is also quantified by calculating the maximum error and the RMS error values and then subtracting both values (Table 4.5).

Table 4.5: RMS error.

Test date	Max. error (°C)	RMS error (°C)
6/21/2013	1.89	1.53
3/21/2013	0.82	0.44
5/7/2013	4.61	3.71

For the first test, two additional graphs have been included. In the first graph (Figure 4.12), the convection heat transfer of the cabin air is compared with the solar irradiation transmitted to the cabin. In the second graph (Figure 4.13), the radiation energy absorbed by the lower base is compared with the energy absorbed by the air of the compartment (measured and simulated values).

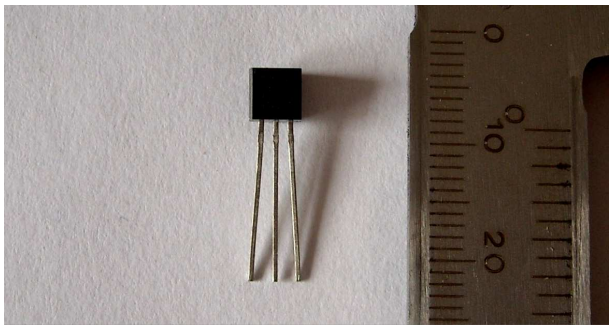

Figure 4.6: DS18B20 temperature sensor (units: mm).

In addition, the first graph includes the temperatures measured by the seven installed sensors described in Section 4.3.

Test 1. 6/21/2013

In Figure 4.14, the measurementsmade by the seven sensors in the cabin are presented with the results of the simulation. As expected, the model closely follows the temperature measured by sensor 5. The values for the remaining sensors demonstrate the validity of the sensor 5 measurements for the temperature of the whole cabin. Figure 4.14 shows that the temperature measured by sensor 5 represents an average value of the measurements at different locations of the cabin. The similarity between the simulated and the measured temperatures is quantified in Table 4.5 by the maximum and RMS errors (1.89 °C and 1.53 °C respectively).

Additional parameters were necessary to calculate the cabin air temperature. These parameters cannot be compared to any experimental data because they are difficult to measure. Nevertheless, these parameters should be equivalent and vary between reasonable limits. In Figure 4.15, the evolution of the temperature for the internal surfaces of the model is presented; the figure shows that the temperature fluctuates between approximately 25 and 60^oC. These values are reasonable for the temperature of the internal surfaces of the car, if the car has been exposed to several hours of intense solar radiation (Figure 4.8).

As explained in Section 4.2, the main objective of the thermal model is to calculate the heat flow of the internal cabin air. In Figure 4.16, this flow is presented along with the total solar irradiance transmitted.

The amount of heat absorbed by the cabin air is very small compared to the amounts of heat transferred by other mechanisms due to the small mass and thermal inertia of the cabin air. Consequently, any considerable variation between the simulated temperature and the real temperature would imply only a slight variation in heat transfer, which is the parameter of interest. In Figure 4.12, the irradiance absorbed by the lower base is shown along with the energy gained by the air in the model and in the real case. The graph verifies the aforementioned variation. The energy absorbed by the lower base is stored in the internal elements of the cabin (seats, dashboard, etc.) and gradually transferred to the cabin air by convection.

Focusing on the energy gained by the cabin air, Figure 4.13 illustrates the similarity between the simulated and the real cases.

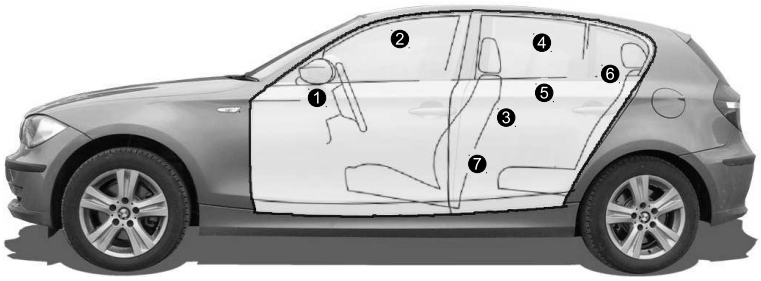

Figure 4.7: Location of the sensors.

Tests 2 (3/21/2013) and 3 (5/7/2013)

As explained at the beginning of this section, tests 2 and 3 are only included to verify the validity of the model under different conditions. The results are presented in Figures 17 and 18.

In the indoor test (3/21/2013), the vehicle was parked following a long exposure to the suns radiation. The thermal inertia of the lower base, heated during this exposure, limited the cooling of the air. Figure 4.17 shows that the dynamics of the model fit the real behaviour because the maximum error is lower than one degree centigrade for a nine-hour simulation (Table 4.5).

In the final test (5/7/2013), the temperature of the simulation rose much more rapidly than the measured temperature. This rise in the calculated temperature was caused by the human heat term (Section 4.2), which assumes that there is a constant heat flow from the occupants to the cabin air. However, the occupants in a vehicle are in contact with the seats or other internal elements of the cabin, which are part of the lower base. Therefore, part of the flow from the occupants will heat the lower base instead of directly increasing the air temperature, as assumed in this model. A more accurate human heat model would improve this result (see Section 4.5.1).

However, in Figure 4.18, both lines (simulated and measured temperatures) show a very similar evolution once the first rise is reached. Thus, the slopes of both lines gradually decrease until hour 8:53. Then, the slopes rise again. Finally, at hour 9:10, the slopes become moderate until the end of the experiment.

A certain error in the temperature calculation (3.71 °C RMS, Table 4.5) exists and provides only a small heat transfer difference, as explained in Section 4.4.2. However, the similarity of the trends exhibited by both lines demonstrates the ability of the model to calculate the heat flows in the cabin, thus fulfilling the aim of this work.

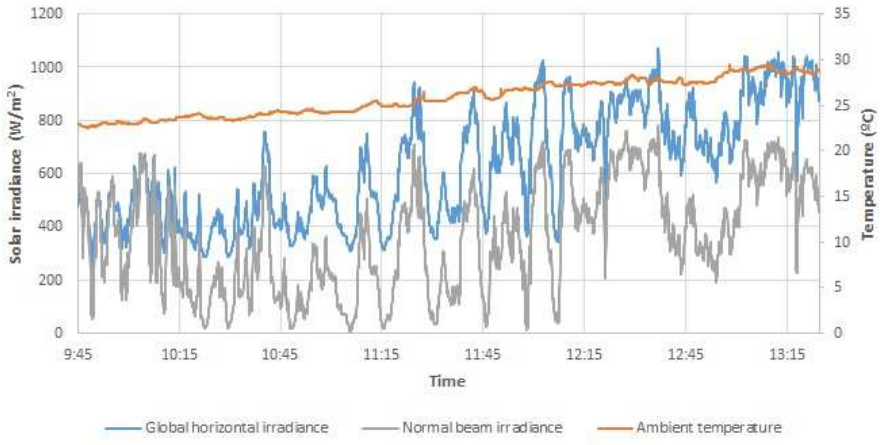

Figure 4.8: 6/21/2013 sun irradiance and ambient temperature.

4.5. Conclusions

In this chapter, a thermal model of a vehicle cabin is proposed. This model was tested under three different conditions: stopped and unoccupied while outdoors, stopped and unoccupied while indoors, and running with one person inside the vehicle. The model was verified by considering the cabin of a real car outfitted with a temperature sensor network.

The model calculates the heat transfer in the car compartment and incorporates the heat transfer in a complete vehicle model to estimate the variations in the behaviour and the fuel consumption of a vehicle due to the use of an HVAC system.

4.5.1. Improvements

As explained in the previous sections, the model achieves the aim of calculating the thermal power transferred and absorbed by the cabin air. However, the model does not consider the following aspects, which could improve the results:

- Modelling the radiative heat transfer between the lower base, windows and ceiling.
- Improvement of the human metabolic heat model by considering the heat flow between the individuals and the lower base (see Section 4.4.2).

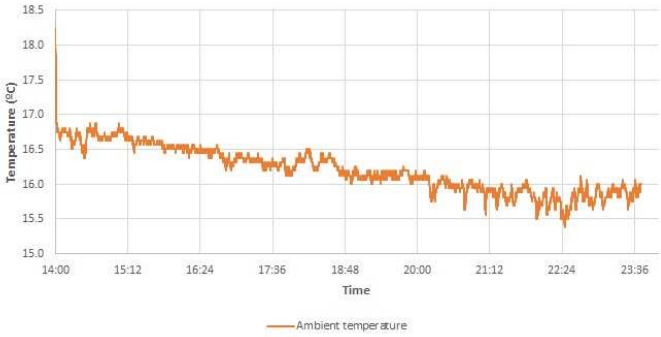

Figure 4.9: 3/21/2013 ambient temperature.

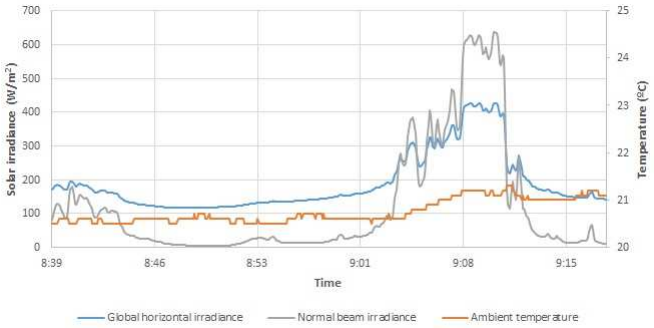

Figure 4.10: 5/7/2013 sun irradiance and ambient temperature.

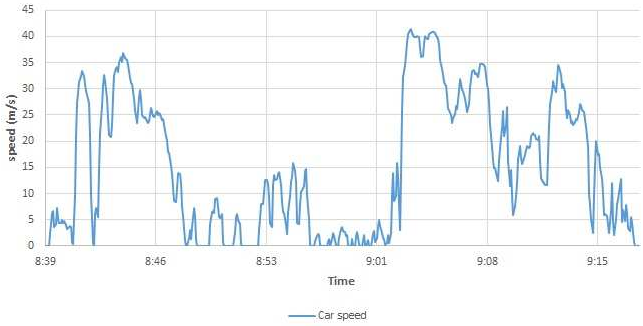

Figure 4.11: 5/7/2013 test vehicle speed.

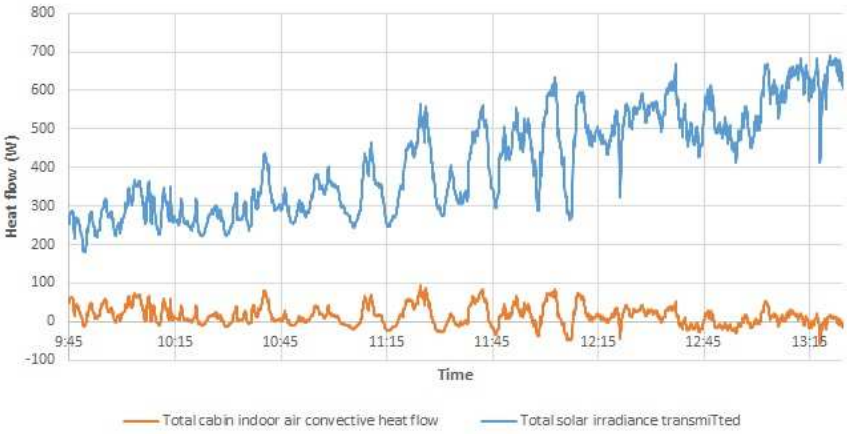

Figure 4.12: 6/21/2013 test heat flows.

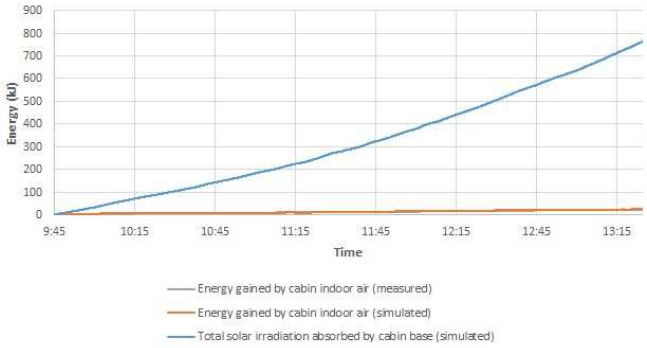

Figure 4.13: 6/21/2013 test energy gain.

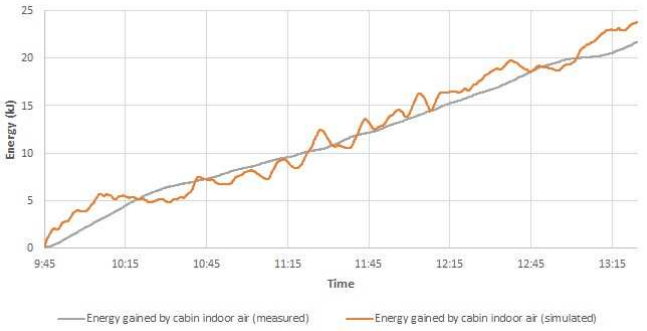

Figure 4.14: 6/21/2013 test energy gain in the cabin air.

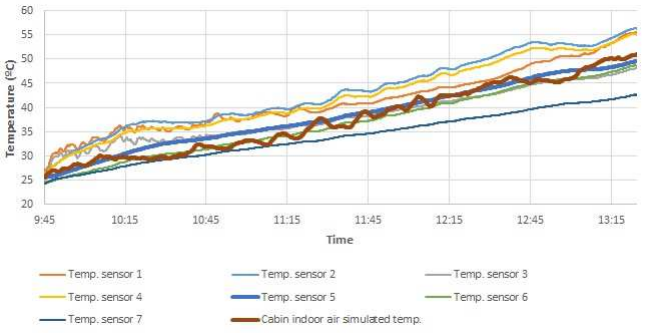

Figure 4.15: 6/21/2013 test compartment temperature.

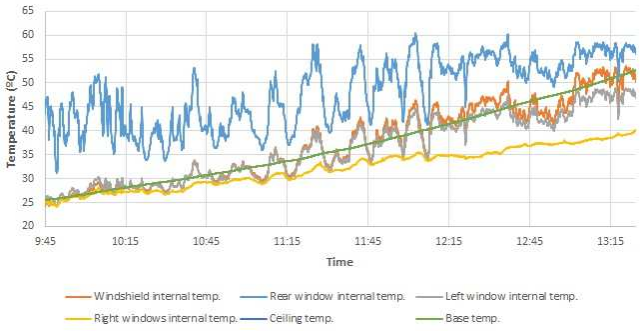

Figure 4.16: 6/21/2013 test internal surfaces temperature.

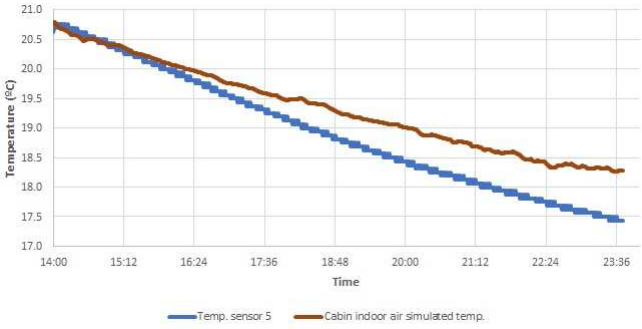

Figure 4.17: 3/21/2013 test compartment temperature.

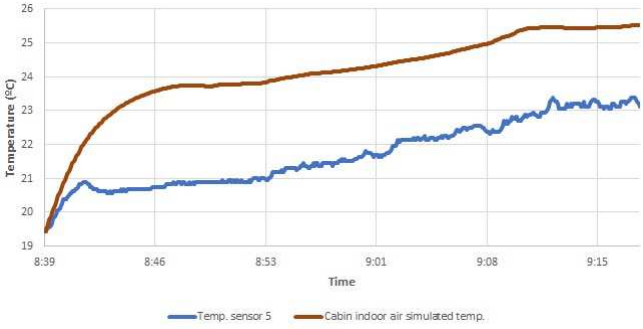

Figure 4.18: 5/7/2013 test compartment temperature.

Chapter 5

Power management in hybrid vehicles with HVAC

5.1. Introduction

In Chapter 4, a validated thermal model of a vehicle was described. The aim of this model is to measure how the performance and the consumption of a hybrid vehicle are affected by the HVAC system.

In order to perform this analysis, the thermal model has been coupled with two vehicle models. The first one is a virtual fuel cell hybrid BMW 1 series. It is assumed that the power system of the vehicle (fuel cell, batteries and motor) is the same as the ones used by the vehicle of the *Hércules* project (Section 2.3). The second model is the Volt model described in Chapter 3. In the case, it is assumed that the thermal load of the cabin of the hybrid Chevrolet Volt is similar to the BMW 1 series' one.

5.2. Air conditioning model

The air conditioning system scheme is represented in Figure 5.1. The scheme is based on a standard refrigeration cycle. The refrigeration fluid is R-134a. The evaporator extracts the thermal load of the cabin by passing an air flow through it. The refrigeration fluid absorbs the heat load and transfers it to the environment via the condenser. The refrigeration fluid is moved by the compressor. This model will be used for both vehicles.

The thermal load is divided in two terms: sensible heat and latent heat. The sensible heat is calculated using Equation 5.1:

$$Q_{sensible} = Q_{windows} + Q_{ceiling} + Q_{base} + Q_{humans} + \dot{m}_{evap}\,(1-\beta)\,C_{p_{air}}\,(T_{out} - T_{air}) \quad (5.1)$$

where $\dot{m}_{evap}$ is the air flow circulating through the evaporator. β is the air recirculation fraction (not all the air introduced in cabin is from outside). In this model, β has a value of 0.7. T_{out} is the temperature of the environment air.

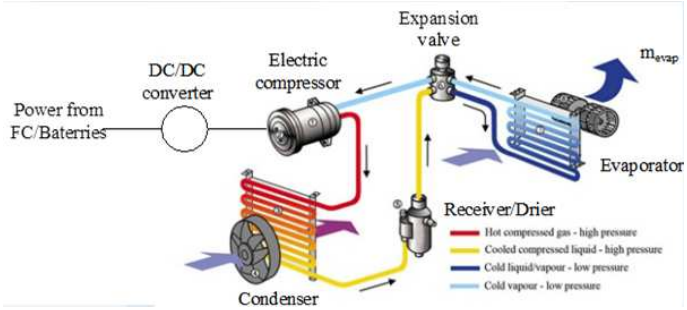

Figure 5.1: ACS scheme.

The latent heat is related to the condensation of moisture of cabin air. It is calculated using the methodology explained in [9].

The behaviour of the air conditioning system and its efficiency (Coefficient Of Performance (COP)) is affected by the cabin and the environment conditions (temperature and relative humidity), and the partial load (relation between heat demanded from cabin and nominal capacity of ACS in operation conditions). These variations from the nominal values of the HVAC are estimated using the following corrective factors [35]:

- $capTotRef\_T(T_{h,in}, T_{out})$: Corrective factor for the total refrigeration capacity, with the temperatures.
- fcp: Partial load factor.
- $conRef\_T(T_{h,in}, T_{out})$: Corrective factor for the refrigeration consumption, with the temperatures.
- $conRef\_FCP(fcp)$: Corrective factor for the refrigeration consumption, with the partial load.

where $T_{h,in}$ is the wet-bulb temperature of the air of the cabin.

The factors are calculated using the following Equations:

$$\begin{aligned} capTotRef\_T(T_{h,in}, T_{out}) = 0.000554364 \cdot T_{h,in}^2 + 0.014247648 \cdot T_{h,in} + \\ 0.0000329832 \cdot T_{out}^2 - 0.007558056 \cdot T_{out} - 0.000191711 \cdot T_{h,in} \cdot T_{out} + 0.880784506 \end{aligned} \tag{5.2}$$

$$fcp = \frac{demSenRef}{capSenRef} = \frac{Q_{evap}}{Q_{nom} \cdot capTotRef\_T} \tag{5.3}$$

$$\begin{aligned} conRef\_T(T_{h,in}, T_{out}) = 0.000161125 \cdot T_{out}^2 + 0.021414276 \cdot T_{out} - \\ 0.000411156 \cdot T_{h,in}^2 + 0.028493334 \cdot T_{h,in} + 0.000679104 \cdot T_{h,in} \cdot T_{out} + 0.1117801 \end{aligned} \tag{5.4}$$

$$\begin{aligned} conRef\_FCP(fcp) = -1.1205104 \cdot fcp^3 + \\ 1.9504979 \cdot fcp^2 - 0.0312175 \cdot fcp + 0.20123007 \end{aligned} \tag{5.5}$$

Table 5.1: ACS characteristics

Nominal Capacity	5 kW
Nominal COP	3
$\dot{m}_{evap}$	0.174 kg/s
Cabin set point temperature	25 ^oC

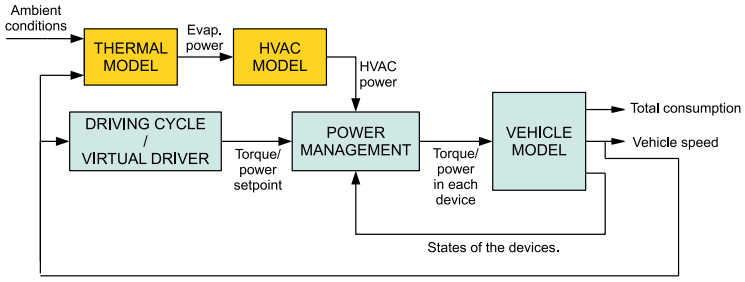

Figure 5.2: Integration of the models.

where Q_{evap} is the desired heat exchanged by the evaporator and Q_{nom} is the nominal power of the ACS.

Finally, the power of the compressor is calculated with Equation 5.6.

$$P_{comp} = \frac{Q_{nom}}{COP_{nom}} \cdot conRef\_T \cdot conRef\_FCP \tag{5.6}$$

The ACS characteristics are summarized in Table 5.1.

5.3. Integration into the model of the vehicle

Figure 5.2 shows an scheme of the integration of the thermal and the ACS models into the model of the power system.

The thermal model calculates the heat that the air of the cabin needs to transfer to the evaporator of the ACS to track the temperature setpoint. As seen in Chapter 4, the inputs of the thermal model are the ambient conditions and the speed of the vehicle, which is taken from the model of the car.

On the other hand, the HVAC model takes as input the heat found by the thermal model, calculating the power consumption of the HVAC. This variable is read by the power management controller, and considering also the torque/power request of the virtual driver, determines the power of each device. Finally, the model of the vehicle calculates the total consumption.

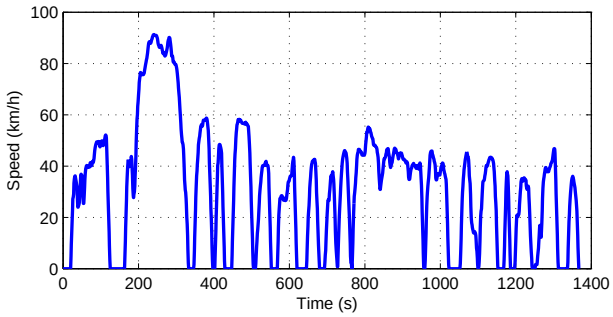

Figure 5.3: Federal Urban Driving Schedule.

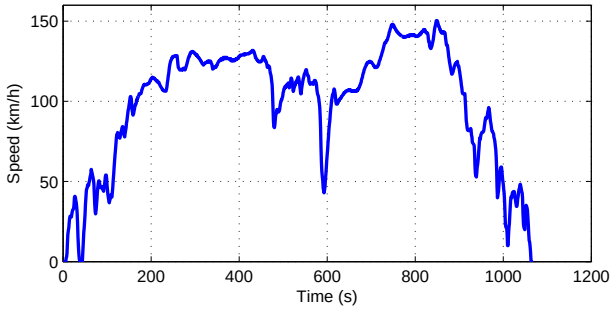

Figure 5.4: ARTEMIS highway driving cycle.

5.4. Description of the tests

Two driving cycles were used for this work. The first one is the Federal Urban Driving Schedule (FUDS) driving cycle, destined to simulate a typical urban cycle. Also known as Urban Dynamometer Driving Schedule (UDDS), this cycle was proposed by the United States Environmental Protection Agency (EPA) for light duty vehicle testing. Figure 5.3 shows the FUDS speed profile. The cycle time is 23 minutes, the total distance of the cycle is 12.07 km and the average speed, 31.5 km/h.

The second cycle is the ARTEMIS highway cycle. In this case, the cycle time is 18 minutes, the total distance is 29.55 km and the average speed is 99.7 km/h. Its speed profile is shown in Figure 5.4.

For a better evaluation of car behaviour and hydrogen consumption, these tests were performed three times consecutively, and under different initial conditions. In particular, the tests were done with an initial SOC of batteries 0.4 in some cases, and 0.8 in others.

The thermal conditions were also different for each test. As the number of occupants affects to the heat transfer in cabin, tests were performed with different number of people, varying from 1 to 5. The ambient conditions (temperature, humidity and radiation) were taken from the *typical meteorological year* in Seville (Spain) on July 19^{th}, using the software *Meteonorm*. The starting time differed from one test to the others to have smooth outside conditions (during first hour in the morning) and extreme outside conditions (at so-

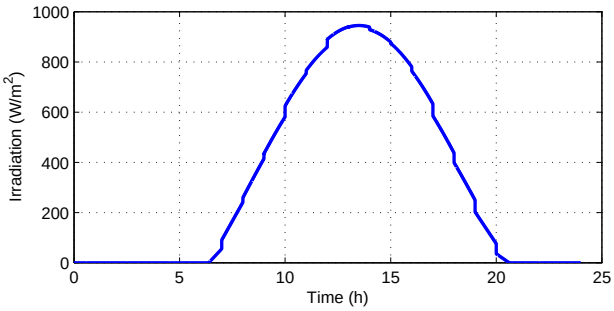

Figure 5.5: Global horizontal irradiation.

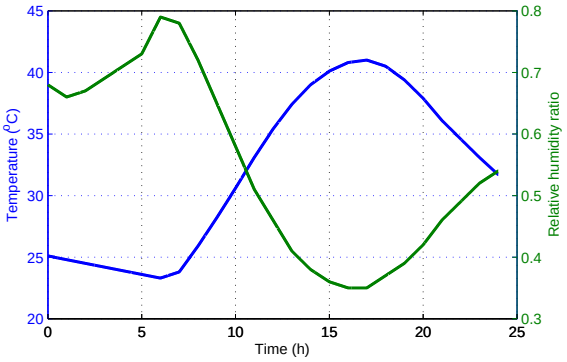

Figure 5.6: Ambient temperature and relative humidity ratio.

lar midday). The weather conditions also have influence on heat transfer processes in cabin. The global horizontal irradiation, ambient temperature and relative humidity ratio are shown in Figure 5.5 and Figure 5.6 respectively.

In Table 5.2, a summary of conditions and fixed parameters in all cases simulated is shown. The parameters considered are: weather, number of occupants and, in the case of the BMW 1, the initial SOC of the batteries. For the Volt case, the initial SOC is always 0.95 to follow the rules of the benchmark (see Section 3.3).

5.5. Results

In this section the results of the tests described in Section 5.4 are presented. Moreover, they have also been simulated assuming the ACS is not active in order to compare the fuel consumption in both cases.

5.5.1. BMW 1 series

Figures 5.7(a) and 5.7(b) show the energy supplied to the powertrain and the energy consumed by the HVAC system during the cycles, in the cases 1A and 1F, where in both

Table 5.2: Simulated cases.

Case	Cycle	Weather	Number of occupants	Initial SOC of batteries	
				BMW 1	Volt
1A	ARTEMIS highway	Extreme	5	0.8	0.95
2A	ARTEMIS highway	Extreme	3	0.8	0.95
3A	ARTEMIS highway	Extreme	1	0.8	0.95
4A	ARTEMIS highway	Smooth	5	0.8	0.95
5A	ARTEMIS highway	Extreme	5	0.4	-
1F	FUDS	Extreme	5	0.8	0.95
2F	FUDS	Extreme	3	0.8	0.95
3F	FUDS	Extreme	1	0.8	0.95
4F	FUDS	Smooth	5	0.8	0.95
5F	FUDS	Extreme	5	0.4	-

cases the HVAC consumption is sensibly lower than energy managed by the powertrain, but it is not negligible.

Table 5.3 summarizes the results of the simulations. The information shown in this table is:

- Initial and final SOC of the batteries (the initial SOC is the same with and without the ACS operating).
- Hydrogen consumption.
- Increment of hydrogen consumption.

According to the results of the simulations, some general conclusions can be obtained:

- In FUDS cycle the final SOC of the batteries is higher than the initial due to the regenerative braking and the fuel cell operation in low power/idle situations. In these situations, the fuel cell is operating at its minimum power, far from its nominal point, and consequently, with very low efficiency. This makes the urban cycle have a bigger consumption than the ARTEMIS highway.
- In both cycles, the variation of a parameter that affect to the ACS system gives a similar increment of hydrogen consumption.
- Due to the size of power equipment (fuel cell and batteries) not deficit of electric power to motor occurred in any time of cycle.

In the following subsections a more detailed analysis of the effect of the simulation parameters is done. In particular, the considered parameters are:

- Number of occupants.
- Climatology.

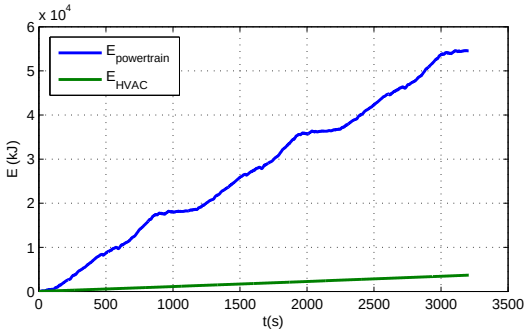

(a) ARTEMIS Highway (1A).

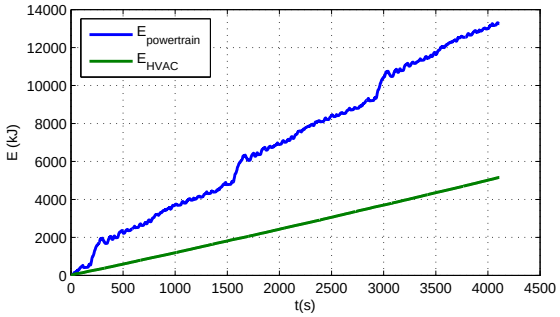

(b) FUDS (1F).

Figure 5.7: Energy supplied to the powertrain and energy consumed by the HVAC system (FCHV).

Table 5.3: Simulation results for the BMW 1 series.

Case	Initial SOC	Final SOC		Hydrogen Consumption (kg/100km)		Increment of Hydrogen consumption (%)
		Without ACS	With ACS	Without ACS	With ACS	
1A	0.8	0.598	0.562	1.50	1.64	9.2
2A	0.8	0.598	0.571	1.50	1.60	7.0
3A	0.8	0.598	0.578	1.50	1.58	5.2
4A	0.8	0.598	0.583	1.50	1.56	3.8
5A	0.4	0.408	0.405	1.97	2.15	11.5
1F	0.8	0.860	0.772	1.71	1.91	9.4
2F	0.8	0.860	0.790	1.71	1.85	7.0
3F	0.8	0.860	0.807	1.71	1.82	5.0
4F	0.8	0.860	0.821	1.71	1.80	2.9
5F	0.4	0.608	0.555	2.04	2.32	13.1

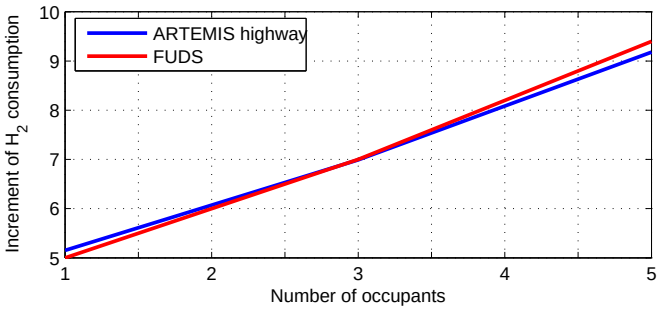

Figure 5.8: H_2 consumption increment vs car occupants.

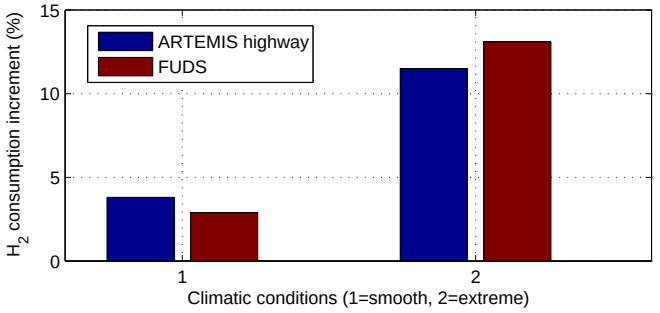

Figure 5.9: H_2 consumption increment in smooth and extreme conditions.

Number of occupants

Figure 5.8 shows the increment of the hydrogen consumption when the number of passengers varies from 1 to 5 for ARTEMIS highway and FUDS cycles.

The number of passengers affects directly to the hydrogen consumption in the two cycles. The average increment of hydrogen is 0.96% per occupant. The climatology is the same in both cycles.

Climatology

Two climatic scenarios have been considered: extreme and smooth conditions. In the extreme conditions, the solar irradiation and the ambient temperature are higher than 630 W/m^2 and 30^oC respectively, while in the smoothies conditions, the average solar irradiation and ambient temperature are 80 W/m^2 and 25^oC respectively. In all the simulations, the vehicle has five occupants. The results are shown in Figure 5.9. The increment of hydrogen consumption is similar in both cycles. The urban cycle accuses the weather change more than the ARTEMIS highway. This is caused by the speed of the car. In those conditions, the temperature of the external surface of the vehicle is higher than the ambient air temperature. At higher speeds, the convection heat transfer increments, so the surface gets cooler and the conduction heat decrements.

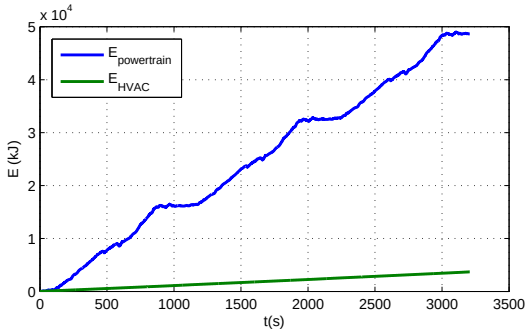

(a) ARTEMIS Highway (1A).

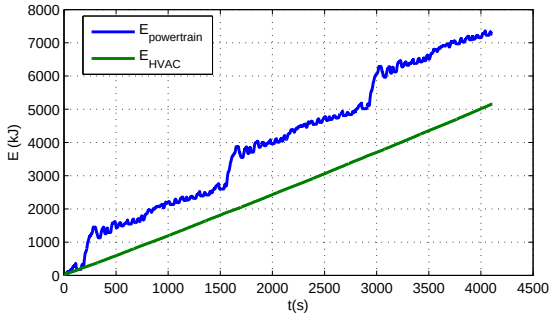

(b) FUDS (1F).

Figure 5.10: Energy supplied to the powertrain and energy consumed by the HVAC system (PHEV).

5.5.2. Chevrolet Volt

The energy supplied to the powertrain of the Chevrolet Volt and the energy consumed by the HVAC system are represented in Figures 5.10 (a) and (b), for the cases 1A and 1F respectively.

In both cases, the energy supplied to the powertrain is higher than the energy required by the HVAC. However, the difference is lower than in the previous vehicle, specially in the urban cycle.

Tables 5.4 and 5.5 show the values of the most important variables at the end of each simulation. The first one shows the results if the HVAC is off, while the second one includes the results when it is active. The information shown in these tables is:

- Speed error (maximum and RMS).
- Final SOC of the batteries.
- Real and equivalent fuel consumption.
- Increment of the equivalent fuel consumption.

According to these results, some conclusions can be obtained:

Table 5.4: Simulation results (Chevrolet Volt, ACS off).

Cycle	RMS speed error (m/s)	Max. speed error (m/s)	SOC_f	Fuel cons. $(l/100km)$	Equivalent fuel cons. $(l/100km)$
ARTEMIS highway hw x3	0.028	0.113	0.30	4.40	8.63
FUDS x3	0.035	0.086	0.71	0.00	3.97

Table 5.5: Simulation results (Chevrolet Volt, ACS on).

Case	RMS speed error (m/s)	Max. speed error (m/s)	SOC_f	Fuel cons. $(l/100km)$	Equivalent fuel cons. $(l/100km)$	Eqiv. fuel cons. increment $(\%)$
1A	0.028	0.113	0.29	4.82	9.11	5.54
2A	0.028	0.113	0.29	4.72	9.00	4.29
3A	0.028	0.113	0.29	4.64	8.90	3.20
4A	0.028	0.113	0.30	4.58	8.83	2.40
1F	0.035	0.086	0.62	0.00	5.46	37.55
2F	0.035	0.086	0.64	0.00	5.13	29.35
3F	0.035	0.086	0.66	0.00	4.84	22.09
4F	0.035	0.086	0.67	0.00	4.58	15.50

- For the ARTEMIS highway cycle, the fuel consumption is much higher than for the FUDS case (independently of the state of the HVAC). This is caused by a higher energy request by the highway cycle, and by the continuous use of the regenerative braking in the urban cycle.
- The increment of consumption is much higher for the FUDS cycle. This is a consequence of the previous conclusion: for a similar consumption of the HVAC, the relative increment is higher as long as the global consumption is lower.
- For the same reason, the results for the FUDS cycle are more affected by the variations in the tests.
- The performance is not affected by the HVAC in any case.

As in Section 5.5.1, a more detailed analysis of the effect of certain parameters is done. These parameters are:

- Number of occupants.
- Climatology.

All the scenarios for both cases are described in the mentioned subsection.

Number of occupants

Figure 5.11 shows how the number of occupants affects the fuel consumption.

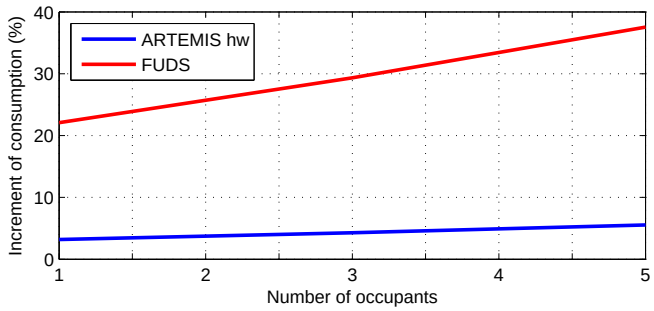

Figure 5.11: Equivalent fuel consumption increment vs car occupants.

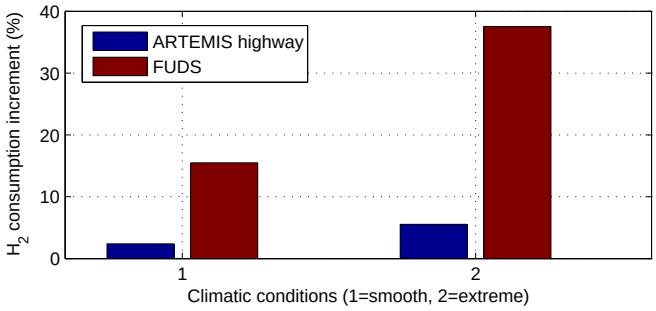

Figure 5.12: Equivalent fuel consumption increment in smooth and extreme conditions.

As expected, the variation is more prominent in the FUDS case, where it increments approximately a 7% per occupant, against the 1% that varies in the highway cycle.

Climatology

As shown in Figure 5.12, the variation of the ambient conditions affects much more to the urban cycle. This is caused by the lower speed of the cycle (see Section 5.5.1) and also by the lower consumption in the cycle, as explained in the beginning of this subsection.

5.6. Conclusions

In this chapter the effect of the Air Conditioning System in two hybrid vehicles has been analysed in terms of increment of fuel consumption. The first vehicle is a fuel cell hybrid car, while the second one is an ICEHV.

The main conclusions of the chapter are:

- The fuel consumption in a standard highway cycle is higher due to a higher electric demand of driving cycle.
- For the FCHV, in a standard urban cycle the final SOC of the batteries is higher than the initial due to the regenerative braking and the fuel cell power, when the vehicle

is idle. In contrast, the ICEHV does not need to use the engine, so it only consumes power from the batteries.

- In the FCHV, the fuel consumption in the urban schedule is higher than in the highway cycle. However, in the ICEHV case, the consumption in the urban cycle is lower than in the highway case. This is due to the possibility of stopping the engine if the vehicle is idle, or requires low power. On the contrary, the fuel cell gets damaged in the start and stop sequences, so the FCHV consumes hydrogen continuously.
- For the FCHV, in both cycles the variation of a parameter that affects the ACS gives a similar increment of hydrogen consumption, while in the Chevrolet Volt, the difference is much more important in the urban cycle.
- Due to the size of the power equipment (fuel cell/engine and batteries) no deficit of electric power to motor occurred in any time of cycle.
- Despite the use of the HVAC does not affect to the behaviour of the vehicle, the fuel consumption suffers a considerable increase, that reaches even more than 35% in some cases. Therefore this load should not be neglected in the study of hybrid vehicles. Moreover, the inclusion of this system as a new variable in the power management of the vehicle may improve the efficiency of the hybrid car in study.

Chapter 6

Modelling and torque distribution control for a four in-wheel independent driving electric vehicle

6.1. Introduction

As exposed in Section 1, ICEVs have been, by far, the main choice for the manufacturers since the invention of the car. However, in the last few years, some factors, like the rising of the fuel price or the increasing environmental awareness, are encouraging the interest for other kind of automobiles. These facts are supported by the development of new kind of batteries (LiPo, Li-ion, etc.), and the possibility of combining them with complementary power sources like ultracapacitors or fuel cells [1, 15], increasing the autonomy of the EV, which is its main limitation.

Therefore, the power source and its management are the main research threads for the EV, hybrid or pure. However, the use of electric motors instead of ICE opens new possibilities in the vehicle control. ICEVs have only one engine that is connected to the tractive wheels by several mechanical devices. These wheels are the front ones, the rear ones or the four of them, depending on the type of vehicle. The differential distributes this torque equally for all the tractive wheels.

In contrast to the ICE, the electric motors do not need an idle speed to work, which means there is no need of a clutch. This advantage and the simplicity of the own motors makes it possible to use one of them for each tractive wheel. This way it is possible to control the torque in every wheel, achieving a better dynamic behaviour for the vehicle in average driving, acting as a differential, as well as in emergency situations (traction control, stability control, etc.) [31, 50, 96]. This control can even be combined with other parameters, as castor and camber angles, or the suspension stiff, as in the scale car described in [31].

Figure 6.1: Fox vehicle.

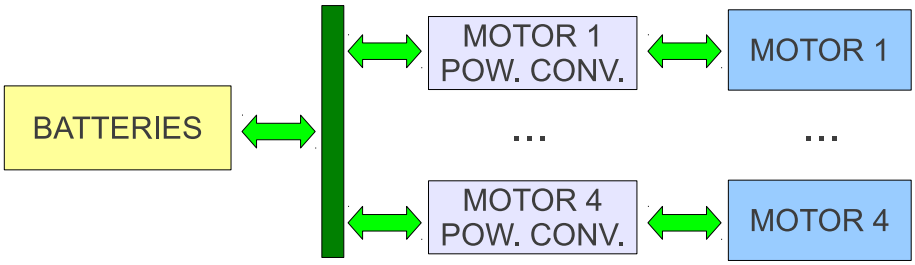

Figure 6.2: Fox power management system.

In this chapter, the vehicle FOX is introduced. This car is made as a test bench for different power management and torque distribution controllers. Two dynamic models are presented, using different modelling software: Matlab-Simulink and ADAMS. Finally, a simple torque distribution controller is presented and compared to the ICEV case.

6.2. Vehicle Description

The FOX vehicle is based on the chassis of the Silver Car S2 racing car. It was slightly modified for the best fitting of the new elements and for adding a second seat. The bodywork is the same as the original S2 car. Figure 6.1 shows the vehicle completely mounted.

The vehicle is powered by four in-wheel brushless electric hub motors. The power for these motors is supplied by a battery pack, as shown in fig. 6.2.

The components of the car are described in the following subsections.

6.2.1. Motors

The car is powered by four brushless hub motors, 7 kW power each. Its characterization, provided by the manufacturer, is shown in Fig. 6.3.

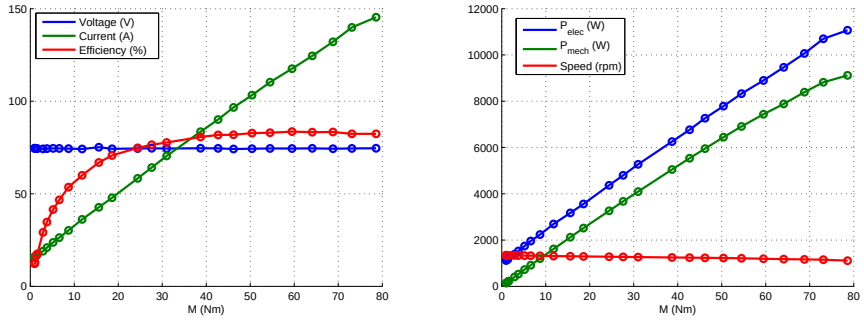

Figure 6.3: In-wheel motor characterization.

(a) Rear left motor. (b) Rear right wheel.

Figure 6.4: In-wheel motors.

Figure 6.4(a) shows the rear left motor mounted in the suspension knuckle. The wheel is coupled directly to the motor, as shown in fig. 6.4(b).

As shown in figure 6.2, each motor is driven by the controller of a power converter. These are commercial converters, which main specifications are shown in Table 6.1.

6.2.2. Batteries

The power source is composed by six packs of four cells of LiFeMnPO4 batteries. Their characteristic curves are shown in Fig. 6.5, while their main specifications are shown in table 6.2 (data supplied by the manufacturer). These batteries are controlled by a commercial Battery Management System (BMS).

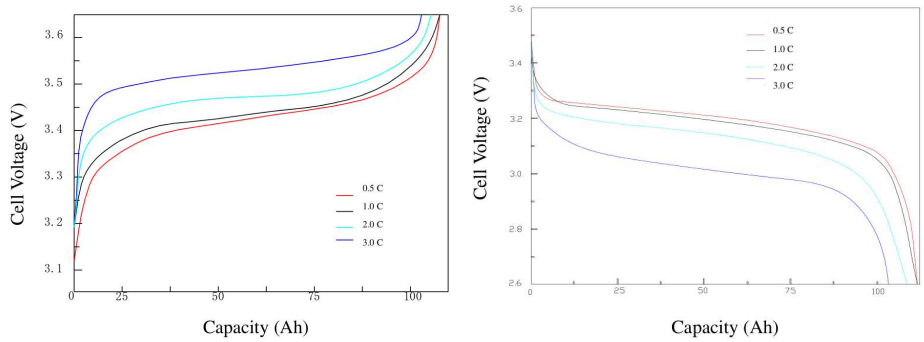

(a) Charging curves. (b) Discharging curves.

Figure 6.5: Batteries charging and discharging curves.

6.2.3. Sensors

Several sensors of different types have been installed in the car, with two aims: set the parameters of the model and, in the end of the modelling process, compare the results with the real case, and validate the model, and measure some parameters to obtain the state of the vehicle and the signals set by the driver, so the controller actuates consequently.

Vehicle behaviour sensors

- Suspension position sensors. These sensors are placed in parallel to the shock absorbers, measuring continuously their compression. The aim of these sensors is to estimate the vertical forces in each wheel. This magnitude will be used to model the forces between the tyres and the road and also to develop further controllers that consider pitch/roll angles.

  Main characteristics:

  Operating temperature range: From -50^oC to $+85^oC$

Table 6.1: Motor power converters specifications.

Frequency of Operation	$16.6kHz$.
Standby Battery Current	$< 0.5mA$.
5V Sensor Supply Current	$40mA$.
Controller supply voltage range, PWR	18V to 90V.
Configurable battery voltage range, B+. Max operating range	18V to 90V.
Analog Brake and Throttle Input	0-5 V.
Full Power Operating Temperature Range	0^oC to 50^oC
Operating Temperature Range	-30^oC to 90^oC
Motor Current Limit	400A, depending on the model.

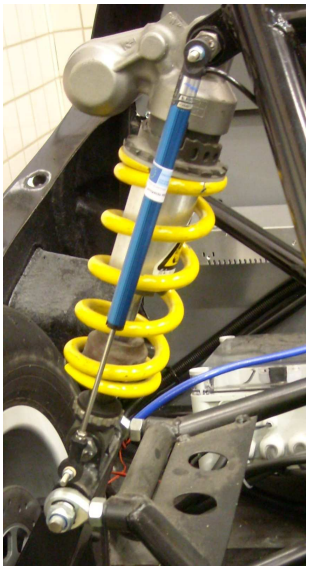

Figure 6.6: Suspension position sensor.

Maximum shaft velocity:	10 m/s (rear), 1000 mm/s (front)
Operating force:	2.45 N horizontal
Measure range:	Up to 150 mm
Nominal resistance:	$6k\Omega$ (rear), 1 $k\Omega$ (front).

- Inertial Measurement Unit (IMU) This device measures the linear and angular accelerations in the three axis, as well as the magnetic field. It also include a GPS, that will add an external position measurement. The IMU installed in the vehicle is the model 3DM-GX3-35, from the manufacturer Microstrain. Main characteristics:

  Ranks:

Table 6.2: Specifications of the batteries.

Nominal Voltage	12.8V (4X 3.2 V)
Nominal Capacity	100 Ah
Operation Voltage Range	11.2 to 14.4V
Weight	12.9 kg
Dimension	270 X 140 X 241 mm
Max Charging Current	3C
Max Discharge Current	3C (continuous) / 10C (pulsed)
Cycle Life	>2000 (80%DOD)
Operating Temperature	20 to 65 ^oC
Self Discharge Rate	<3% monthly

Accelerometers:	$\pm 5g$
Gyroscopes:	$\pm 300^o/s$
Magnetometer:	$\pm 2.5 Gauss$
GPS (acceleration):	$\pm 4g$
GPS (speed):	$500 m/s$
Aligning error:	$\pm 0.05^o$
GPS precision (speed):	$0.1 m/s$

Sensors of the driver devices

- Accelerator.
  0 to 5 volts signal, proportional to the pedal position.
- Brake pedal sensor.

  Potentiometer.
  Main characteristics:
  Nominal resistance: 10 kω
  Accuracy: 0.034%

6.3. CAD model

A CAD model of the vehicle was done. The aim of the model is double: on one hand, the devices can be allocated in the model before their real integration, checking easily not only where to fit each component, but how it affects the global physical parameters (center of mass, inertia...). On the other hand, the model will be ported to two numerical software (ADAMS and Matlab-Simmechanics) for simulating the dynamics of the vehicle [73] and design and test new controllers for the dynamics of the vehicle.

In the following subsections, the different parts of the car model are explained, detailing their physical characteristics.

6.3.1. Vehicle body

The vehicle body is composed on the chassis, and all the devices fixed at it. Two occupants are also included in this part.

Chassis

This is the only part of the car that was not modelled by the author. In fact, the model was given by the manufacturer of the vehicle (Silver Car). A confidentiality agreement was signed, so the characteristics of this body will not be detailed.

Power devices

The power devices (fuel cell, hydrogen tanks, batteries, ultracapacitors and power converters) were modelled following the physical characteristics given by their manufacturers.

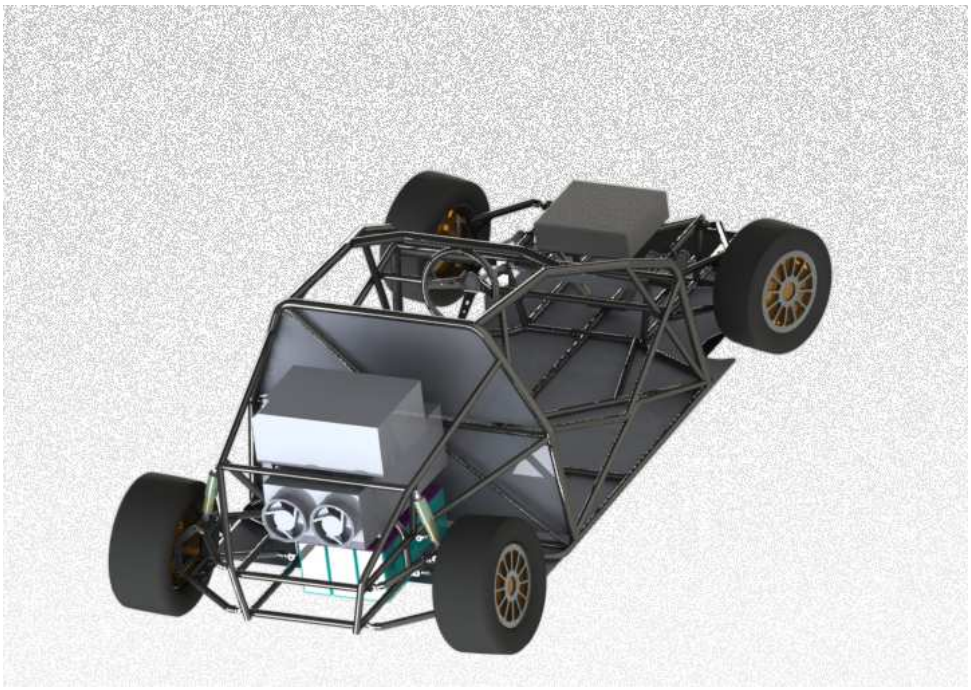

Figure 6.7: Power devices.

Unfortunately, none of the inertias of the devices were given, so a homogeneous distribution of the mass is supposed for all the elements. The devices were placed as shown in fig. 6.7, which is the location of each one in the real vehicle.

Car occupants

For the vehicle occupants, a free CAD model of a person sat in a car was included. A weight of 78 kg was assumed for each person, as well as a homogeneous mass density.

6.3.2. Suspension and steering

Both the front and the rear suspensions are of the individual double wishbone type.

Rear suspension

The rear suspension is modelled as is. As shown in fig. 6.8, the wishbones and the knuckle arms are placed according to the real vehicle. The shock absorbers were modelled as two concentric cylinders. The force element will be added afterwards in the simulator (secs. 6.4 and 6.5).

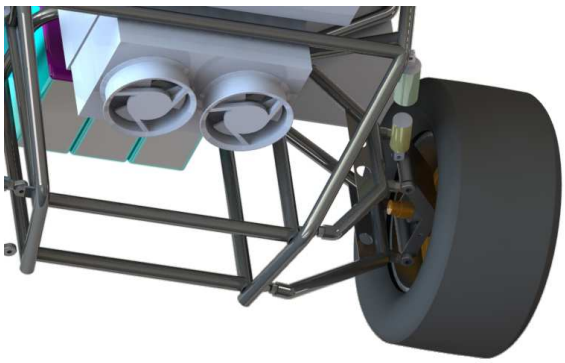

Figure 6.8: Rear suspension.

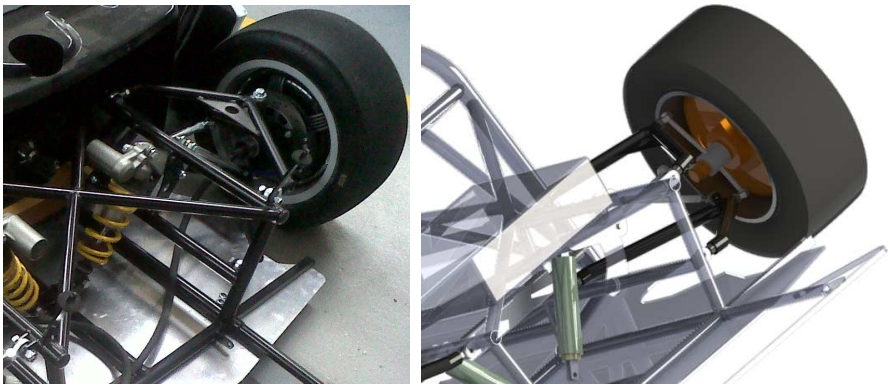

(a) Real (b) Model for ADAMS

Figure 6.9: Front suspension.

Front suspension

For the front suspension, two different configurations were modelled. The first one is the most realistic, and it will be used in the ADAMS vehicle model. The second one includes several simplifications in order to facilitate the Simmechanics model.

Figures 6.9(b) show the configuration for the ADAMS model, where the geometry of the original system was respected. The shape of the knuckle was slightly modified due to the difficulty of modelling the original one. However, its joints are placed as in the vehicle knuckles, so their behaviour does not differ from the original one.

The steering system was modelled following the vehicle rack and pinion steering mechanism (fig. 6.10).

On the other hand, fig. 6.11 shows the model for Simulink-Simmechanics. The knuckle is a simpler piece, where the vertical movement of the suspension and the rotation of the steering are separated. The shock absorbers were joint directly to the lower whishbones, in order to simplify the system.

The steering system was not included in the CAD design. It will be calculated numeri-

Figure 6.10: Steering system (model for ADAMS).

Figure 6.11: Front suspension (model for Simmechanics).

cally in the Simmechanics model (sec. 6.4).

6.3.3. Wheels

In the Simmechanics model, the reaction forces between the road and the wheels cannot be directly calculated, as it is not an specific program for vehicle modelling. Thus, the joint between those mentioned parts cannot be properly modelled directly. A modification of the CAD design is necessary for this model. It consists on two parts. One on them is a bar, that is fixed to the knuckle, and which ends in the tyre surface. The second part is the interface between the bar and the road, as shown in fig. 6.12, where the motor and the rim were hidden, in order to show the virtual bar. The Simmechanics model for the wheels will be explained in section 6.4.

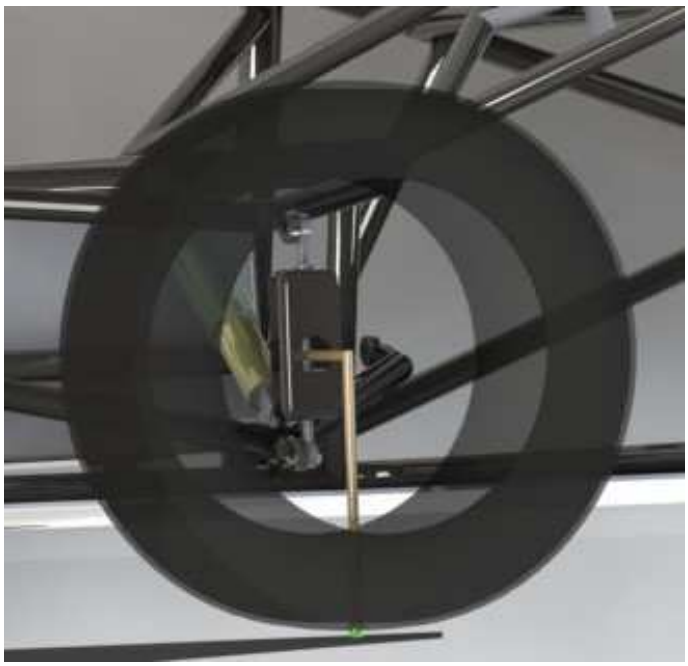

Figure 6.12: Front left wheel (variation for Simmechanics)

6.4. Simmechanics model

6.4.1. Introduction to Simmechanics

Simmechanics is a Matlab/Simulink toolbox that facilitates working with mechanical systems. This toolbox uses two basic specific blocks: bodies and joints.

A body block represents a single part of the mechanical system. These blocks contain a mathematical model of the piece (mass and inertia ellipsoid), as well as the position of the center of gravity and the orientation of the body. It also contains the coordinates and orientation of some important points of the body, like, for example, the point where a force will be applied and its direction.

A joint block represents a link between two bodies. There are several kind of joints, depending on the degrees of freedom between the linked bodies. For example, a rotative joint, which allows only the rotation movement around one direction, would be used for a hinge model.

Some other specific Simmechanics blocks are used. The most important are the actuators and the sensors. Both kind of blocks can be linked to a body or to a joint, and they are the interface between these blocks and the common Simulink blocks. The actuators apply forces/torques to bodies or joints, or force the body/joint to track a certain trajectory. These forces/trajectories are set by common Simulink blocks, connected to the actuator blocks. On the other hand, the sensor blocks measure the forces/torques or the kinematics of the bodies/joints. These blocks are connected to the common ones, which will take this data, processing it as any other Simulink variable.

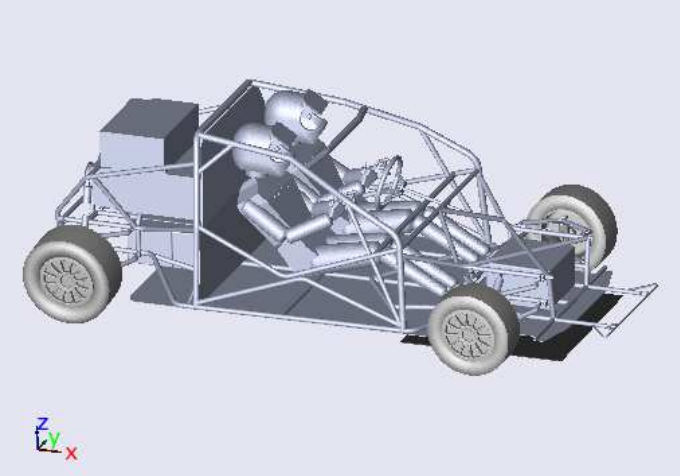

Figure 6.13: Simmechanics 3D model representation

Simmechanics incorporates a software tool, Simmechanics link, that helps porting a CAD design into a Simmechanics model. This tool not only eases modelling the mechanical system: it also provides a 3D animation, representing the modelled mechanical system.

6.4.2. Simmechanics for a vehicle model

Creating the mathematical model of a non trivial mechanical system is not a simple issue. As a matter of fact, most of the vehicle models make several simplifications, usually removing some degrees of freedom by simplifying or even blocking the suspension system. For the rest of the models, a large number of differential equations must be implemented [34, 108, 117, 125].

Simmechanics implements internally all the equations of the dynamics of the system. This does not only save time, but it prevents possible errors when enunciating the equations. Though, any change the user wants to have in the system is easily made just by changing any body/joint block. The equations will be reset automatically. *Simmechanics Link* eases this labour. If the primitive CAD design is changed, the Simmechanics model can be updated, taking into account the changes, and respecting the rest of the model.

The only limitation of this tool for its use in a vehicle model is the tyre-road interface modelling. This kind of joint is not modelled in the tool, so the user must create an equivalent mechanical system for this aim.

However, despite this inconvenient, the reasons explained above, and the possibility of utilizing any common Simulink function to manage/set/interpret the model data, make Simmechanics a very good option to model a vehicle, and develop the controllers of its driving devices.

For the FOX vehicle, the Simmechanics block diagram was imported from its Solidworks CAD design. It includes 35 bodies and 38 joints. A simplified block diagram of the model is shown in Figure 6.14.

Despite the ADAMS model described in Section 6.5 may be more accurate, a Simme-

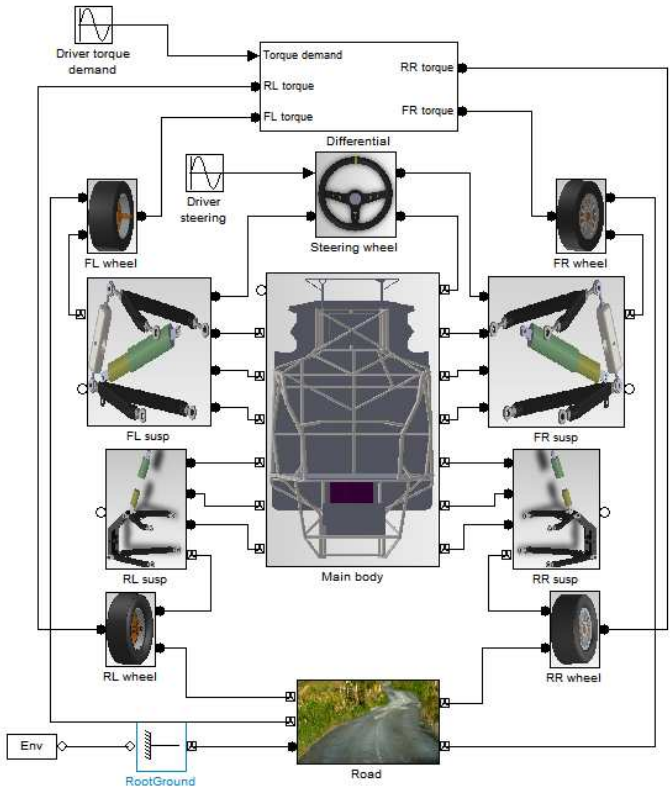

Figure 6.14: Simplified Simmechanics block diagram

chanics model is worth being done due to its versatility and simplicity. It is directly integrated in the Matlab-Simulink environment, what eases any change, addition or removal.

6.4.3. Assumptions and simplifications

In order to simplify the model, these assumptions were done:

- All the parts of the vehicle are rigid bodies, including the tyres.
- The occupants of the vehicle are also modelled as rigid bodies, fixed to the chassis.
- The force between the tyre and the road is applied at the lowest point of the center circumference of the wheel (the green point in Fig. 6.15).
- The front knuckles were modified. Instead of having three spherical joints, they have three rotative joints. Two of them allow the movement respect the wishbones. The third joint allows the steering movement.
- The vehicle always moves over a flat surface .
- The air friction force is considered only for the longitudinal axis.

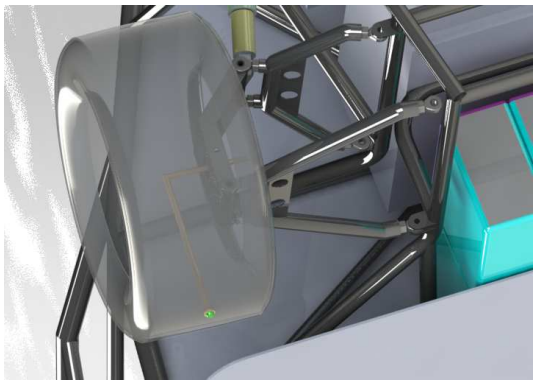

Figure 6.15: Wheel-road forces application point

6.4.4. Reference systems

Before describing the model, it is necessary to define some reference systems, important for some parts of the model. The z axis is perpendicular to the ground, and parallel for all the cases, so it will not be included in the descriptions. All the systems are summarized in Figure 6.16

Global reference system (x_G, y_G): It is an inertial reference system, where the origin is located in the starting point of the mass center of the vehicle.

Center of gravity reference system (x_{CG}, y_{CG}): This system has its origin in the mass center of the vehicle, while the x_{CG} axis is oriented to the longitudinal axis of the car.

Wheel reference systems (x_i, y_i): There is one reference system of this type per wheel. The subscript i is defined as fl, fr, rl, rr, depending on the wheel (forward and rear, left and right). The origin of this system is placed in the contact point between the wheel and the road (see Section 6.4.3). The x axis is oriented to the longitudinal axis of the wheel.

Wheel velocity reference systems (x_{wi}, y_{wi}): As in the previous case. the subscript i is defined as fl, fr, rl, rr. The origin of this system is also placed in the contact point between the wheel and the road. However, the x axis is oriented to the speed vector of the wheel.

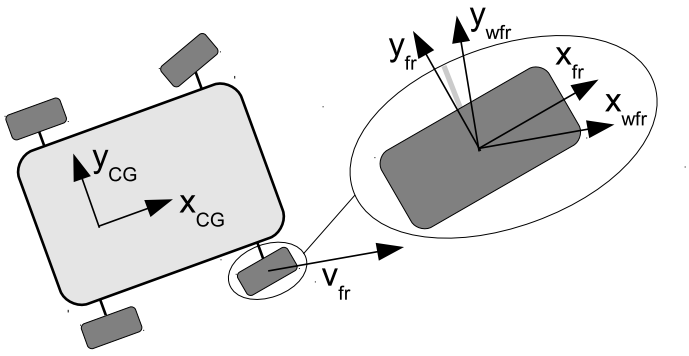

Figure 6.16: Reference systems

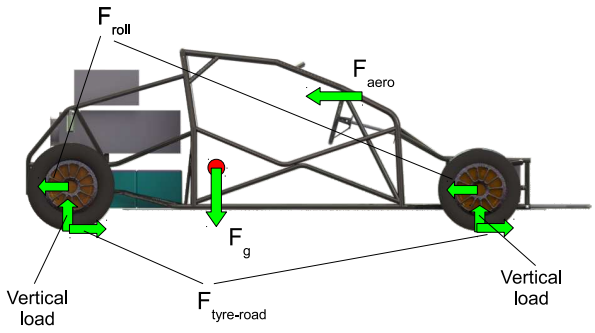

Figure 6.17: External forces.

6.4.5. External forces

Fig. 6.17 show the external forces applied to the vehicle.

Where F_g is the force of gravity, F_z the vertical load, F_{roll} the rolling resistance, F_w the horizontal road to wheel force and F_{air} the air resistance. These forces are described in the following subsections.

Force of gravity

The force of gravity is modelled as a negative vertical force, applied to the center of mass, which value is proportional to the mass of the body:

$$F_g = -mg \tag{6.1}$$

Where $g = 9.81 m/s^2$ is the gravitational acceleration. This force is automatically calculated by the Simmechanics toolbox.

Vertical load

This force is applied to the tyres, and it consists on the reaction of the road to the perpendicular forces of the tyres. This forces are calculated by the toolbox so they do not violate the tyre-road planar joints (see sec. 6.4.7).

Rolling resistance

This force is caused by the non-elastic effects of the tyre as it rolls. Part of the force applied to the tyre deforms it, and not all of it is recovered after removing the pressure. Thus, part of that force is lost. In analogy to the well-known sliding resistance, the rolling resistance can be modelled as a coefficient times the normal force.

$$F_{roll} = f_{roll} F_z \tag{6.2}$$

Where f_{roll} is the described coefficient, and F_z is the vertical load.

Friction road-tyre force

This force is applied from the road to the tyres, and it opposes to their linear movement. It is necessary to implement a tyre model to estimate this force. This model is described in Sec. 6.4.7.

Air resistance

When moving, the vehicle has to displace the air contained in the volume the car is going to occupy. Thus, a force is applied from the vehicle to the air. The reaction of this force must be included in the model. It is modelled as a force applied in the center of the front area of the car. This force depends on the front area surface, and the shape and the speed of the vehicle:

$$F_{aero} = \frac{1}{2} C_{ax} S_{front} \rho_{air} v_x^2 \tag{6.3}$$

Where $S_{front} = 1.48m^2$ is the front area surface of the vehicle, $\rho_{air} = 1.16kg/m^3$ is the density of the air, v_x is the longitudinal speed of the car, and $C_{ax} = 0.3$ is the drag factor of the vehicle, which depends on its shape. This coefficient is difficult to calculate, and it was taken from known values of similar vehicles.

6.4.6. Wheel model

The main problem of Simmechanics when modelling a vehicle is the wheel-road interface (see sec. 6.4.2). Simmechanics is thought for rigid body systems, and it does not include a good tool to model the interaction between the wheels and the road. Due to this fact, a mathematical model of this interaction was implemented and added to the system, using body and joint sensor/actuator blocks.

In the Simmechanics model of the FOX, the wheel is substituted by the mechanical system shown in Fig. 6.18.

In this figure, a front wheel is represented. The rear wheels differ only in the knuckle, which does not have the steering rotational joint.

A bar substitutes the wheel. This bar is linked to another auxiliary body by an universal joint, as well as this body is linked to the road by a planar one. All the forces between the tyre and the road will be applied in the mentioned auxiliary body. This body is placed in the lowest middle part of the tyre.

As explained in section 6.4.5, the vertical load is calculated by Simmechanics. Then, the aim of the model is to calculate the horizontal force between the road and the tyre, and the spinning speed of the wheel.

A large sort of tyre models can be found in mechanical publications. Some of them are based on the physics of the tyre. The LuGre model [22], for example, is based on the coulomb friction. Others reduce the tyre into a simpler system. The most popular model of this type is the brush model [91], where the tyre is 'converted' into a rolling brush (see fig. 6.19).

On the other hand, several models are based on experimental data. This is the case of Pacejka's magic formula [91], which is probably the best method so far. However, its

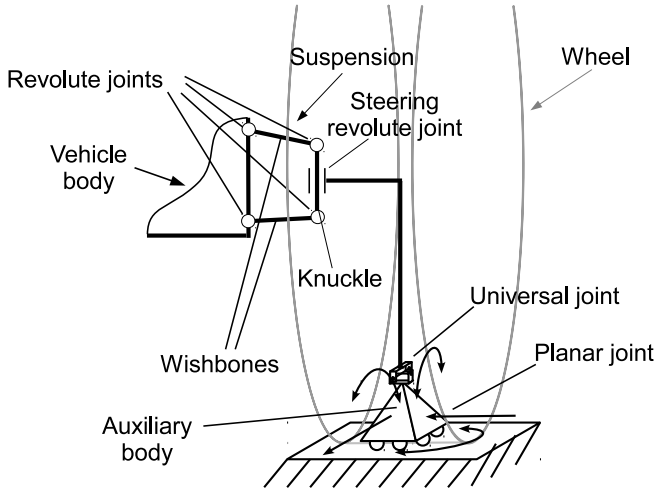

Figure 6.18: Wheel model scheme.

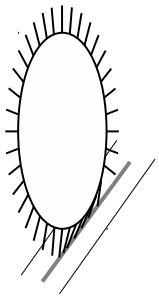

Figure 6.19: Brush tyre model.

large number of parameters makes it difficult to be set properly without using some specific testing devices. Burckhardt model [19, 74] is also based on empirical results. Although it is not as accurate as Pacejka's, it is appropriate for the kind of tests that are going to be done (moderate speed and driving conditions), and it is significantly easier to set up. Therefore, it is the method used for this model.

The steps for the calculation of the force via the Burckhardt model are explained in the following subsections.

Measured data

The data measured in each wheel is the angular speed, the speed vector, the direction of the wheel and the vertical load on the wheel.

In the Simmechanics model, the four magnitudes are measured with sensor blocks. In the real vehicle, the first one is measured with a speed sensor installed in the motor. The second and the third ones are calculated from the data from the IMU, the geometry of the

car and the steering angle. Finally, the vertical load is estimated from the shock absorber length measurement.

Force and speed vectors

In Figure 6.20(a), two velocities are shown. v_w is the speed of the wheel. On the other hand, the equivalent velocity (v_r) is a virtual speed, which direction is coincidental to the x_i axis. Its module is the product of the wheel rotational speed and the effective wheel radius (r_{eff}) (Eq. 6.4). The effective wheel radius is 253 mm and 270 mm for the front and the rear wheels respectively. The angle between v_r and v_w is the slip angle (α in Figures 6.20 (a) and (b)). The use of this angle for the calculations is explained in the following subsection.

$$v_r = \omega_{wheel} r_{eff} \tag{6.4}$$

In Figure 6.20(b) the force the road applies to the wheel is represented as F. F_L (F_S) is the longitudinal (side) components of the force, respecting the wheel velocity reference system. Finally, F_{wL} is the longitudinal component of the force, respecting the wheel coordinate system.

Wheel slip

In the Burckhardt model, the force is calculated from the relative movement between the tyre and the road. This movement is depicted by two coefficients: longitudinal and side slip. The longitudinal slip is defined as the difference between the longitudinal component of the equivalent velocity and the longitudinal speed of the wheel, divided by the biggest of these magnitudes. On the other hand, the side slip is defined in a similar form in the driving case, but it is simplified to the tangent of the slip angle in the braking case. Both coefficients vary between 0 and 1. The mathematical expressions for all cases are shown in Table 6.3.

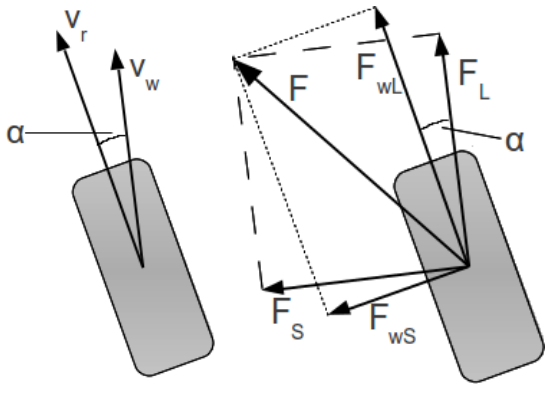

(a) Speed (b) Forces

Figure 6.20: Wheel diagrams

Force calculation

The force applied to the tyre, according to the Burckhardt model, will depend on the vertical load, which is known, and the lateral and side friction coefficients (μ_L and μ_S), that depend on the longitudinal and side slips:

$$\mu_L = \mu_{Res}\frac{s_L}{s_{Res}} \tag{6.5}$$

$$\mu_S = \mu_{Res}\frac{s_S}{s_{Res}} \tag{6.6}$$

Where:

$$s_{Res} = \sqrt{{s_L}^2 + {s_S}^2} \tag{6.7}$$

Looking at the expressions in Table 6.3 it is easy to see that S_{Res} still varies between 0 and 1. μ_{Res} is defined as:

$$\mu_{Res} = c_1 \cdot (1 - e^{-c_2 s_{Res}}) - c_3 \cdot S_{Res} \tag{6.8}$$

The values of the coefficients c_1 to c_3 depend on the type of road (asphalt, dirt, snow...) and of its conditions (dry, wet, etc.). Several sets of parameters for diverse conditions can be found at [62], pg. 322. Figure 6.21 shows a comparative of the resultant friction coefficient against the resultant slip for different situations. Al the graphs have a similar behaviour: when the resultant slip starts increasing, the friction coefficient, and so the friction force, increase. However, it reaches a maximum, and the friction decreases slowly. It is also evident the difference between the friction of the asphalt or the cobblestone roads and the one with snow.

The longitudinal and lateral forces are calculated using Equations 6.9 and 6.10.

$$F_L = \mu_L \cdot F_z \tag{6.9}$$

$$F_S = \mu_S \cdot F_z \tag{6.10}$$

Where F_z is the vertical load. In the Simulink model, once the friction force is found, F_{wL} and F_{wS} are calculated (it is simple, known α) and they are applied to the Simmechanics model making use of a joint actuator.

Table 6.3: Slip calculation.

	$v_r cos\alpha \leq v_w$ (Braking)	$v_r cos\alpha > v_w$ (Driving)
Longitudinal Slip	$S_L = \frac{v_R cos\alpha - v_w}{v_w}$	$S_L = \frac{v_R cos\alpha - v_w}{v_R cos\alpha}$
Side Slip	$\frac{v_R sin\alpha}{v_w}$	$tan\alpha$

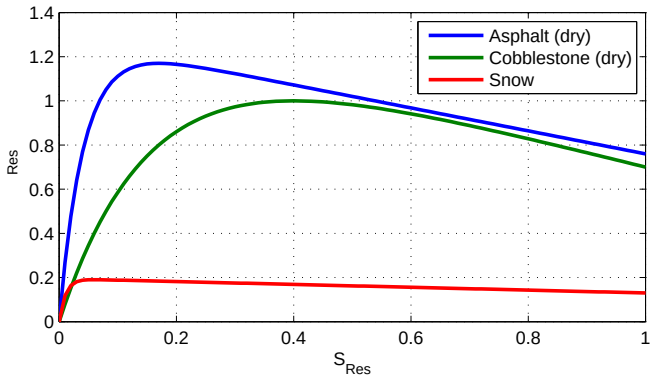

Figure 6.21: Resultant friction coefficient for several scenarios.

Finally, the torque that will move the wheel is calculated. It is found using the torque balance expressed in 6.11:

$$T_{wi} = T_{drive_i} - F_{wL_i} \cdot r_{eff_i} \tag{6.11}$$

Where the subscript i indicates the wheel (fl, fr, rl or rr), T_{drive_i} is the torque of the motor (which is known) and T_{wi} is the remaining torque, because of which the wheel will rotate.

Limitations

The denominators in the equations in Table 6.3 are proportional to the speed of the wheel (rotational or linear). Therefore, if the speed is close to zero, these expressions will provide a non valid result. A new simpler model is introduced in order to avoid this problem. In this model, the horizontal forces are calculated as shown in Table 6.4.

Table 6.4: Horizontal forces calculation for the low speed case.

Longitudinal Force	$F_{wL} = k_L \cdot (v_r - v_w \cos\alpha)$
Side Force	$F_{wS} = k_S \cdot v_w \sin\alpha$

Where $k_L = -1000N/(m/s)$ and $k_s = 0.7N/(m/s)$ are constants, which values have been calculated using a test-error process. This model is used only in the low speed case. Table 6.5 summarizes the use of one or each model, depending on the speed of the wheel, as well as the transition, smoothed to avoid discontinuities. In the table, F_{wL_B} (F_{wS_B}) and $F_{wL_{ls}}$ ($F_{wS_{ls}}$) are the longitudinal (side) forces calculated using the Burckhardt and the low-speed models, respectively. On the other hand, $v_{tl} = 0.1m/s$ and $v_{th} = 0.2m/s$ are the lower and higher threshold speeds respectively.

The validity of this solution is discussed in Section 6.4.8.

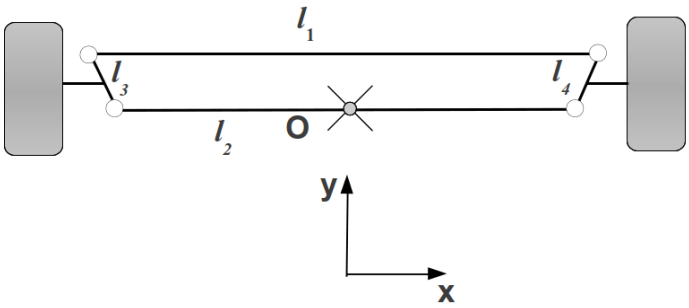

Figure 6.22: Steering system model.

6.4.7. Steering system

As explained in Section 6.3.2, the steering system is not imported from the CAD model. It is based on the rack and pinion mechanism of the vehicle (Fig. 6.10), but it was simplified into the four-bar linkage shown in Figure 6.22, where: $l_1 = 1.17m$, $l_2 = 1.01m$ and $l_3 = l_4 = 0.12m$.

It is assumed that the horizontal component (x axis) of the point 'O' is proportional to the angle of the steering wheel.

6.4.8. Model validation

In this section, the results of two simulations are compared with the data taken from two real test. This tests were performed in a dry, flat and horizontal concrete surface (Figure 6.23).

The inputs of the model are the torque set point and the steering wheel angle. The latter is taken from the value measured with the sensor of the vehicle (Sec. 6.2.3). The torque set point is given to the real car by the throttle and brake pedals. However, despite the positions of these pedals are logged, the lack of a model for the motor and brakes make these values useless at the moment. The torque set point is given by a PI controller that tracks the vehicle speed. The value of the speed given by the GPS device is corrected with the calculation done using the contrasted online tool GPSvisualizer [47], based on the GPS position data. Unfortunately, this will not avoid some errors due to the GPS precision. However, the speed measurement is accurate enough.

Table 6.5: Horizontal forces calculation depending on v_w.

	Longitudinal force	*Side force*
$\lvert v_w \rvert < v_{tl}$	$F_{wL} = F_{wL_{ls}}$	$F_{wS} = F_{wS_{ls}}$
$v_{tl} \geq \lvert v_w \rvert < v_{th} m/s$	$F_{wL} = F_{wL_{ls}} \frac{v_{th} - v_w}{v_{tl}} + F_{wL_B} \frac{v_w - v_{tl}}{v_{tl}}$	$F_{wS} = F_{wS_{ls}} \frac{v_{th} - v_w}{v_{tl}} + F_{wS_B} \frac{v_w - v_{tl}}{v_{tl}}$
$\lvert v_w \rvert \geq v_{th}$	$F_{wL} = F_{wL_B}$	$F_{wS} = F_{wS_B}$

Figure 6.23: Test track.

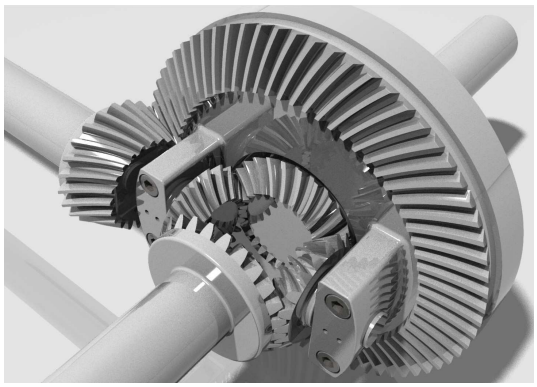

Figure 6.24: MEchanical differential.

Rear Wheel Drive (RWD) test

RWD test conditions

For the first test only the rear wheel motors were active. Both rear wheel motors applied the same torque. The front wheels rolled freely. This configuration is similar to the RWD ICEV case, where a mechanical component (differential) distributes the torque equally between the rear wheels. Figure 6.24 shows a mechanical differential.

Figures 6.25 and 6.26 show the steering wheel position and the speed set point and tracking.

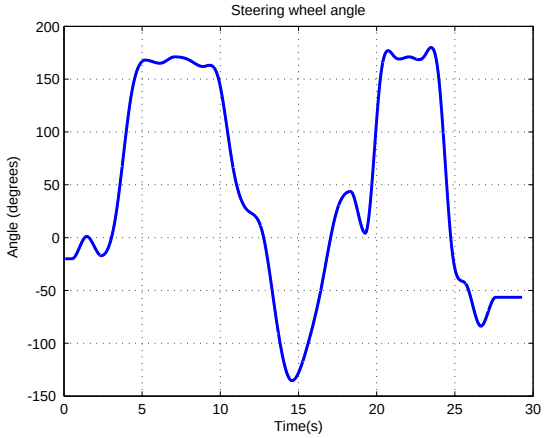

Figure 6.25: Steering wheel angle.

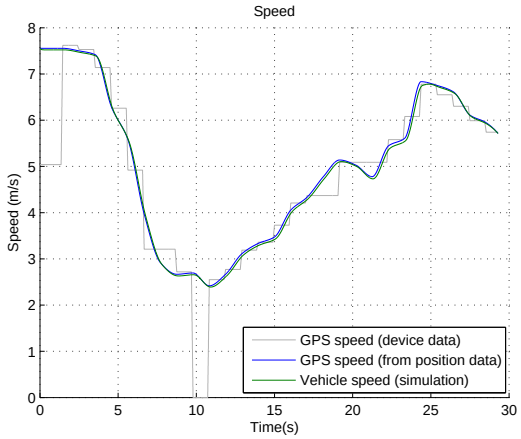

Figure 6.26: Speed.

RWD test simulation results

Figure 6.27 shows the longitudinal, side and resultant slips in the four wheels. The main difference between the front and the rear wheels is the longitudinal slip. While in the rear wheels it takes values quite similar to the side slip, in the front wheels both parameters vary in different orders of magnitude. As the front wheel motors do not make any torque, the only resistance to the movement is the inertia of the wheel. On the other hand, the torque applied by the rear motors makes the longitudinal slip increase, and so the longitudinal force, as shown in Figure 6.28, where the longitudinal and side forces of the wheels are represented.

The side slip takes its highest values when the vehicle is turning, due to the inertial forces. This is easy to check comparing Figure 6.27 with the steering wheel angle (Figure 6.25). The slip angle, defined in Section 6.4.6, is represented in Figure 6.29. As expected,

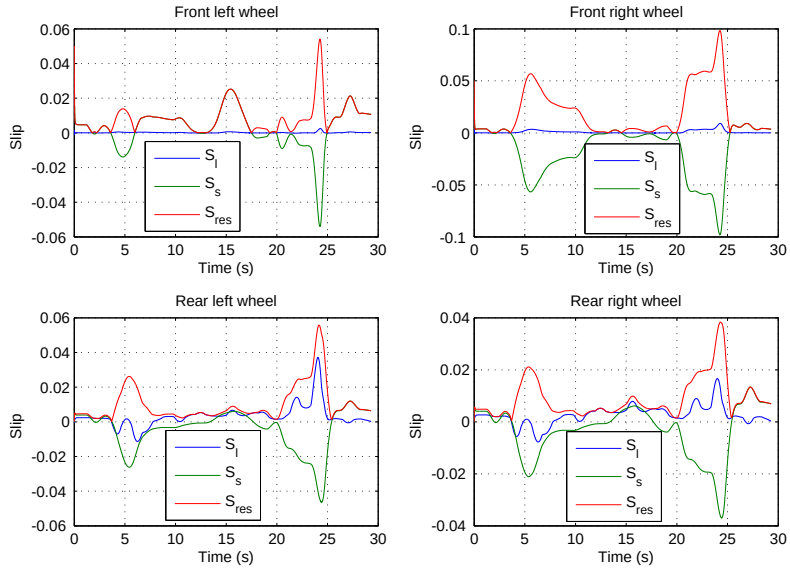

Figure 6.27: Slips in each wheel.

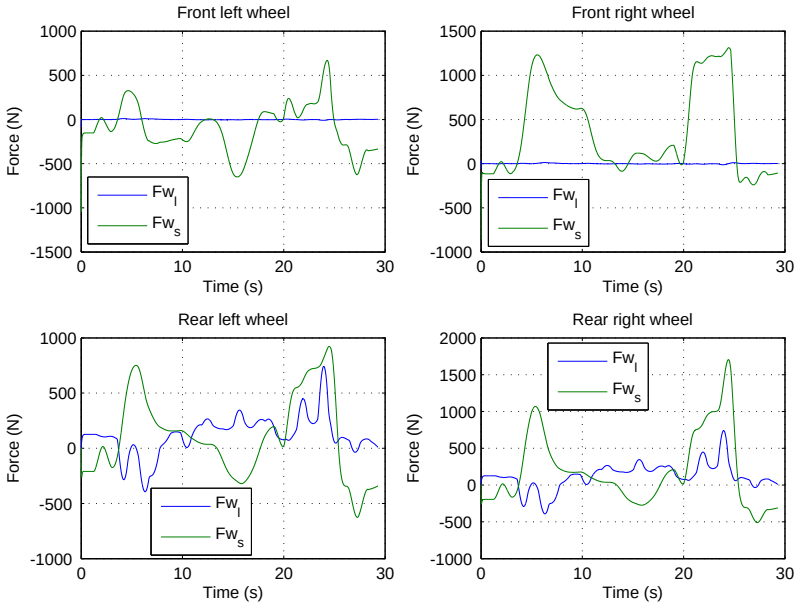

Figure 6.28: Forces in each wheel.

the value of this angle increases with the curvature of the trajectory and the speed of the car.

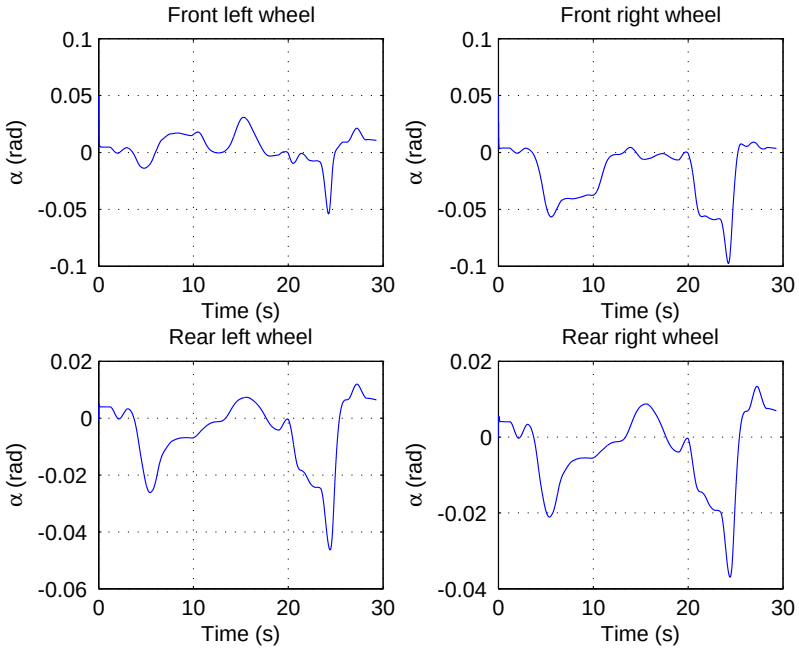

Figure 6.29: Slip angle in each wheel.

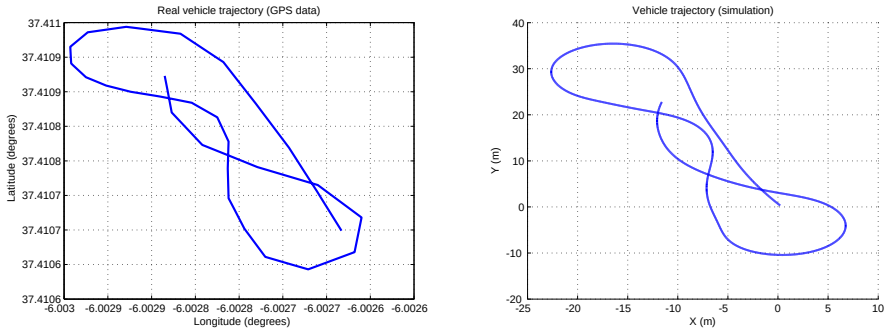

(a) Vehicle trajectory (GPS). (b) Vehicle trajectory (simulation)

Figure 6.30: Vehicle trajectory.

Finally, the trajectories of the real test and the simulation are compared in Figures 6.30
380 (a) and (b).

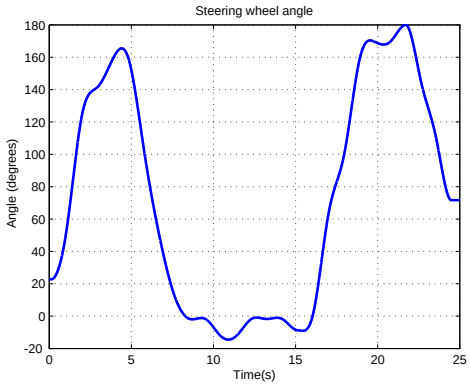

Figure 6.31: Steering wheel angle.

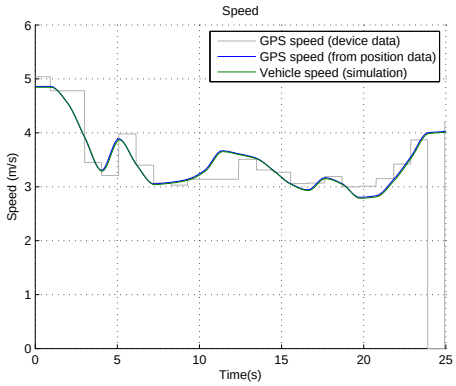

Figure 6.32: Speed.

Four wheel drive (4WD) test

4WD test conditions

A second test was performed, where the four wheels applied the same torque. The speed and the steering wheel angle are shown in figures 6.31 and 6.32.

4WD test simulation results

The slips are shown in Figure 6.33. In this case all the slips are of the same order, and the total drive is shared between the four wheels.

The trajectories of the real test and the simulation are shown in Figures 6.34 (a) and (b).

Discussion

The accuracy of the model cannot be quantified, due to the poor precision of the GPS device, that affects not only to the trajectory graph, but to the speed measurement, as explained

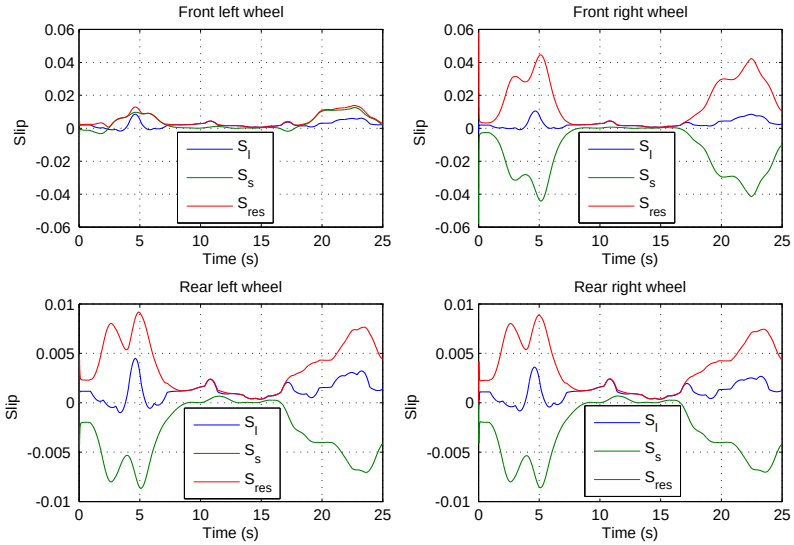

Figure 6.33: Slips in each wheel.

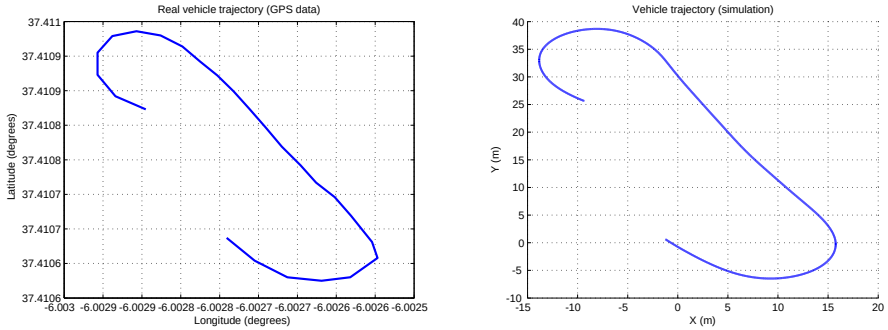

(a) Vehicle trajectory (GPS). (b) Vehicle trajectory (simulation)

Figure 6.34: Vehicle trajectory.

at the beginning of Section 6.4.8. The conversion from geographical to UTM coordinates would involve a second source of error.

The tests were performed at low speed due to the small dimensions of the track. With higher speeds, the slip would be more significant.

However, the shape of the trajectories (Figures 6.30 and 6.34) demonstrates that both the real vehicle and the model have a very similar behaviour in both RWD and 4WD tests. Therefore, it is proved that the model performs a realistic trajectory, so it valid to test any kind of traction controller before its implementation in the car, which is the aim of designing this model.

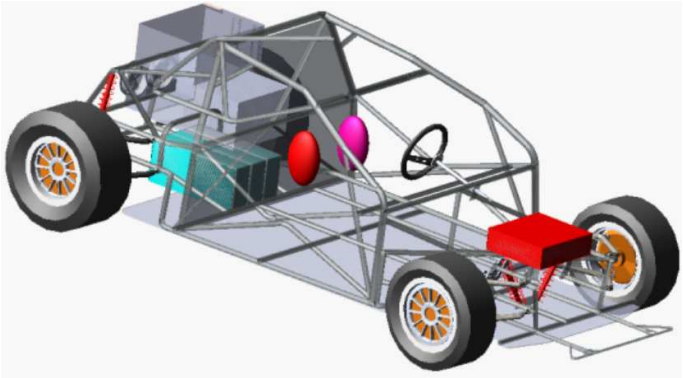

Figure 6.35: ADAMS model.

6.5. ADAMS Model

6.5.1. Description

A numerical model of the dynamic behaviour of the vehicle has been developed and implemented in ADAMS software by Mántaras and Luque [73]. As explained in section 6.3, the ADAMS model (Fig. 6.35) is based on a CAD design. This section brings a brief explanation of the model.

The kinematic configuration of the vehicle is composed of 40 bodies, 15 revolute joints, 16 spherical joints, 3 translation joints, 4 homokinetic joints and 13 fixed joints.

Some masses have been added to the model in order to increase its precision and to take into account some elements of the vehicle that have not been included in the CAD model.

The final model has 14 degrees of freedom. The dynamic characterization is determined by the modelling of several elements, like the helical springs, the telescopic shock-absorbers and the pneumatic wheels. For the tyres Pacejka's Magic Formula [92] has been used. The identifying parameters have been obtained from the curves of the manufacturer (Avon [10]).

The suspension wishbones are assumed to be rigid, and linked to the tubular chassis with ideal spheric joints (no friction nor clearance). It is also assumed that the springs and absorbers are linear in their operational zone.

Several inputs have been included for the simulation of the model. The kinematics are essentially controlled by the movement of the steering system. The control is imposed by the movement of the steering wheel.

The dynamic control of the vehicle is regulated by torque in each wheel. As a first approach to the model, an equitable distribution of the torque is used (ie. same torque for each wheel). For imposing the torque, a PID controller is used, in which the speed and linear acceleration values are set.

6.5.2. Testing and experimental validation

For the validation of the ADAMS model, an experimental program based on static and dynamic tests in the real vehicle is proposed [76]. For this program, two kinds of tests will

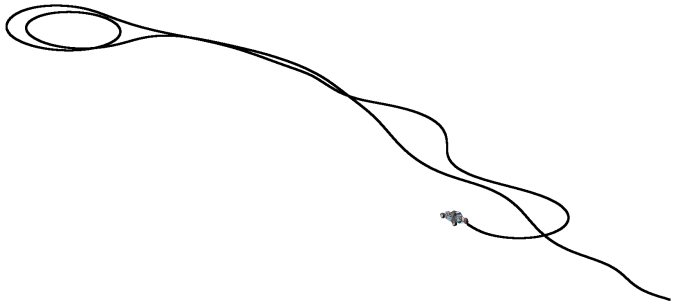

Figure 6.36: Mixed trajectory.

be performed:

1. Static: Several loads and controlled displacements were applied for obtaining information necessary to set some parameters of the model:
   a Weight distribution in each wheel and mass centre.
   b Preload of the suspension helicoidal springs.
   c Gearing of the steering system.
   d Equivalent wheel suspension stiffness.
2. Dynamic: Several dynamic tests were performed in order to collect the data necessary to set and validate the model.
   a. Acceleration in a straight line and in curves.
   b. Braking in a straight line and in curves.
   c. Slalom.
   d. Circular curves at constant/increasing speed.
   e. Mixed trajectories.

For instance, the simulation of a mixed slalom, circular curves, slalom, and braking curve is shown in Figure 6.36.

After the final adjustment of the model, it is seen that the most representative variables of the vehicle movement (trajectory, speed and acceleration) are reproduced correctly, as well as the dynamic response of some significant elements, as the steering, suspension and the tyres.

6.6. Torque distribution controllers

Modern cars have several active safety systems that actuate over the torque of the wheels, like Anti-lock Braking System, Traction-Control System or Electronic Stability Program. However, these systems actuate only in extreme cases (lost of grip in one or more wheels) and usually to reduce the torque, by braking and/or stopping the fuel supply

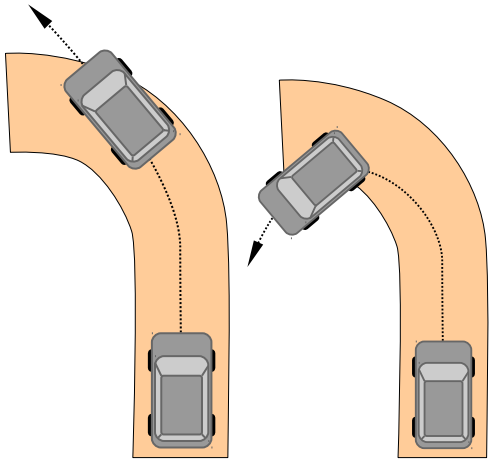

(a) Understeering (b) Oversteering

to the engine (reducing the power in case of EVs). The rest of the time, the torque of the engine/motor is equally distributed between the tractive wheels.

As explained in Section 6.1, the use of one motor per wheel opens a wide range of possibilities of torque control. An easier and safer driving can be achieved with a better torque distribution, increasing or reducing the torque in each wheel depending on the circumstances.

In this section, two distribution controllers for the vehicle are presented and compared. The first one emulates a mechanical differential system, in which the same torque is applied to the four wheels. This is a simple but effective control, used by almost all the Four Wheel Drive (4WD) vehicles in the world. It will be considered the baseline controller. The second controller is based on a PI that controls the yaw rate of the vehicle. These controllers have been tested in the Simmechanics model.

6.6.1. Understeering and oversteering

Definition

In [84], the National Highway Traffic Safety Administration (NHTSA) defines oversteering and understeering as ”typically cases of loss-of-control where vehicles move in a direction different from the drivers intended direction. Oversteering is a situation where a vehicle turns more than drivers input because the rear end of the vehicle is spinning out or sliding out. Understeering is a situation where a vehicle turns less than the drivers input and departs from its intended course because the front wheels do not have sufficient traction.” Figures 6.37(a) and 6.37(b) show graphically both cases.

Obviously these situations are both undesirable. The avoidance or diminution of the effects of understeering and oversteering will be the aim of the torque distribution controllers.

Understeer gradient

The understeer gradient is a parameter that measures the understeering and oversteering effects in a vehicle. It is defined by the Society of Automotive Engineers (SAE) [99] as "the quantity obtained by subtracting the Ackermann steer angle gradient from the ratio of the steering wheel angle gradient to the overall steering ratio". Namely [46],

$$\delta = \delta_a + K \cdot a_y \tag{6.12}$$

Where K is the understeer gradient, δ is the steer angle, and δ_a is the Ackermann steer angle.

The steer angle is the angle between the longitudinal axis of the vehicle and the direction of the front wheel of the bicycle model. In this simplified model the car is represented by a bicycle that has the same wheelbase as the car. Its steer angle is defined by the steering wheel angle of the vehicle, so that the bicycle radius of turn is the same as the one of the car. Figure 6.37 show the bicycle model, where the steering angle (δ), the wheelbase (L) and the radius of turn (R) are represented.

The Ackermann steer angle is "the angle whose tangent is the wheelbase of the vehicle divided by the radius of turn" [99] (Equation 6.13).

$$\delta_a = atan\left(\frac{L}{R}\right) \tag{6.13}$$

The simplest way to relate the steering wheel angle to the steer angle is performing some constant radius tests at low speed. In these tests the lateral acceleration is so low that the effect over the steer angle is negligible, so the steer angle can be approximated to the Ackermann steer angle (Equation 6.12). The results of the tests are shown in Figure 6.38.

Going back to Equation 6.12, the understeer gradient indicates the grade of understeering/oversteering effect over the vehicle. If the gradient is positive it means that the steering

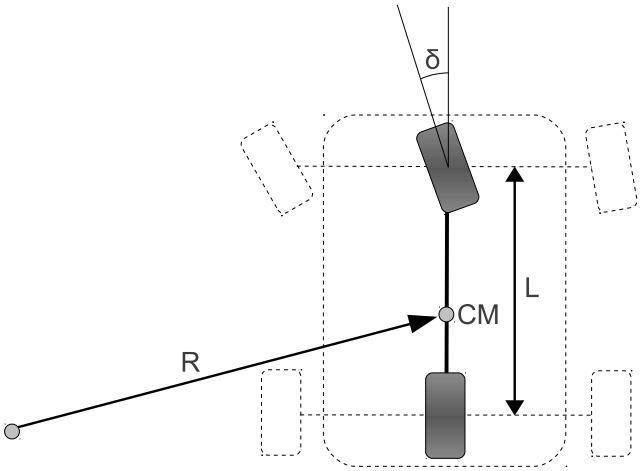

Figure 6.37: Bicycle model.

angle is higher than the Ackermann steering angle. Therefore the real radius of turn is higher than the theoretical, so it is an understeering case. On the opposite, a negative gradient means an oversteering situation. Finally, if the gradient is zero the situation is named 'neutral steering', which is the optimal case.

Calculation of the understeer gradient

There are several methods to calculate the understeer gradient. In [46], Gillespie describes three of them: constant speed, constant steer angle and constant radius methods. The most simple, and probably the most used one is the latter. In the constant radius method the vehicle performs several tests tracking a curve with a constant radius in steady state. The tests are at different speeds, so the lateral acceleration varies between one and other.

Differentiating Equation 6.12 respect the lateral acceleration:

$$\frac{\partial \delta}{\partial a_y} = \frac{\partial \delta_a}{\partial a_y} + K \cdot \frac{\partial a_y}{\partial a_y} \tag{6.14}$$

Substituting Equation 6.13 into 6.14:

$$\frac{\partial \delta_a}{\partial a_y} = \frac{\partial \left(atan\left(\frac{L}{R}\right)\right)}{\partial a_y} = 0 \tag{6.15}$$

Therefore,

$$\frac{\partial \delta}{\partial a_y} = K \tag{6.16}$$

the understeer gradient is the slope of the steer angle curve. Figure 6.39 represents the steer angle curve and the understeer gradient for different situations.

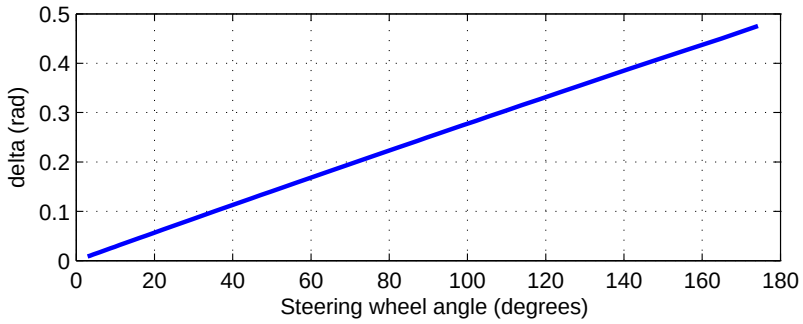

Figure 6.38: Steering angle vs steering wheel angle.

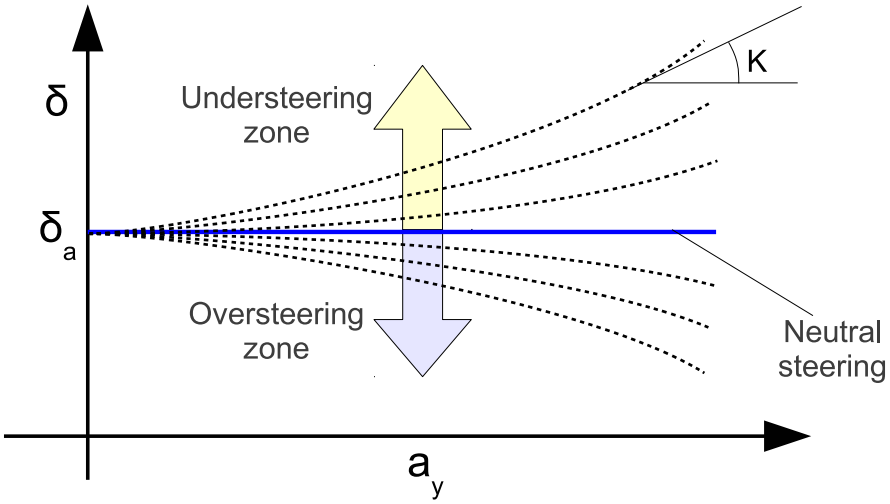

Figure 6.39: Constant radius method curves.

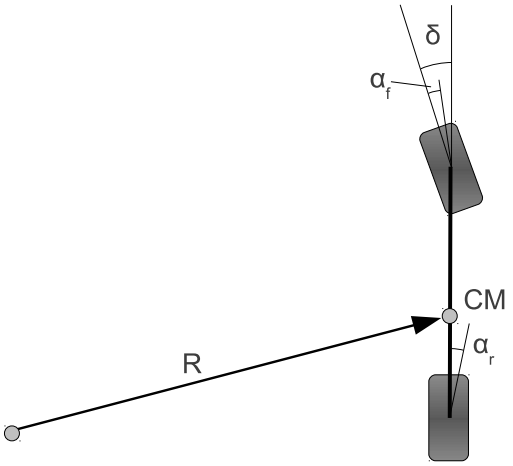

Figure 6.40: Bicycle model.

6.6.2. Influence of the torque distribution over the performance of the vehicle

Front and rear torque distribution

515 Figure 6.40 shows the bicycle model of the vehicle in a left turn. In the picture, α_f and α_r are the front and the rear slip angles respectively. It is easy to see that a bigger slip angle in the front wheel implies a bigger radius of turn (understeering), and on the contrary a bigger slip angle in the rear wheel implies a smaller radius of turn (oversteering).

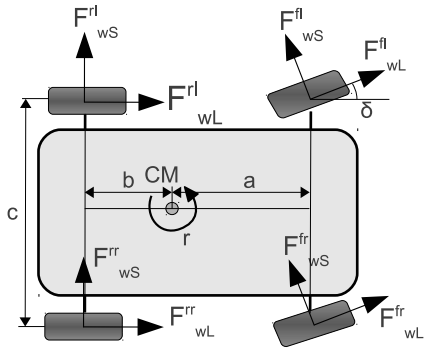

Figure 6.41: Forces diagram.

As depicted in Section 6.4.7, a bigger torque increases the slip angle. Therefore, understeering (oversteering) can be diminished by decreasing the torque of the front (rear) wheels, incrementing the torque in the other axis to fulfil the requirements of the driver.

Left and right torque distribution

Figure 6.41 shows the horizontal forces in the vehicle when turning left. In this case it is assumed that both front wheels have the same steering angle ($\delta_{fl} = \delta_{fr} = \delta$).

The vehicle motion equation in the axis z is:

$$\begin{aligned} I_{zz}\dot{r} = &\left[a\left(F_{wS}^{fl}+F_{wS}^{fr}\right)cos\delta - b\left(F_{wS}^{rl}+F_{wS}^{rr}\right)+\frac{c}{2}\left(F_{wS}^{fl}-F_{wS}^{fr}\right)sin\delta\right]+ \\ &\left[a\left(F_{wL}^{fl}+F_{wL}^{fr}\right)sin\delta+\frac{c}{2}\left(F_{wL}^{fr}-F_{wL}^{fl}\right)cos\delta+\frac{c}{2}\left(F_{wL}^{rr}-F_{wL}^{rl}\right)\right] \end{aligned} \tag{6.17}$$

where r is the yaw rate, I_{zz} is the inertia of the vehicle in the vertical axis and F_{wx}^{ij} are the friction road-tyre forces (see Section 6.4.5).

The second member of Equation 6.17 is divided in two terms. In the first one, the torque is generated by the side forces, and in the second one it is generated by the longitudinal forces. The side forces depend on the lateral acceleration, while the longitudinal forces depend on the torque applied to the wheel. Therefore, the torque distribution will only affect directly to the second term.

Grouping the first term into a new variable

$$T_{F_S} = a\left(F_{wS}^{fl}+F_{wS}^{fr}\right)cos\delta - b\left(F_{wS}^{rl}+F_{wS}^{rr}\right)+\frac{c}{2}\left(F_{wS}^{fl}-F_{wS}^{fr}\right)sin\delta \tag{6.18}$$

and rearranging the variables in the second term, Equation 6.17 becomes:

$$I_{zz}\dot{r} = T_{F_S} + \left[F_{wL}^{fl}\left(a\sin\delta-\frac{c}{2}\cos\delta\right)-\frac{c}{2}F_{wL}^{rl}\right]+\left[F_{wL}^{fr}\left(a\sin\delta+\frac{c}{2}\cos\delta\right)+\frac{c}{2}F_{wL}^{rr}\right] \tag{6.19}$$

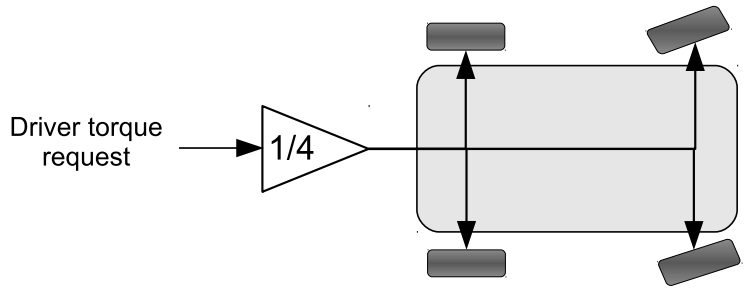

Figure 6.42: Equal torque distribution.

In this equation, the second (third) term of the second member represents the torque generated by the longitudinal forces in the left (right) wheels.

Assuming the torque in the wheels is positive (what implies the longitudinal forces are also positive). Equation 6.19 shows that the longitudinal forces in the outer wheels (in this case, the right wheels) make a positive torque over the vertical axis of the vehicle, while the forces in the inner wheels is negative except for high values of δ.

Consequently, if the torque distribution decrements the torque in the inner wheels, incrementing it on in the outer ones, the yaw moment will increase, and vice-versa.

6.6.3. Equal torque distribution controller

The first controller emulates a mechanical differential for a one motor 4WD vehicle, in which the torque is distributed equally between the four wheels (Figure 6.42). This is considered as the baseline to be compared with the controller depicted in next section.

6.6.4. PI yaw rate controller

The system has three Degree of Freedom (DoF): the front-rear, the front left-front right and the rear left-rear right distributions, since the sum of all the torques must equal the torque demanded by the driver. However, this controller will apply the same ratio for the three DoFs. This ratio is generated by a Single Input Single Output (SISO) PI that controls the yaw rate of the vehicle. According to what was exposed in Section 6.6.2, if the yaw rate error is negative, the controller should increase the torque in the back and outer wheels, and vice-versa, as shown in Equations 6.20 to 6.23 and Figure 6.43.

$$ratio_{fi} = (1-u)(1-u) \tag{6.20}$$

$$ratio_{fo} = (1-u)u \tag{6.21}$$

$$ratio_{ri} = u(1-u) \tag{6.22}$$

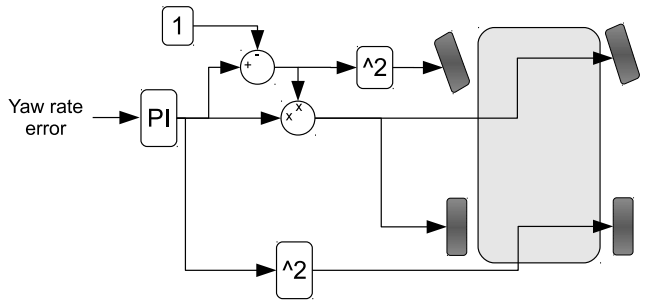

Figure 6.43: Yaw rate controller.

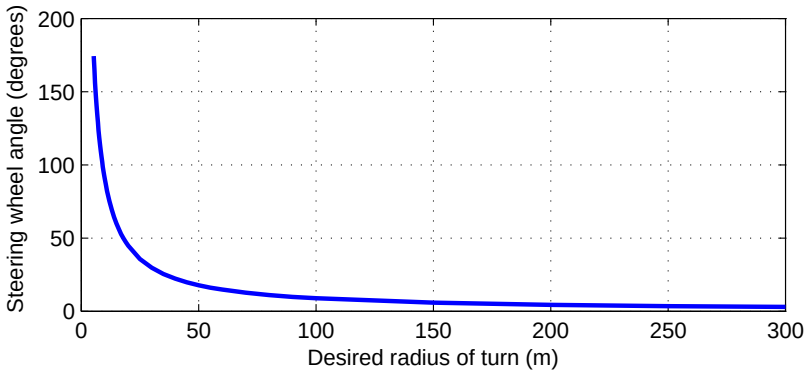

Figure 6.44: Steering wheel angle vs desired radius of turn.

$$ratio_{ro} = u \cdot u \tag{6.23}$$

where u (between 0 and 1) is the output of the controller and fi, fo, ri, ro mean front inner, front outer, rear inner and rear outer respectively.

Yaw rate reference

The desired yaw rate can be found by equation 6.24

$$r_d = \frac{v}{R_d} \tag{6.24}$$

where v is the longitudinal speed of the car and R_d is the desired radius of turn, which is the radius of turn in the neutral steering case. The correlation between this radius and the steering wheel angle was found by the low speed tests described in Section 6.6.1, and is shown in Figure 6.44.

Consequently, the desired yaw rate is found interpolating a table whose breakpoints are the speed and the angle of the steering wheel. This table is represented as a 3D plot in Figure 6.45.

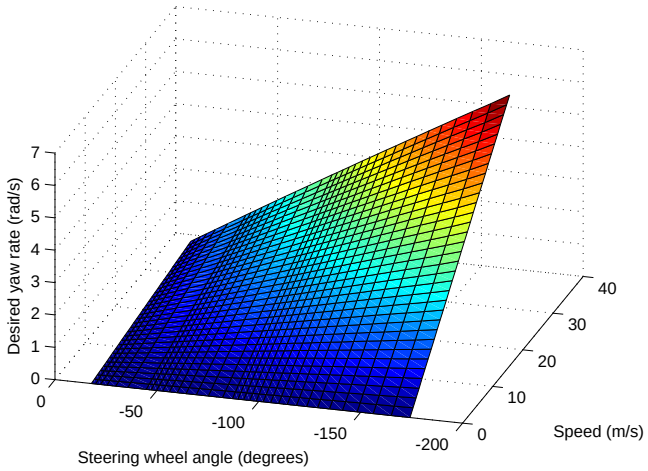

Figure 6.45: Desired yaw rate against speed and steering wheel angle.

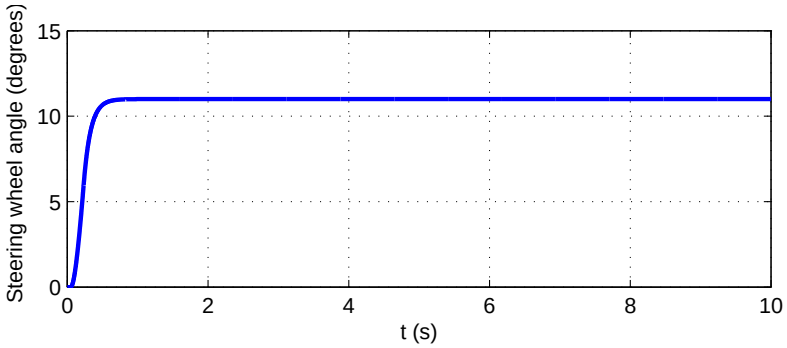

Figure 6.46: Steering wheel angle for the dynamic test.

6.6.5. Description of the tests

To evaluate the goodness of the two controllers, three tests were performed. The first one is the 'constant radius method' to calculate the understeer gradient. This method was described in Section 6.6.1. This method was applied to the vehicle with both controllers for two radius of turn: 80 and 200 meters.

In the second test, the vehicle starts at constant speed (70 km/h) and with the steering wheel in neutral position (0 degrees). This angle starts rising in a 60 degrees/s ramp (smoothed in the edges) until it reaches 11.08 degrees, which is the Ackermann steering wheel angle for a radius of turn of 80 m (Figure 6.46). The aim of this test is to evaluate the dynamic response of the vehicle.

For the last scenario, the vehicle starts at the end of the previous test (steady-state, speed=70 km/h, steering wheel angle=11.08 degrees), and the ground changes from dry asphalt to wet asphalt. This is simulated changing the c_i parameters of the Burckhardt

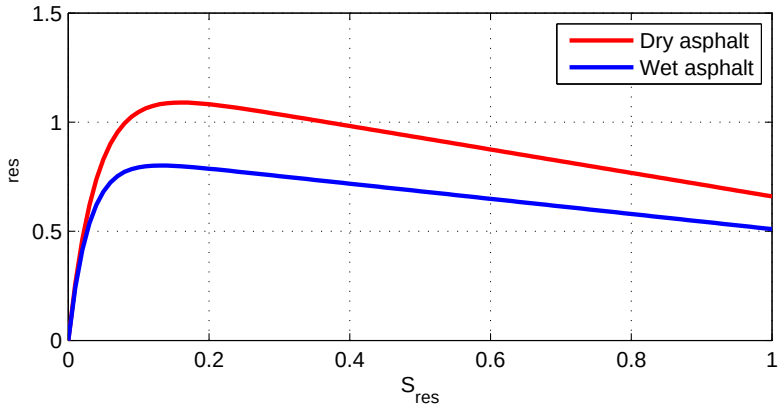

Figure 6.47: Resultant friction coefficient.

model (Section 6.4.7). The values of these parameters are shown in Table 6.6, while Figure 6.47 shows the resultant friction coefficient in both cases.

Table 6.6: Burckhardt model parameters.

Asphalt condition	c_1	c_2	c_3
Dry	1.1973	25.168	0.5373
Wet	0.857	33.822	0.347

6.6.6. Results

Equal torque distribution

The graphics for the constant radius method are shown in Figures 6.48(a) and 6.48(b)

In both cases, the steering angle increments with the lateral acceleration. This implies a positive understeer gradient, what means that the vehicle has an understeering tendency with the equal torque distribution controller. Table 6.7 shows the numeric values of the gradients for the final part of each graph.

Table 6.7: Understeer gradient for the equal torque distribution.

Radius (m)	$a_y\ (m/s^2)$	Gradient $\left(\frac{rad}{m/s^2}\right)$
80	5.385	$8.009 \cdot 10^{-4}$
200	2.359	$3.230 \cdot 10^{-4}$

For the second test, the resulting yaw rate is shown in Figure 6.49, where the reference line is the yaw rate the vehicle would have in neutral steering. In the graph, a certain steady

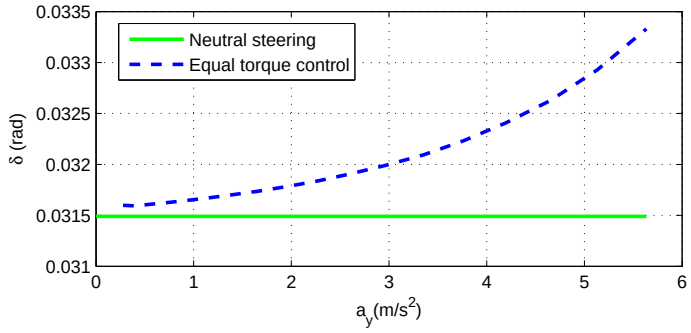

(a) $R = 80m$

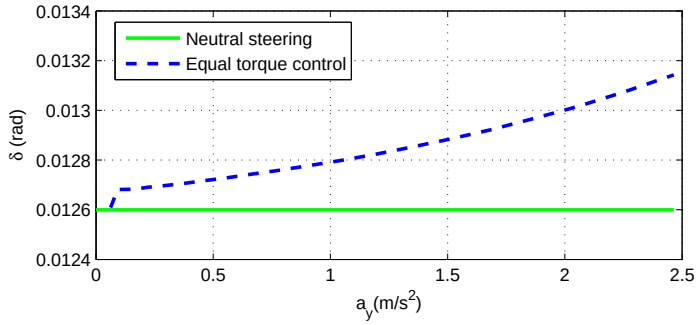

(b) $R = 200m$

Figure 6.48: Constant radius method graphics (equal torque distribution).

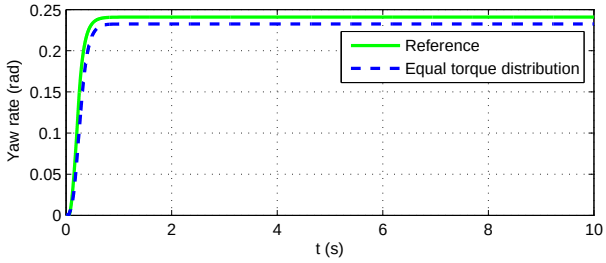

Figure 6.49: Dynamic test for the equal torque distribution controller.

590 state error is outlined (3.5%). Thus, the yaw rate of the vehicle in steady state is always lower than the reference, what confirms the vehicle is in an understeering situation.

Finally, the result of the third test is shown in Figure 6.50. The yaw yaw rate error increments (3.5% to 4.8%), as expected.

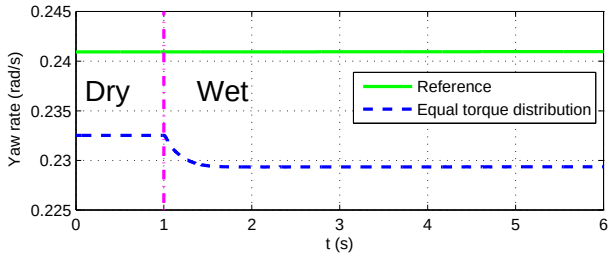

Figure 6.50: Disturbance test for the equal torque distribution controller.

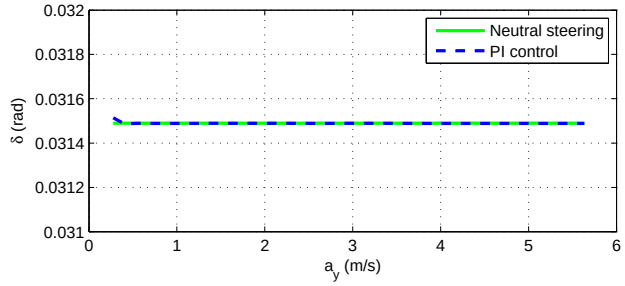

(a) $R = 80m$

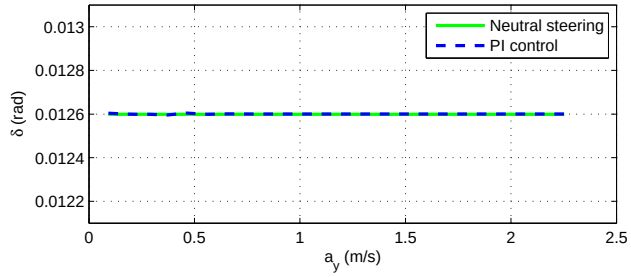

(b) $R = 200m$

Figure 6.51: Constant radius method graphics (PI yaw rate controller).

PI yaw rate controller

The graphs of the constant radius method for the PI yaw rate controller are represented in Figures 6.51(a) and 6.51(b).

In this case the steering angle is almost constant respect the lateral acceleration, and very close to the Ackermann steering angle. It implies that the car has a neutral steering behaviour. Table 6.8 shows the numeric values of the gradient for the end of the graphs.

Table 6.9 shows the values of the PI output for different speeds, and a constant radius of turn of $80m$. In all the cases, the values are higher than 0.5, what means that the torque is higher in the outer and rear wheels. This is coherent with the results of the previous controller, considering its understeering tendency. The PI output increments with the speed.

Table 6.8: Understeer gradient for the PI yaw rate controller.

Radius (m)	a_y (m/s^2)	Gradient $\left(\frac{rad}{m/s^2}\right)$
80	5.385	$2.133 \cdot 10^{-7}$
200	2.359	$2.683 \cdot 10^{-7}$

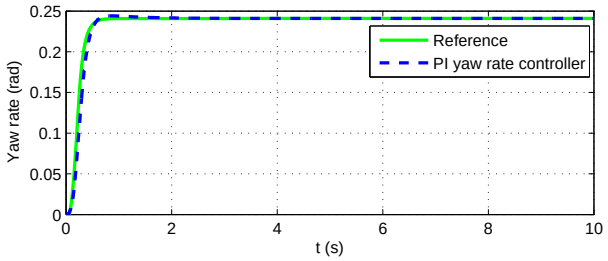

Figure 6.52: Dynamic test for the PI yaw rate controller.

This is also coherent with the previous results, due to increase of the understeer gradient with the lateral acceleration (Figure 6.7).

Table 6.9: PI output.

Radius (m)	v (km/h)	PI output
80	30	0.5394
80	50	0.5695
80	70	0.6229

Performing the second test, the vehicle tracks the yaw rate reference, as shown in Figure 6.52, where the overoscillation is insignificant. Figure 6.53 shows the PI output for this test. Finally, the results of the third test are shown in Figure 6.54. In this case, after a very small peak (0.3%), the vehicle is able to track the reference again. Therefore, the driver would hardly notice the variation in the condition on the road, and does not need to actuate at all. The controller output for this case is shown in Figure 6.55.

When the vehicle enters the wet zone, the friction coefficients of the wheels get lower. This increases the slip in all the wheels, specially in those where the torque is higher, in this case the rear and outer wheels. A side slip increase in the rear wheels causes an increment in the yaw rate, what makes the controller smooth its output.

6.6.7. Discussion

Comparing the results of the understeer gradients of the two controllers in Figures 6.56 and 6.57, it is easy to see how the PI yaw rate controller improves the behaviour of the vehicle. Comparing Tables 6.7 and 6.8, there is a difference of three orders of magnitude in

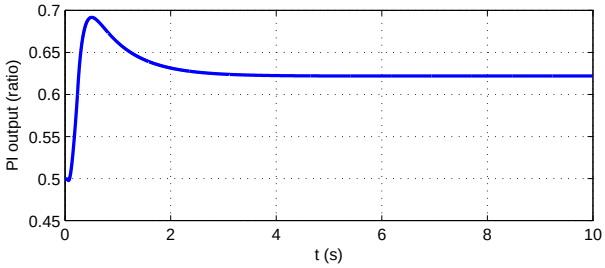

Figure 6.53: PI signal of control.

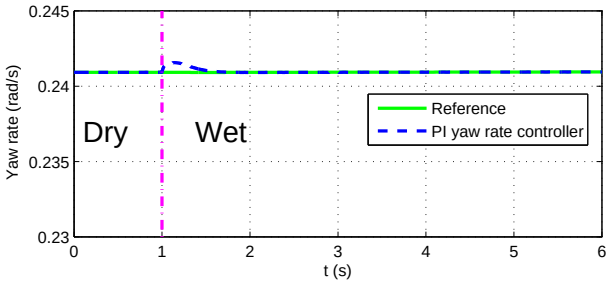

Figure 6.54: Disturbance test for the PI yaw rate controller.

the understeer gradients. The difference in the sign of the gradient is not significant, due to its negligible value.

For the two last tests, the comparison between both controllers is summarized in Figure 6.58, where the vehicle enters the wet asphalt in the second 10.

The figure shows the better behaviour when the car where the PI yaw rate controller is acting. This difference becomes more evident when plotting the trajectories of the vehicle using both controllers (Figure 6.59).

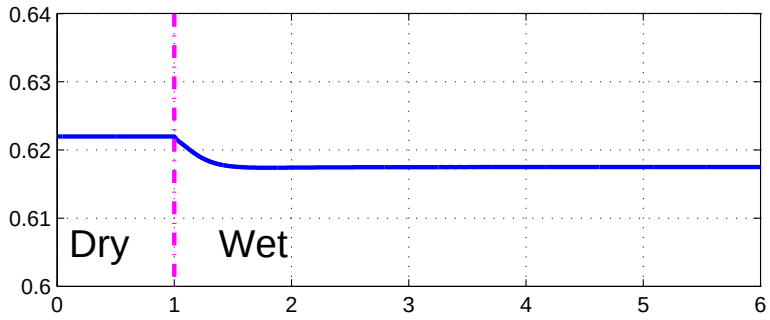

Figure 6.55: PI output.

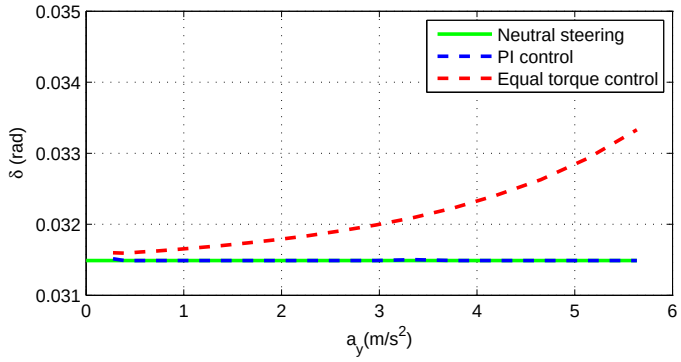

Figure 6.56: Constant radius method graphics $(R = 80m)$.

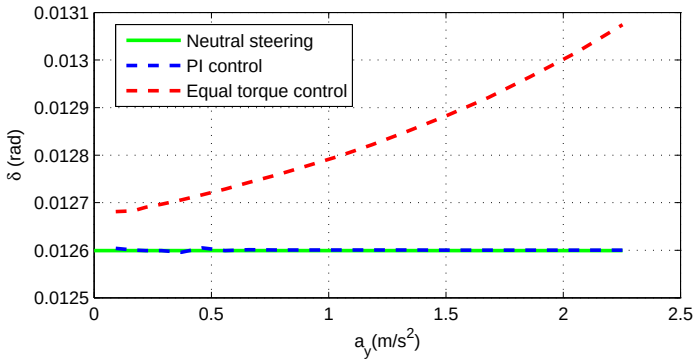

Figure 6.57: Constant radius method graphics $(R = 200m)$.

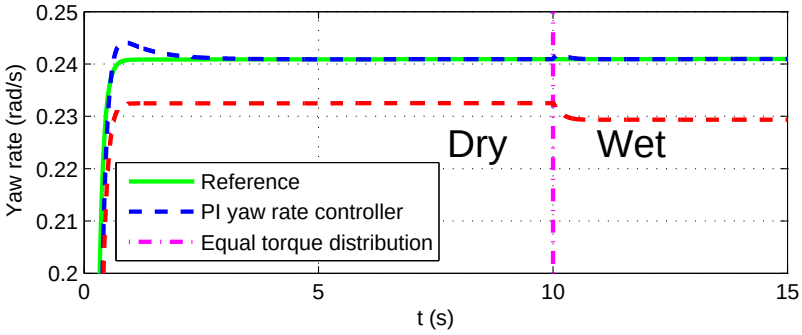

Figure 6.58: Comparison between both controllers in tests 2 and 3.

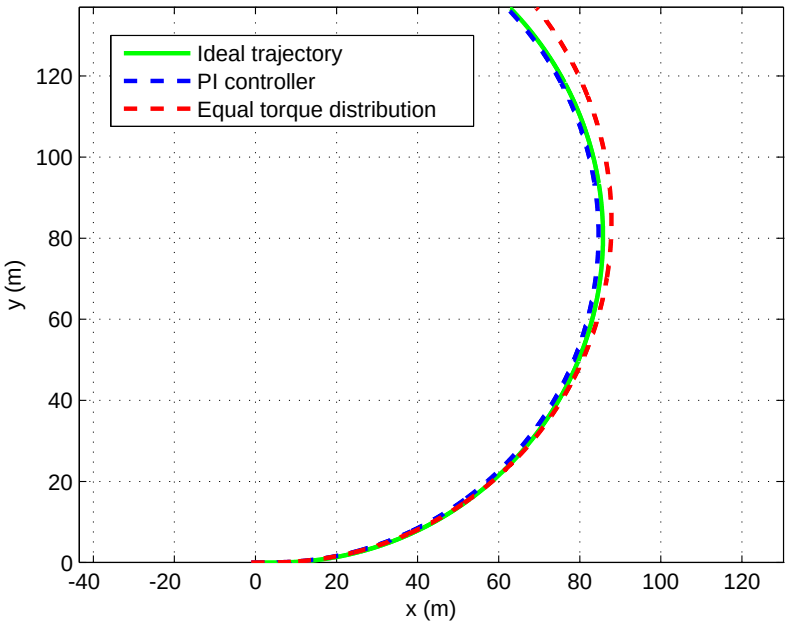

Figure 6.59: Trajectories of the vehicle.

6.7. Conclusions

In this chapter, a 3D CAD model of the FOX four wheel-motor electric vehicle was presented. This model has two variants, that differ in the steering system. The most realistic variant was used to create a numeric dynamic model of the vehicle using the *ADAMS* software. The simplified model was ported into the *Simulink Simmechanics* toolbox to create a dynamic model. This model was validated with real data.

Finally, two torque distribution controllers were developed for the vehicle and tested on *Simmechanics* model. The first one (considered the baseline controller) distributes the torque equally in the four wheels, while the second one controls the rate of the yaw angle with a PI controller. The simulations demonstrate the better performance of the PI-based torque distribution over the baseline controller.

Chapter 7

Conclusions and future research

7.1. Conclusions

- A commercial BEV was hybridized by the addition of a hydrogen storage system and a fuel cell as a second energy source. The power converter (also introduced) and the fuel cell are controlled by a central power management system, depending on the SOC of the batteries. This system was tested, and the experimental results demonstrated the feasibility of the fuel cell as an energy source for automotive applications.

- Another variant for the same car was also presented, in which the fuel cell was substituted by two lower power FC stacks. The new controller is divided in three levels. The highest level consists on a global power management system, that includes the power converter and the batteries. The middle level controller determines the power supplied by each of the stacks, and finally the low level controls both FCs. These controllers were successfully tested in real performance. Despite the use of two FCs instead of one implies the introduction of a new device, both FCs are not only smaller, but simpler than the one used in the first variant. As a consequence, the coolant circuit has been removed and the FCs are controlled by the ECU of the vehicle, what makes it easier to coordinate with the power management, specially in case of errors.

- The power management controller of a second FCHV prototype was presented. This vehicle was made in collaboration with several companies and public institutions. The car consists on a electric motor driven by a set of batteries and a fuel cell. A model of the power supply system of this vehicle was made. A MPC strategy was implemented for the power management system in the model. Besides, the use of UC as a substitute of the batteries was also studied, as well as the use of both storage devices. The MPC was able to fulfil the power requirements of the system, respecting the constraints and minimizing the fuel consumption. Despite it requires a high computational cost, the simulations demonstrate that it is fast enough to be implemented in a real ECU. Regarding the use of batteries or UCs as storage devices, the results of the three configurations were almost equivalent, so it is recommended to use only one source in order to simplify the system.

- A model of the combined series/parallel ICE PHEV Chevrolet Volt was used to design a power manager for a benchmark special session of the ECOSM 2012. The controller was divided in two levels. The high level estimated the energy necessary to complete the driving cycle and, considering the remaining energy in the batteries, requests power to the ICE in the most efficiency manner. On the other hand, the low level is composed on several controllers that manage the power devices minimizing the wasted power.

  The system was simulated in different standard and real driving cycles (urban, mountain, highway), as well as in acceleration and braking tests, demonstrating a good performance and fuel efficiency. Twenty groups started the benchmark competition, and this proposal classified fourth.

- A thermal model of the cabin of a vehicle is included in this thesis. This model calculated the heat transfer in the air of the cabin of the vehicle, with the aim of being included in a complete power system model of a vehicle, and analyse the effect of the HVAC in a car in terms of performance and consumption.

  This model was validated with real data, taken from a temperature sensor network installed in a vehicle. For this validation, several tests were performed under different conditions: stopped and unoccupied while outdoors, stopped and unoccupied while indoors, and running with one person inside the vehicle. Consequently, it is feasible to develop a model to be used for the design of controllers for the integration of the HVAC in the power management of a HV.

- The HVAC of a vehicle was modelled to be used with the thermal model of the cabin presented in Chapter 4. The model calculates the power consumption of the compressor, considering the heat transfer in the cabin, the specifications of the compressor, and temperature and humidity of the external and internal air.

- The HVAC and the thermal models were included in the power system models of two hybrid cars: a FCHV and a ICE PHEV. Several tests under different conditions of speed, weather (temperature, humidity and solar irradiation) and number of occupants were run, concluding that:

  - In any case the use of the HVAC has affected the performance significantly.
  - This increment is not negligible (3-10% in most cases), specially for the PHEV in city cycles, that can reach up to a 35%, due to the lower consumption in the urban scenario.

- A four in-wheel independent drive vehicle was presented. A 3D CAD model was made for this vehicle, with two variants, that differed in the steering system. These models were ported to *Matlab Simulink Simmechanics* and *ADAMS/ADAMS Car*, generating both numeric models of the vehicle dynamics. Both models were validated with real data.

- Two torque distribution controllers were designed. The aim of these controllers is to improve the performance of the car by reducing the understeering and oversteering effects. The controllers were implemented and tested in *Matlab Simulink Simmechanics*.

In summary, this thesis has addressed three important problems related to the new challenges associated to hybridization: management of the power sources, integration of HVAC in power management and dynamics control. Thus, the author was in involved in the design and set up of the three FCHVs mentioned in this thesis. It includes election of components, software design, modelling, control (power management and dynamics) and physical integration.

Regarding modelling, three kinds of models have been implemented in this thesis, involving HVs: power system, mechanical and thermal. The latter two were also validated with real data.

Finally, two kind of controllers were designed for the mentioned systems: car performance and power management controllers, where different control strategies were used (heuristic, linear, MPC...).

7.2. Future research

- The implementation of the MPC controller for the power management system of a FCHV in a real vehicle, and in particular in the platform FOX, described in Chapter 6. This vehicle carries the three different energy storage systems studied in Chapter 2 (hydrogen, batteries and UC), allowing any combination of these sources.

- Regarding the power management controller of the PHEV, it is based on the estimation of the energy that the vehicle needs to complete the cycle. This estimation, and so the controller, could be improved obtaining more data from the GPS unit. Thus, with the current technology, the device could also provide:

  - Average speed by stages. With this simple change, the controller could have a better vision of the power consumption during the cycle, and consequently it could distribute the energy of the batteries in a more efficiency manner, specially in combined urban/road, urban/highway cycles.
  - With a periodic refresh of the remaining distance the energy estimation would be more accurate, improving the power management.
  - The effect of the slope is not considered in the controller, due to the lack of data about this parameter. An average value of this parameter, also by stages, would increase the accuracy of the energy estimation, specially in mountain roads.

  A more advanced system with mobile phone technology could also improve the controller, by providing real time information of traffic, road conditions (water/snow), roads under construction, etc.

- Regarding the HVAC, the own system should be validated with real data.

- To predict the power consumption of the HVAC in the PHEV, the controller could use the values of the temperature and humidity of the external air, that most of the modern cars actually measure. Besides, the data of solar irradiation would also help to do this prediction.

- The compressor of the HVAC is driven by its own electric motor. In the case of the PHEV that motor could be the generator or the ICE. This would change completely the power management system and possibly improve the efficiency.
- In the case of the four in-wheel independent drive car, the implementation of the torque distribution controller in the real vehicle is the next step. The controller can be improved using a two or three-output Multiple Input Multiple Output (MIMO) controller that considers the free DoFs of the system. Thus, the controller would also consider other parameters (typically, the lateral acceleration) what would ensure the correct behaviour of the vehicle.
- The torque distribution control would be complete developing an ESP, including ABS and TCS. This program would also consider the rotational speed of each wheel, softening the torque set point of the driver in case of emergency.

Appendix A

Convective heat transfer coefficient calculation

The convective heat transfer coefficient links the convective heat flow to the difference between the temperature of the surface and the air (i.e., Equations (4.2) to (4.5)). This coefficient is calculated using the Nusselt number:

$$Nu = \frac{hL}{k_f} \tag{A.1}$$

where L is the characteristic length, h is the convection heat transfer coefficient, and k_f is the thermal conductivity of the fluid. The Nusselt number can be calculated using certain correlations that depend on the flow and the surface considered. Therefore, whether the convection is free or forced and, in the second case, whether the flow is laminar or turbulent must be determined using the dimensionless Reynolds (Re) number when forced convection is considered, or the Grashof (Gr) number when free convection is considered:

$$Re = \frac{vL}{\nu} \tag{A.2}$$

$$Gr = \frac{g\beta(T_s - T_{air})L^3}{\nu^2} \tag{A.3}$$

where v is the speed, L is the characteristic length, ν is the kinematic viscosity, g is gravitational acceleration, T_s and T_{air} are the temperatures of the surface and air, respectively, and β is the volumetric thermal expansion coefficient.

The correlations for each case and surface are as follows:

Forced convection (any surface):

Laminar flow:

$$\overline{Nu_x} = 0.664 Re^{1/2} Pr^{3/2} \tag{A.4}$$

Turbulent flow:

$$\overline{Nu_L} = \left(0.037 Re^{4/5} - 871\right) Pr^{1/3} \tag{A.5}$$

Free convection:

Horizontal flat plate (roof): Upper surface of hot plate or lower surface of cold plate:

$$\overline{Nu_L} = 0.54 Ra_L^{1/4} \left(10^4 < Ra_L \leq 10^7\right) \tag{A.6}$$

$$\overline{Nu_L} = 0.15 Ra_L^{1/3} \left(10^7 \leq Ra_L \leq 10^11\right) \tag{A.7}$$

Upper surface of cold plate or lower surface of hot plate:

$$\overline{Nu_L} = 0.27 Ra_L^{1/4} \left(10^5 < Ra_L \leq 10^10\right) \tag{A.8}$$

where:

Re - Reynolds number.

Pr - Prandtl number.

Ra - Rayleigh number.

Flat vertical plate:

$$Nu = \left(0.825 + \frac{0.837 Ra^{1/6}}{\left(1 + (0.492 Pr)^{9/16}\right)^{8/17}} \right)^2 \tag{A.9}$$

For a flat inclined plate (side and rear windows and windshield), correlation (A.9) can be used with the term $gcos(\varphi)$ representing gravity, where φ is the angle between the surface and the vertical axis, which is indicated in Table 4.2.

Bibliography

[1] Marcos D., Bordons C., Ridao M.A., Estudio Comparativo de Sistemas de Almacenamiento de Energa en un Vehculo Hbrido con Pila de Combustible. Jornadas de Automtica XXXI. Jaén, 2010.

[2] *www.acea.be/statistics* (Last visit: June 2014).

[3] Ahmed S.K., Chmielewski D.J., On the Tuning of Predictive Controllers for Hybrid Fuel Cell Vehicle Applications, Dynamics and Control of Process Systems, Volume #10 Part# 1, Dec. 2013, pp 129-134.

[4] Ambhl, D.,Sciarretta,A.,Onder,C.,Guzzella,L.,Sterzing,S.,Mann,K.,etal. A Causal Operation Strategy for Hybrid Electric Vehicles Based on Optimal Control Theory. In Proceedings of the 4th Braunschweig symposium on hybrid vehicles and energy management. 2007.

[5] Andujar J., Segura F., Fuel Cells: History and updating. A Walk Along Two Centuries. Renewable and Sustainable Energy Reviews 13, 2009, pp 2309-2322.

[6] Arce A., del Real A.J., Bordons C., Mpc for battery/fuel cell hybrid vehicle including fuel cell dynamics and battery performance improvement. J. Process Control, 19(8):1289-1304, 2009.

[7] Arce A., del Real A.J., Bordons C., Gutirrez M.B., Analysis of fuel cell dynamics and battery operation modes in a hybrid predictive controller for a fuel cell vehicle. In Fuel Cells Science and Technology 2008, Copenhagen, Denmark, 2008.

[8] Arxer M. and Martíez L.E., Hercules project: Contributing to the development of the hydrogen infrastructure. J. Power Sources, 171:224227, 2007.

[9] ASHRAE HANDBOOK FUNDAMENTALS, ed. Ashrae, 2005.

[10] *www.avontyres.es* (Last visit: July 2013).

[11] bALLARD FCgen-1020ACS Fuel Cell Stack and FCvelocity-1020ACS Fuel Cell Stack Product Manual and Integration Guide, Ballard Power Systems Inc., October 14, 2011.

[12] Baumann, B.,Rizzoni,G., Washington,G., Intelligent Control of Hybrid Vehicles Using Neural Networks and Fuzzy Logic. SAE Paper 981061. 1998.

[13] Beck R., Richert F., Bollig A., Abel D., Saenger S., Neil K., Scholt T., and Noreikat K. Model predictive control of a parallel hybrid vehicle driver. In Decision and Control, 2005 and 2005 European Control Conference. CDC-EC 05, pages 26702675, Seville, Spain, 2005.

[14] J. Bernard, S. Delprat, F. Buechi, T. Guerra, Global optimization in the power management of a fuel cell hybrid vehicle (FCHV), in: Proceedings of 2006 Vehicle Power and Propulsion Conference, 2006.

[15] C. Bordons, M.A. Ridao. Antonio Prez Espinosa, Alicia Arce and David Marcos. Model Predictive Control for Power Management in Hybrid Fuel Cell Vehicles. Vehicle Power and Propulsion Conference 2010 (VPPC 10), Lille, France, 2010

[16] Borhan, H.A., Vahidi,A., Model Predictive Control of a Power-Split Hybrid Electric Vehicle with Combined Battery and Ultracapacitor Energy Storage.In Proceedings of the American control conference, 2010,pp. 50315036.

[17] Bosch Motorsport ECU MS 5.2 Manual. 2012.

[18] Bosch Professional Automotive Information, Bosch Automotive Electrics and Automotive Electronics, 5th Edition, Springer Vieweg, 2007.

[19] Burckhardt M. Fahrwerktechnik: Radschlupf-Regelsysteme, Vogel Fachbuch, 1993.

[20] Cai W., Homs N., Ramírez de la Piscina P., Renewable hydrogen production from oxidative steam reforming of bio-butanol over CoIr/CeZrO2 catalysts: Relationship between catalytic behaviour and catalyst structure, Applied Catalysis B: Environmental, Volumes 150151, 5 May 2014, Pages 47-56.

[21] E.F. Camacho and C. Bordons. Model Predictive Control. 2004.

[22] Canudas de Wit C., Olsson H., Astrom K.J. and Lischinsky P. A New Model for Control of Systems with Friction, 1995, IEEE TAC, vol. 40, no. 3, pp.419 -425.

[23] Chen Y., Hedrick J.K., Guo K., A novel direct yaw moment controller for in-wheel motor electric vehicles, Vehicle System Dynamics, Vol. 51, No. 6, 2013, pages 925942.

[24] Chiang W.P., Yin D., Omae M., Shimizu H., Integrated Slip-Based Torque Control of Antilock Braking System for In-Wheel Motor Electric Vehicle, IEEJ Journal of Industry Applications Vol. 3, No. 4, 2014, pages 318-327.

[25] Cipollone, R.,Sciarretta,A., Analysis of the Potential Performance of a Combined Hybrid Vehicle with Optimal Supervisory Control.In Proceedings of the IEEE international conference on control applications. 2006.

[26] Corrêa F.C., Implementation of Heuristic Control Techniques in Power Management in Hybrid Vehicle Parallel Configuration. 22nd International Congress of Mechanical Engineering (COBEM 2013), Ribeiro Preto, SP, Brazil, November 3-7, 2013.

[27] Dave C.D., Pant K.K., Renewable hydrogen generation by steam reforming of glycerol over zirconia promoted ceria supported catalyst, Renewable Energy, Volume 36, Issue 11, November 2011, Pages 3195-3202.

[28] Del Real, A.J., Arce A., Bordons C., Development and experimental validation of a PEM fuel cell dynamic model, Journal of power sources 173 (1), 2007, pages 310-324.

[29] E. Dominguez, J.I Leon, C. Montero, D. Marcos, C. Bordons, M.A. Ridao, E.F. Camacho, E. Lopez, F. Rosa. Practical implementation of an hybrid electric-fuel cell vehicle, Industrial Electronics, 2009. IECON 09. 35th Annual Conference of IEEE, pp.3828-3833, 3-5 Nov. 2009

[30] Duffie J.A., Bechman W.A., Solar Engineering of Thermal Processes, 3rd ed., John Wiley & Sons Inc., U.S.A., 2006.

[31] Edrén J., Exploring force allocation control of over actuated vehicles. Licentiate thesis, KTH Royal Institute of Technology, Stockholm (Sweden), 2011.

[32] $http://www.eea.europa.eu/data-and-maps/indicators/final-energy-consumption-by-sector-5/assessment$(Last visit: July 2014).

[33] Al EmranHasan M. M., Motamed Ektesabi M., Kapoor A., An Investigation into Differential Torque Based Strategies for Electronic Stability Control in an In-Wheel Electric Vehicle, International Journal of Engineering and Innovative Technology Volume 2, Issue 7, January 2013

[34] Esmailzadeh E., Vossoughi G.R., Goodarzi A., Dynamic Modeling and Analysis of a Four Motorized Wheels Electric Vehicle, Vehicle System Dynamics, Vol. 35, Iss. 3, 2001, pages 163-194.

[35] "Corrective factors in equipments, CALENER-VYP, IDAE, Ministry of Industry, Tourism and Commerce (Spain), 2009. (Spanish).

[36] Faheem, Mahmud S.A., Khan G.M., Rahman M., Zafar H., A Survey of Intelligent Car Parking System. Journal of applied research and technology, 11(5), 2013, pages 714-726.

[37] Farzaneh Y.,Tootoonchi A.A., Controlling Automobile Thermal Comfort Using Optimized Fuzzy Controller, Applied Thermal Engineering, Volume 28, Issues 1415, October 2008, Pages 1906-1917.

[38] Fayazbakhsh, M. and Bahrami, M., Comprehensive Modeling of Vehicle Air Conditioning Loads Using Heat Balance Method, SAE Technical Paper 2013-01-1507, 2013.

[39] Freescale Semiconductor MPC5200B Data Sheet. Rev. 4, 02/2010.

[40] Fuhs A., Hybrid Vehicles and the Future of Personal Transportation, CRC Press, 2009.

[41] García P., Torreglosa J.P., Fernández L.M., Jurado F., Control Strategies for High-Power Electric Vehicles Powered by Hydrogen Fuel Cell, Battery and Supercapacitor, Expert Systems with Applications, Volume 40, Issue 12, 15 September 2013, Pages 4791-4804.

[42] $http://www.polaris.com/en-us/gem-electric-car/utility-vehicle/eL/pages/specifications.aspx$ Last visit: 02/10/2014.

[43] B. Geng, James K. Mills and Dong Sun. Two-Stage Energy Management Control of Fuel Cell Plug-In Hybrid Electric Vehicles Considering Fuel Cell Longevity. IEEE Trans. on Vehicular Technology, Vol 61, No 2, February 2012.

[44] Genta G., Morello L., Cavallino F., Filtri L., The Motor Car, Past, Present and Future. Springer, 2014.

[45] M. Gielniak, Z. Shen, Power management strategy based on game theory for fuel cell hybrid electric vehicles, in: Proceedings of 2004 Vehicular Technology Conference, Vol. 6, 2004, pp. 4422-4426.

[46] Gillespie T.D., Fundamentals of vehicle dynamics, SAE, Warrendale, PA, USA, 1992, pg. 227.

[47] *//www.gpsvisualizer.com/convert_input* (Last visit: January 2014).

[48] Grebe U.D. and Nitz L.T. VOLTEC - The propulsion system for Chevrolet Volt and Opel Ampera ATZ autotechnology 02/2011.

[49] Guemri M., Caux S., Ngueveu S.U., Messine F., A Better Alternative to Dynamic Programming for Offline Energy Optimization in Hybrid-Electric Vehicles. Electronics, Control, Measurement, Signals and their application to Mechatronics (ECMSM), 2013 IEEE 11th International Workshop of , vol., no., pp.1,2, 24-26 June 2013

[50] Gutiérrez J., Romo J., González M.I., Cañibano E., Merino J.C., Control Algorithm Development for Independent Wheel Torque Distribution with 4 In-wheel Electric Motors. Computer Modeling and Simulation (EMS), 2011 Fifth UKSim European Symposium on , vol., no., pp.257,262, 16-18 Nov. 2011

[51] Guzzella L., Sciarretta A., Vehicle Propulsion Systems, Third Edition. Springer, 2013.

[52] Hemi H., Ghouili J., Cheriti A., A real time fuzzy logic power management strategy for a fuel cell vehicle, Energy Conversion and Management, Volume 80, April 2014, Pages 63-70.

[53] Hwang, J.J., Chen Y.J., Kuo J.K. The Study on the Power Management System in a Fuel Cell Hybrid Vehicle. International Journal of Hydrogen Energy, volume 37, issue 5, 2012, pp. 4476-4489.

[54] Ibrahim B.S.K.K., Aziah M.A.N., Ahmad S., Akmeliawati R., Nizam H.M.I., Muthalif A.G.A., Toha S.F., M.K. Hassan, Fuzzy-based Temperature and Humidity Control for HV AC of Electric Vehicle, Procedia Engineering, Volume 41, 2012, pp 904-910.

[55] Incropera F.P., DeWitt D.P., Bergman T.L., Lavine A.S., Fundamentals of Heat and Mass Transfers, Sixth Edition, John Wiley & Sons Inc., U.S.A., 2006.

[56] Kasten F., Czeplak G., Solar and Terrestrial Radiation Dependent on the Amount and Type of Cloud, Solar Energy 24, 1980, pp. 177-189.

[57] *http://www.formula1.com/inside_f1/understanding_f1_racing/8763.html* (last visit: June 2014).

[58] Khayyam H., Kouzani A. Z., Hu E.J., Nahavandi S., Coordinated Energy Management of Vehicle Air Conditioning System, Applied Thermal Engineering, Volume 31, Issue 5, April 2011, pp. 750-764.

[59] Khayyam H., Adaptive Intelligent Control of Vehicle Air Conditioning System, Applied Thermal Engineering, Volume 51, Issues 1-2, March 2013, pp. 1154-1161.

[60] Khayyam H., Abawajy J., Jazar R.N., Intelligent Energy Management Control of Vehicle air Conditioning System Coupled with Engine, Applied Thermal Engineering, Volume 48, 15 December 2012, Pages 211-224.

[61] Khayyam H., Nahavandi S., Davis S., Adaptive Cruise Control Look-Ahead System for Energy Management of Vehicles, Expert Systems with Applications, Volume 39, Issue 3, 15 February 2012, Pages 3874-3885.

[62] Kiencke U., Nielsen L., Automotive Control Systems For Engine, Driveline, and Vehicle. Second edition. Germany, 2005.

[63] Kim T.S. Optimal control of a parallel hybrid electric vehicle with traffic preview. PhD thesis, Dept. of Mechanical Engineering, The University of Melbourne. 2011

[64] Kim, N.W.,Cha,S.K., Peng,H., Optimal Control of Hybrid Electric Vehicles Based on Pontryagin's Minimum Principle. IEEE Transactions On Control Systems Technology, 19(5), 2011, pp 12791287.

[65] T.S. Kim. Optimal control of a parallel hybrid electric vehicle with traffic preview. PhD thesis, Dept. of Mechanical Engineering, The University of Melbourne. 2011

[66] Kleimaier A. and Schroder D. An approach for the online optimized control of a hybrid powertrain. In Proceedings of the 7th International Workshop on Advanced Motion Control, Maribor, Slovenia, 2002.

[67] $http://www.laferrari.com/es/$ (last visit: June 2014).

[68] Lee, M., Lee, H., Won, H., Characteristic Evaluation on the Cooling Performance of an Electrical Air Conditioning System Using R744 for a Fuel Cell Electric Vehicle. Energies, Volume 5, Number 5, 2012, pp 1371-1383.

[69] Levinson R., Pan H., Ban-Weiss G., Rosado P., Paolini R. Akbari H. Potential Benefits of a Solar Reflective Car Shells: Cooler Cabins, Fuel savings and Emission Reductions, Applied Energy 88, 2011, pp. 4343-4357.

[70] Li D., Ishikawa C., Koike M., Wang L., Nakagawa Y., Tomishige K., Production of renewable hydrogen by steam reforming of tar from biomass pyrolysis over supported Co catalysts, International Journal of Hydrogen Energy, Volume 38, Issue 9, 27 March 2013, Pages 3572-3581.

[71] C. Lina, J. Kang, J. Grizzle, and H. Peng. Energy management strategy for a parallel hybrid electric truck. In SAE 2000 World Congress,Detroit, Michigan, USA, 2000.

[72] Liu W., Introduction to Hybrid Vehicle System Modeling and Control. John Wiley & Sons Inc., Hoboken, New Jersey, 2013.

[73] Marcos D., Bordons C., Wideberg J., Mántaras D.A., Luque P., Desarrollo Y Validacin Experimental De Un Modelo Dinmico Para Un Vehculo Elctrico Con Motores En Las Ruedas. Actas de las XXXIV Jornadas de Automtica, pp. 545-549, 4-6 Sept 2013.

[74] Macek K., Thoma K., Glatzel R., and Siegwart R. Dynamics Modeling and Parameter Identification for Autonomous Vehicle Navigation. In Intelligent Robots and Systems, 2007. IROS 2007. IEEE/RSJ International Conference on, pages 33213326.

[75] Manrique T., Malaise H., Fiacchini M., Chambrion T., Millerioux G., Model predictive real-time controller for a low-consumption electric vehicle, Environment Friendly Energies and Applications (EFEA), 2012 2nd International Symposium on, 25-27 June 2012, pp.88-93.

[76] Mántaras D.A., Luque P., Virtual test rig to improve the design and optimization process of the vehicle steering and suspension systems, Vehicle System Dynamics, vol. 50, n 10, pp. 1563-1584, 2012.

[77] Mekhilefa S., Saidurb R., Safari A., Comparative Study of Different Fuel Cell Technologies, Renewable and Sustainable Energy Reviews 16, pages 981-989, 2012.

[78] $http://www.mercedes-benz-classic.com/content/classic/mpc/mpc\_classic\_website/en/mpc\_home/mbc/hon$ (Last visit: June 2014).

[79] Merzhab A., Bouzidi M. Computation of Thermal Comfort Inside a Passenger Car Compartment, Applied Thermal Engineering 26, 2006, pp. 1679-1704.

[80] Meyer R.T., DeCarlo R. A., Meckl P. H., Doktorcik C., Pekarek S., Hybrid Model Predictive Power Management of A Fuel Cell-Battery Vehicle. Asian Journal of Control, 15. Pages 363379. 2013.

[81] Miranda Á.G., Chen T.S., Hong C.W., Feasibility Study of a Green Energy Powered Thermoelectric Chip Based Air Conditioner for Electric Vehicles, Energy, Volume 59, 15 September 2013, pp. 633-641.

[82] Mokrani Z., Rekioua D., Rekioua T., Modeling, Control and Power Management of Hybrid Photovoltaic Fuel Cells with Battery Bank Supplying Electric Vehicle, International Journal of Hydrogen Energy, Available online 30 April 2014

[83] Murphey Y.L., Park J., Kiliaris L., Kuang M.L., Masrur M.A., Phillips A.M., Wang Q. Intelligent Hybrid Vehicle Power Controlpart II: Online Intelligent Energy Management. IEEE Transactions on Vehicular Technology. Vol. 62, no. 1, 2012, pp. 69-79.

[84] NHTSA, Office of Regulatory Analysis and Evaluation National Center for Statistics and Analysis, Electronic Stability Control Systems Federal Motor Vehicle Safety Standards (FMVSS) No. 126. March 2007.

[85] Noori K., Jenab K., Fuzzy Reliability-Based Traction Control Model for Intelligent Transportation Systems, Systems, Man, and Cybernetics: Systems, IEEE Transactions on , vol.43, no.1, pp.229,234, Jan. 2013.

[86] Odeim F., Roes J., Wlbeck L., Heinzel A., Power Management Optimization of Fuel Cell/Battery Hybrid Vehicles with Experimental Validation, Journal of Power Sources, Volume 252, 15 April 2014, Pages 333-343.

[87] $http://www.oica.net/category/vehicles-in-use/$ (Last visit: June 2014).

[88] $http://www.oica.net/category/climate-change-and-co2/$ (Last visit: July 2014).

[89] OKneefe M. and Markel T. Dynamic programming applied to investigate energy management strategies for a plug-in hev. In Proceedings of the 22nd Internatinal Battery, Hybrid and Fuel Cell Electric Vehicle Symposium and Exposition, EVS-22, Yokohama, Japan, 2006.

[90] Ozeki Y., Takabayashi T., Tanabe S., Effects of Spectral Properties of Glass on the Thermal Comfort of Car Occupants, In: Yutaka Tochihara and Tadakatsu Ohnaka, Editor(s), Elsevier Ergonomics Book Series, Elsevier, 2005, Volume 3, pp 289-297.

[91] Pacejka H.B. Tyre and Vehicle Dynamics. 2006 Elsevier.

[92] Pacejka H.B., Tyre and Vehicle Dynamics, Butterworth-Heinemann, Oxford, UK, 2002.

[93] Parotto M., Sgatti S., Sensi F., Advanced GDI Injector Control with Extended Dynamic Range, SAE Technical Paper 2013-01-0258, 2013.

[94] Pethaiaha S.S., Subiantoroa A., Stimminga U., The Application of Intermediate Temperature Fuel Cell for the Auxiliary Power Unit of the Air Conditioning System in an Electric Vehicle, ECS Transactions, Volume 53, Issue 30, 2013, pp. 3-9.

[95] Preitl Z., Bauer P., Kulcsar B., Rizzo G., and Bokor J. Control solutions for hybrid solar vehicle fuel consumption minimization. In Proceedings of the 2007 IEEE Intelligent Vehicles Symposium, Istanbul, Turkey, 2007.

[96] Qian H., Xu G., Yan J., Lam T.L., Xu Y., Xu K., Energy management for four-wheel Independent Driving Vehicle, Intelligent Robots and Systems (IROS), 2010 IEEE/RSJ International Conference on , vol., no., pp.5532,5537, 18-22 Oct. 2010

[97] Rahman Z., Butler K., and Ehsani M.. A comparison study between two parallel hybrid control concepts. In Proceedings of the 2001 American Control Conference, Arlington, VA, USA, 2001.

[98] Rodatz P., Paganelli G., Sciarretta A., Guzzella L.. Optimal power management of an experimental fuel cell/supercapacitor-powered hybrid vehicle. Science Direct; Control Engineering Practice 13. 2005, pages 4153.

[99] Society of Automotive Engineers, Vehicle Dynamics Terminology, SAEJ670e, SAE, Warrendale, PA, 1976.

[100] Sanaye S., Masoud D., Amir F. Temperature Control of a Cabin in an Automobile Using Thermal Modeling and Fuzzy Controller, Applied Energy 97, 2012, pp. 860-868.

[101] Schouten N.J., Salman M.A. and Kheir N.A. Energy management strategies for parallel hybrid vehicles using fuzzy logic. Control Engineering Practice, 11:171177, 2003.

[102] A. Sciarretta, M. Back, and L. Guzzella. Optimal control of parallel hybrid electric vehicles. IEEE Transactions on Control Systems Technology, 12(3):171-177, May 2004.

[103] Sciarretta A., Guzzella L., and Back M. Real-time optimal control strategy for parallel hybrid vehicles: from global optimization towards real-time control. In Proceedings of the IFAC Symposium on Advances an Automative Control, Salerno, Italy, 2004.

[104] Sciarretta A., Serrao L., Dewangan P.C., Tona P., Bergshoeff E.N.D., Bordons C., Charmpa L., Elbert Ph., Eriksson L., Hofman T., Hubacher M., Isenegger P., Lacandia F., Laveau A., Li H., Marcos D., Nesch T., Onori S., Pisu P., Rios J., Silvas E., Sivertsson M., Tribioli L., van der Hoeven A.-J., Wu M., A control benchmark on the energy management of a plug-in hybrid electric vehicle, Control Engineering Practice, Volume 29, August 2014, Pages 287-298.

[105] Sigal A., Leiva E.P.M., Rodríguez C.R., Assessment of the potential for hydrogen production from renewable resources in Argentina, International Journal of Hydrogen Energy, Volume 39, Issue 16, 27 May 2014, Pages 8204-8214.

[106] Simmons K., Guezennec Y., Onori S., Modeling and Energy Management Control Design for a Fuel Cell Hybrid Passenger Bus, Journal of Power Sources, Volume 246, 15 January 2014, Pages 736-746.

[107] Sivertsson M., Adaptive Control Using Map-Based ECMS for a PHEV. E-COSM'12 – IFAC Workshop on Engine and Powertrain Control, Simulation and Modeling. 2012.

[108] Song J., Boo K., Performance Evaluation of Traction Control Systems Using a Vehicle Dynamic Model, Proceedings of the Institution of Mechanical Engineers, Part D: Journal of Automobile Engineering July 1, 2004, pages 685-696.

[109] Tang Y., Zhang X., Zhang D., Zhao G., Guan X., Fractional Order Sliding Mode Controller Design for Antilock Braking Systems, Neurocomputing, Volume 111, 2 July 2013, Pages 122-130

[110] Tapani A., Vehicle Trajectory Effects of Adaptive Cruise Control, Journal of Intelligent Transportation Systems, Vol. 16, Iss. 1, 2012.

[111] $http://www.toyota.es/innovation/coches\_hibridos.tmex$ (In Spanish. Last visit July 2014).

[112] $http://www.toyota.es/innovation/design/concept\_cars/fcv-r/index.tmex$ (In Spanish. Last visit June 2014).

[113] $http://www.toyota.es/innovation/design/concept\_cars/fchv/index.tmex$ (In Spanish. Last visit June 2014).

[114] Tsai M., Tseng C., Lin Y., Power Management and Control of an Electric Vehicle with Auxiliary Fuel Cell and Wind Energies," TENCON 2013 - 2013 IEEE Region 10 Conference (31194) , vol., no., pp.1,4, 22-25 Oct. 2013.

[115] Tulpule P., Marano V., Rizzoni G., Effects of different PHEV control strategies on vehicle performance, American Control Conference, 2009. ACC '09, 10-12 June 2009, pages 3950,3955.

[116] Tuza P.V., Manfro R.L., Ribeiro N.F.P., Souza Mariana M.M.V.M., Production of renewable hydrogen by aqueous-phase reforming of glycerol over NiCu catalysts derived from hydrotalcite precursors, Renewable Energy, Volume 50, February 2013, Pages 408-414.

[117] Wang J., Wang Q., Jin L., Song C., Independent Wheel Torque Control of 4wd Electric Vehicle for Differential Drive Assisted Steering, Mechatronics, Volume 21, Issue 1, February 2011, Pages 63-76.

[118] Wang H., Xiang L., Numerical Simulation of Air conditioning Vehicle Using Computational Fluid Dynamics, Power and Energy Engineering Conference, APPEEC 2009. Asia-Pacific, 27-31 March 2009, pp.1,4.

[119] Wipke K., Cuddy M., and Burch S. Advisor 2.1: A user-friendly advanced powertrain simulation using a combined backward/forward approach. IEEE Transactions on Vehicular Technology, 48(6):17511761, November 1999.

[120] Wipke K., Markel T., and Nelson D. Optimizing energy management strategy and degree of hybridization for a hydrogen fuel cell suv. In International Electric Vehicle Symposium EVS 18, Berlin, Germany, 2001.

[121] Wu X., Du J., Hu C., Ding N., The Economic Analysis of a Plug-in Series Hybrid Electric Vehicle in Different Energy Management Strategy. Vehicle Power and Propulsion Conference (VPPC), 2013 IEEE, 15-18 Oct. 2013, pp.1,5.

[122] Wu C., Sun Z., Design and Control of a Direct Fuel Injector with Rate Shaping Capability, American Control Conference (ACC) 2013, 17-19 June 2013, pages 3637-3642.

[123] Yang I., Byun S., Seo B., Lee D., Han D.S., Integrated Control Systems of Active Front Steering and Direct Yaw Moment Control Using Dynamic Inversion, IEEE Intelligent Vehicles Symposium (IV) Gold Coast, Australia, June 23-26, 2013.

[124] Yu H., Huang M., Zhang Z., Direct Yaw-Moment Hinfinity Control of Motor-Wheel Driving Electric Vehicle, Vehicle Power and Propulsion Conference (VPPC), 2013 IEEE, 15-18 Oct. 2013, pp.1,5.

[125] Zanon M., Frasch J.V., Diehl M., Nonlinear Moving Horizon Estimation for Combined State and Friction Coefficient Estimation in Autonomous Driving, 2013 European Control Conference (ECC), 17-19 July 2013, pages 4130-4135.

[126] Zhang L., Li L., Lin C., Wang C., Qi B., Song J., Coaxial-Coupling Traction Control For a Four-Wheel-Independent-Drive Electric Vehicle on a Complex Road, Proceedings of the Institution of Mechanical Engineers, Part D: Journal of Automobile Engineering June 9, 2014.

+

Glossary

Nomenclature

Chapter 1

Chapter 2

C_p	heat capacity
J	cost function
p	prediction horizon
P	power
T	temperature
u	manipulated variable
V	voltage
y	output

Chapter 3

D	distance
E	energy
F	force
g	gravitational acceleration
m	mass
P	power
r	radius
T	torque
t	time
v	speed

Chapter 4

A	area
C	thermal inertia
C_p	heat capacity

e thickness
G solar irradiance
h convective heat transfer coefficient
k thermal conductivity
m mass
Q heat flow
T temperature

Chapter 5

Chapter 6

C_{ax} drag factor
F force
g gravitational acceleration
r yaw rate
S slip
T torque
v speed

Subscripts

Chapter 1

Chapter 2

amb ambient
avg average
max maximum
min minimum
opt optimal
$perf$ performance
st stack

Chapter 3

avg average
bat batteries
c carrier
el electric
eng engine
f final
max maximum
$mech$ mechanical

nr non regenerative
pwt powertrain
r ring
regen regenerative
rem remaining
s sun
sp set point
tot total

Chapter 4

a absorbed
cd conduction
cv convection
inc incident
lsw left side window
r reflected
rd radiation
rsw right side window
rw rear windows
t transmitted
ws windshield

Chapter 5

Chapter 6

B Burckhardt
CG center of gravity reference system
eff effective
fl front left
fr front right
G global reference system
g gravity
L longitudinal
ls low speed
res resultant
rl rear left
roll rolling
rr rear right
S side
th threshold (high)
tl threshold (low)
w velocity reference system

Greek symbols

Chapter 1

Chapter 2

ε constraint softening coefficient

Chapter 3

α road slope
ρ gear ratio
ω angular velocity

Chapter 4

α absorptivity
τ transmisivity
ε emisivity
σ Stefan-Boltzman constant
ρ reflectivity

Chapter 5

Chapter 6

α wheel slip angle
μ friction coefficient
ρ density

Acronyms

4WD Four Wheel Drive

ABS Anti-lock Braking System

ACC Adaptive Cruise Control

ACEA Association des Constructeurs Europens d'Automobiles

ACS Air Conditioning System

ARTEMIS (Assessment and Reliability of Transport Emission Models and Inventory Systems)

BEV Battery-powered Electric Vehicle

BMS Battery Management System

CAD Computer-Aided Design

CD-CS Charge Depleting - Charge Sustaining

COP Coefficient Of Performance

CVM Cell Voltage Monitor

DoF Degree of Freedom

DoH Degree of Hybridness

EEA European Environment Agency

ECMS Equivalent Consumption Minimization Strategy

ECR Equal Concern for the Relaxation

ECU Electronic Control Unit

ESP Electronic Stability Program

EM Electric Motor

EPA Environmental Protection Agency

FIA Federation Internationale de l'Automobile

EREV Extended-Range Electric Vehicle

EV Electric Vehicle

FC Fuel Cell

FCV Fuel Cell Vehicle

FCHV Fuel Cell Hybrid Vehicle

FMVSS Federal Motor Vehicle Safety Standards

FUDS Federal Urban Driving Schedule

GEM Global Electric Motorcars

GPS Global Positioning System

HEV Hybrid Electric Vehicle

HMI Human-Machine Interface

HV Hybrid Vehicle

HVAC Heating, Ventilation, and Air Conditioning

ICEV Internal Combustion Engine Vehicle

ICE Internal Combustion Engine

ICEHV Internal Combustion Engine Hybrid Vehicle

IMU Inertial Measurement Unit

INTA National Institute for Aerospace Technology

KERS Kinematic Energy Recovery System

LPG Liquefied Petroleum Gas

MIMO Multiple Input Multiple Output

MPC Model Predictive Control

NEDC New European Driving Cycle

NHTSA National Highway Traffic Safety Administration

OICA Organisation Internationale des Constructeurs d'Automobiles

PHEV Plug-in Hybrid Electric Vehicle

PEM Proton Exchange Membrane

PMSM Permanent Magnet Synchronous Motor

RAM Random Access Memory

RMS Root Mean Square

ROM Read Only Memory

RWD Rear Wheel Drive

SAE Society of Automotive Engineers

SISO Single Input Single Output

SOC State Of Charge

TCS Traction-Control System

UC Ultra Capacitor

UDDS Urban Dynamometer Driving Schedule

ZEV Zero Emission Vehicle

Resumen

Introducción

Justificación

Desde el descubrimiento de la rueda, el transporte por carretera ha tenido un papel vital en la historia de la humanidad, para transporte de mercancías, animales o personas. En la década de 1880, Karl Benz patentó los primeros coches con motor de combustión interna, que en poco tiempo se convertiría en el principal modo de tracción.

Hoy, el número de vehículos no para de crecer, y las emisiones de los mismos suponen un problema, reconocido por casi todos los organismos competentes. El precio del combustible y una mayor preocupación por el medio ambiente está abriendo una tendencia en fabricantes y consumidores hacia unos vehículos con menos emisiones.

A su vez, los consumidores no quieren renunciar a las posibilidades y comodidades de los vehículos actuales. Por lo tanto, los vehículos del futuro deberán tener al menos la misma potencia, e incorporar avances en comodidad y seguridad.

Control automático en vehículos

Como en todos los campos tecnológicos, la automoción ha sufrido un gran cambio en los últimos aos, debido al uso de microprocesadores. Los coches hoy tienen kilómetros de cable, frente a las no más de 40 líneas que había antao, para alimentar las luces, las bujías y el motor de arranque.

La primera mejora significativa fue la introducción de la inyección en los aos sesenta, sistema que optimiza la entrada de combustible al motor, proporcionando mayor potencia con un menor consumo. En los aos setenta Bosch desarrolló el sistema ABS, que constituyó un hito, pues fue el primero que actuaba para cambiar la dinámica del coche, en este caso evitando el bloqueo de las ruedas en el frenado, acortando la distancia de frenado y evitando la pérdida de control por parte del conductor. En los aos siguientes, cientos de sistemas electrónicos fueron introducidos en los coches, como elevalunas eléctrico, sensor de lluvia o airbag.

Todos estos sistemas están controlados por un sistema electrónico, llamado ECU. Los coches modernos suelen montar más de cien ECUs, que se ocupan de labores específicas, a distintos niveles. La más importante es la que se encarga del control del motor, inyección, etc. Cada ECU lee los sensores relativos a su función, procesa la información, y envía la seal de control adecuada a los actuadores. A su vez, pueden enviar o recibir información de

otras ECUs, para actuar de manera coordinada, o compartir información de determinados sensores.

Los sistemas de control se pueden dividir en tres categorías: sistemas que no influyen directamente en el comportamiento del coche (cierre centralizado, control del ángulo de los faros), sistemas que ayudan al conductor (ABS) y sistemas que sustituyen al conductor (velocidad de crucero, conducción autónoma). De estos, el primero y el tercero quedan fuera del estudio de esta tesis. En cuanto al segundo, hay numerosas líneas de investigación abiertas. Con un vehículo con motor de combustión interna (ICEV), los controladores actúan sobre los frenos y la inyección. Los motores eléctricos facilitan este control, mientras que en el caso de los vehículos con motores en cada rueda, la actuación se hace directamente en cada motor, posibilitando un mayor y mejor control.

Coches híbridos

Un coche híbrido es aquel que tiene más de un tipo de sistema de almacenamiento de energía. Por ejemplo: gasolina y baterías. Pese a que el primer coche híbrido se fabricó hace más de cien aos, ha sido desde la comercialización del Toyota Prius (1997) cuando han sido una opción real frente a los ICEVs. Hoy cada vez están más extendidos, y ya casi todas las marcas incluyen al menos algún micro-híbrido, con el sistema de parada automática del motor cuando el coche está detenido. Quizás la tendencia más fuerte ahora mismo sea la de los híbridos enchufables (PHEVs), que ofrecen la posibilidad de cargar el coche desde la red eléctrica.

Existen tres arquitecturas básicas de vehículos híbridos: en serie, en paralelo y combinada. En la primera el ICE (o en su caso otra fuente auxiliar de potencia) mueve un generador, cuya potencia eléctrica va al bus de potencia, donde se reparte entre el motor que da la tracción a las ruedas y la recarga de baterías. En la configuración paralela, tanto el ICE como el motor eléctrico están conectados a un sistema mecánico, de manera que ambos aportan tracción a las ruedas. Finalmente en la arquitectura combinada el ICE aporta tanto tracción como movimiento al generador para que se genere energía eléctrica.

Aunque el combustible líquido es junto a las baterías la fuente de energía más común en coches híbridos, todas las compaías están investigando con otras fuentes. La que mayor fuerza tiene en este momento es el hidrógeno. Así, las pilas de combustible (FCs) toman este combustible y oxígeno del ambiente, generando energía eléctrica, y agua como único residuo. De esta forma, y teniendo en cuenta que el hidrógeno puede obtenerse por fuentes renovables, el coche con pila de hidrógeno resulta un vehículo respetuoso con el medio ambiente, y cuya fuente de energía no es limitada, como en el caso de los **IECV!** (**IECV!**)s.

Objetivos de la tesis

El objetivo de esta tesis es cubrir los principales problemas de control para tres tipos de vehículos híbridos: ICE PHEVs, FCHVs y vehículos con motores independientes en cada rueda. Coches que representan las principales tendencias en automoción a corto y medio plazo.

Control de potencia en FCHVs

En este capítulo se presentan dos vehículos híbridos con pila de combustible, que pertenecen a los proyectos Delfín y Hércules, desarrollados junto a los grupos de investigación de distintas corporaciones públicas y privadas. En estos coches se prueban varias configuraciones para este tipo de vehículo, y en el caso del segundo se hace un modelo del sistema de potencia y un controlador para el mismo.

Proyectos Delfín

En los proyectos Delfín I y II se ha partido de un vehículo eléctrico comercial (GEM eL), al que se le han aadido una serie de dispositivos para convertirlo en un vehículo híbrido.

Delfín I

En el Delfín I al coche original se le aadió una pila pila de combustible de 12 kW, un sistema de almacenamiento de hidrógeno y un convertidor de potencia para acoplar la pila de combustible al sistema eléctrico de potencia existente en el coche. A su vez, se instaló un sistema de control para gestionar los flujos de potencia entre los distintos dispositivos y un entorno gráfico interactivo para el usuario.

El sistema se probó bajo distintas condiciones de conducción, comprobándose que era capaz de suministrar la potencia necesaria para satisfacer los requerimientos el conductor.

Delfín II

Basado en el mismo coche que el Delfín I, el sistema de almacenamiento de hidrógeno y el motor eléctrico son los dos únicos elementos de potencia que se mantienen respecto a la primera versión. Las baterías se sustituyeron de 6 a 4 baterías de gel de 12V, el convertidor de potencia tuvo que ser rediseado, y la pila de combustible fue cambiada por dos *stacks* de 1'2 kW.

En este caso el sistema de control se divide en tres niveles. El nivel superior se encarga de la gestión de potencia global del vehículo. Recibe como referencia la posición del pedal del acelerador (lo que aporta una estimación de la potencia requerida por el conductor), y envía las referencias de potencia a los controladores de las pilas de combustible y a los convertidores de potencia. El segundo nivel divide la potencia requerida para las pilas por el controlador anterior entre las dos pilas. Por último, el controlador de bajo nivel se encarga del control interno de cada una de las pilas (temperatura y flujo de aire).

Este sistema fue probado experimentalmente, comprobándose el buen funcionamiento de las pilas, así como del control de potencia, satisfaciendo los requerimientos del conductor.

Proyecto Hércules

El proyecto Hércules, y en particular su subproyecto .[El] Leónçonsiste en el diseo y montaje del prototipo de un vehículo híbrido con pila de combustible. Este parte del chasis de un Santana 350, sobre el que se montan todos los dispositivos de potencia. Estos son:

- Una pila de combustible de 56 kW, junto a su sistema de almacenamiento de hidrógeno (hasta 2'4 kg de hidrógeno).
- un pack de baterías de ión litio, consistente en cuatro módulos en serie, de trece celdas de 3'7V, también en serie.
- Un motor síncrono de imanes permanentes, de potencia nominal 66 kW y par máximo de 460 Nm.

El sistema de potencia de este vehículo ha sido modelado para probar distintas configuraciones o estrategias de control. Sobre este modelo se ha implementado un controlador MPC para la gestión de potencia. Dicho controlador recibe como entradas la potencia requerida y el estado de carga de las baterías, siendo las variables manipuladas las referencias de potencia a los distintos dispositivos: motor, pila de combustible, baterías y resistencia de frenado.

El controlador penaliza tanto la potencia requerida a cada fuente como su variación. Por otra parte las restricciones aseguran que los dispositivos no se salgan de sus rangos de funcionamiento y fuerzan al controlador a aportar la potencia requerida por el conductor.

Finalmente, el modelo se amplió con la inclusión de una nueva fuente de energía: los supercondensadores, adaptando para ello el controlador. Se probaron otras dos configuraciones, sustituyendo estos total o parcialmente a las baterías.

Gestión de potencia de un PHEV bastado en la estimación de la energía del ciclo

En este capítulo se trabaja sobre el modelo del sistema de potencia del PHEV *Chevrolet Volt*, aportado por los organizadores de la sesión especial para un benchmark en el congreso Ecosm 2012. El modelo incluía un conductor virtual, cuya salida era el par requerido de manera que el coche siguiera un determinado ciclo. El controlador debía proporcionar esta potencia, minimizando el consumo final de baterías y combustible, y consumiendo los mínimos recursos posibles (memoria y tiempo de CPU), evidentemente sin sobrepasar las restricciones de cada dispositivo.

El vehículo tiene un ICE, dos motores eléctricos (motor y generador) y tres embragues, permitiendo cuatro modos de funcionamiento: eléctrico puro con uno o dos motores, *range extender* y *power split*. El controlador tiene como entradas la demanda de par, el par máximo regenerativo, la velocidad del vehículo, el estado de carga de las baterías y una estimación de la distancia total y de la velocidad media del trayecto completo. Como salidas tiene los pares de los tres motores, la velocidad del generador, y el estado de los tres embragues (abierto/cerrado) y del ICE (apagado/encendido).

El controlador propuesto se divide en dos niveles. En el nivel más alto se estima la energía que el vehículo va a necesitar para completar el ciclo a través de los datos aproximados de distancia total y velocidad media. Esta estimación se irá corrigiendo según avance el tiempo. A la vez, a partir del SOC calcula la energía restante en las baterías. De esta manera se estima la energía que debe aportar el motor de combustión. La energía de las baterías se administrará de manera que el ICE pueda funcionar de la manera más eficiente posible.

El nivel más bajo recoge las referencias del más alto, y gestiona los modos de funcionamiento y la potencia de cada dispositivo de la forma más eficiente posible, a la vez que cuida que se cumplen las restricciones.

Para probar el controlador, se realizaron varias pruebas tanto de aceleración como de comportamiento en ciclos de conducción, resultando un controlador eficaz, pues cumplió todas las restricciones, sencillo, lo cual disminuye el uso de memoria y tiempo de CPU y eficiente, dado que el controlador trata de minimizar el consumo tanto a nivel de planificación (alto nivel) como de actuación (bajo nivel).

Desarrollo y validación de un modelo térmico para el habitáculo de un vehículo

En un vehículo con motor de combustión interna el calor para la calefacción se toma del circuito de refrigeración del motor, mientras que el compresor del aire acondicionado se acopla al motor mediante un embrague. En los coches eléctricos e híbridos el motor de combustión, en caso de haberlo, no está siempre activo, y el motor eléctrico no sufre un calentamiento tan grande ni tiene un ralentí: cuando el coche está parado, el motor también lo está. Por lo tanto es necesario un nuevo sistema de calefacción, ventilación y aire acondicionado (HVAC). Este sistema debe estar presente en el cálculo de consumo del coche. Se hace necesario por tanto el desarrollo de un modelo térmico del habitáculo del coche para conocer la transferencia de calor del aire del mismo, y estimar así el consumo del sistema de HVAC.

En este capítulo se describe un modelo para el habitáculo de un BMW serie 1. Para el mismo se han hecho las siguientes suposiciones: las superficies que delimitan el habitáculo son planas, la inercia térmica tanto de los cristales como del techo es despreciable y las únicas superficies del vehículo que intercambian calor con el exterior son los cristales y el techo.

El aire del habitáculo intercambia calor con:

- Ocupantes del coche. El calor transferido es hallado a partir de los valores calculados por ASHRAE.
- Elementos internos del vehículo. Estos se modelan como una superficie con una inercia térmica, estimada a partir de ensayos experimentales. Se supone que la radiación que entra en el habitáculo incide en estos elementos.
- El aire exterior, a partir del flujo másico por filtraciones y el sistema de ventilación.
- Las superficies internas de los cristales y el techo por convección.

El flujo de calor en las paredes del habitáculo se calcula a partir de ecuaciones teóricas y correlaciones experimentales, teniendo en cuenta la radiación incidente, la convección exterior, la conducción y finalmente la convección interior.

Para validar el modelo, se instaló una red de sensores de temperatura en un coche real, realizando tres tipos de pruebas: coche vacío y parado en un aparcamiento subterráneo, coche vacío y parado al aire libre y coche con un ocupante moviéndose, al aire libre. La similitud de los resultados experimentales y de las simulaciones permite validar el modelo.

Gestión de potencia en vehículos híbridos con HVAC

En este capítulo se utiliza el modelo térmico del habitáculo de un vehículo para calcular la influencia del sistema HVAC sobre un coche híbrido. Para ello se incluye este modelo en el modelo del sistema de potencia del vehículo en estudio.

Modelo de aire acondicionado

Este modelo no puede ser introducido directamente. Es necesario acoplar entre los dos un tercer modelo, del propio HVAC, que calcule la potencia del compresor a partir del cálculo de la transferencia de calor hacia el aire del habitáculo. El modelo del habitáculo ha sido mejorado, aadiendo el cálculo de la humedad y del calor latente.

El modelo de HVAC calcula esta potencia a partir de los datos del propio sistema de refrigeración (capacidad y COP nominales) y de una serie de factores de corrección, que tienen en cuenta la influencia sobre el sistema de trabajar fuera de su punto nominal.

Integración y resultados

El modelo del habitáculo junto con el de aire acondicionado se integró en dos modelos del sistema de potencia vehículos híbridos de distintos tipos y fuentes de energía. Por una parte se integró en el modelo de un FCHV formado por un BMW serie 1 con pila de combustible, y con un controlador MPC como el expuesto en el Capítulo 2. Se realizaros varias simulaciones, cambiando las condiciones meteorológicas, el número de ocupantes y el SOC inicial para dos ciclos de conducción: uno urbano (FUDS) y otro de autopista (ARTEMIS highway).

De la misma manera se integró el modelo en el PHEV descrito en el Capítulo 3, donde se realizaron simulaciones para distintas condiciones meteorológicas y número de ocupantes, para los mismos ciclos de conducción que el vehículo anterior.

A su vez, se realizaron las mismas simulaciones con el aire acondicionado desconectado. Comparando los resultados, se demuestra que el consumo del sistema de aire acondicionado incrementa normalmente entre un 3 y un 9 % el consumo de energía, llegando a valores de hasta el 35 % en el ciclo de ciudad del híbrido enchufable.

Modelado y control de par de un vehículo con cuatro motores en ruedas

Descripción del vehículo

En este capítulo se trabaja sobre el prototipo FOX. Se trata de un coche montado sobre una variante del chasis del coche de competición *Silver Car S2*. A este coche se le han montado cuatro motores en rueda, con una potencia nominal de 7 kW cada uno, así como sus respectivos convertidores/controladores. Estos motores están alimentados por seis módulos de baterías LiFeMnPO4, de 12.8V y 100Ah cada una. En un futuro se le aadirán otras dos fuentes de energía: una pila de combustible y un módulo de supercondensadores.

El vehículo incluye una serie de sensores con dos objetivos principales: medir la posición de los dispositivos del conductor y conocer la posición y el comportamiento del vehículo. Para el primero se utilizan tres potenciómetros, que miden el recorrido de los pedales de aceleración y freno, y el ángulo del volante. Para el segundo objetivo se utilizan cuatro potenciómetros para medir el recorrido de las suspensiones, una Unidad de Medida Inercial IMU para medir las aceleraciones (lineales y angulares) en los tres ejes, y las velocidades angulares, también en los tres ejes y un GPS, incluido en la IMU (localización geográfica y velocidad). A esto hay que aadir los datos de los sensores internos de las baterías (SOC, tensión, intensidad) y de los motores y convertidores (intensidad, velocidad angular del motor).

Modelo CAD

Se ha hecho un modelo del vehículo en CAD, utilizando el software *Solidworks*. Este diseo está basado en el modelo del chasis, suministrado por el fabricante. A él se le han aadido la suspensión, los motores, las ruedas, la dirección, los dispositivos de potencia y los modelos de dos ocupantes. Se han hecho dos variantes para la suspensión delantera y dirección: uno más sencillo en el que el punto de contacto entre la rueda y el suelo está siempre en el centro de la banda de rodadura del neumático, y otro más complejo, que se ajusta más al sistema real. Este modelo CAD será portado a dos *softwares* se simulación: *ADAMS/ADAMS Car* y *Matlab Simulink-Simmechanics*, que usarán las variantes compleja y sencilla de la dirección respectivamente.

Modelo en Simulink-Simmechanics

Mediante la herramienta Simmechanics-link, el modelo del coche en Solidworks fue portado a Simulink-Simmechanics. En este quedan definidos todos los sólidos (bodies) y las uniones entre los mismos (joints).

Sin embargo, por su complejidad, la interacción entre los neumáticos y el asfalto no se modela directamente, por lo que es necesario crear un subsistema que calcule estas fuerzas. Para ello se ha utilizado el modelo de Burckhardt, que relaciona el deslizamiento longitudinal y lateral con la fuerza entre el suelo y el neumático. De esta forma, el modelo calcula en cada iteración la aceleración de la rueda a través del par, y con esta el movimiento. El deslizamiento se calcula a partir de la relación entre le velocidad del neumático y la de la propia rueda y del ángulo entre los vectores del eje longitudinal de la rueda y el de la velocidad de la misma. A partir de los deslizamientos calcula las fuerzas.

Para el sistema de dirección se ha supuesto un modelo de Ackermann basado en las medidas del sistema real.

El modelo ha sido validado comparando la trayectoria del sistema simulado con trayectorias reales en las mismas condiciones, tanto con tracción total como con propulsión.

Controladores de distribución de par

Al ser los cuatro motores del coche mecánicamente independientes, el controlador podrá mandar cualquier referencia de par a cualquier motor: es decir, el control de par puede ser

cualquiera, y ha de hacerse de forma electrónica. En este apartado se proponen dos controladores, uno a bucle abierto y otro a bucle cerrado.

El controlador a bucle abierto simplemente manda la misma referencia de par a cada motor, que será proporcional a la consigna del conductor (posición del acelerador). Por contra, el controlador a bucle cerrado toma la consigna del conductor como la media entre los pares de las cuatro ruedas, repartiendo el par de forma que el comportamiento del coche se acerque lo máximo posible al deseado por el conductor, sin subviraje ni sobreviraje.

Para ello calcula, a partir de la velocidad del coche y del ángulo del volante el *yaw rate* (derivada del ángulo de guiada) deseado. Este *yaw rate* se controla mediante un PI, cuyo valor da la proporción que se aplicará entre los pares de los ejes delantero y trasero y los pares de las ruedas exteriores e interiores para cada eje.

Se calculó para ambos controladores el gradiente de subviraje (magnitud que cuantifica el subviraje/sobreviraje de un vehículo), resultando tres órdenes e magnitud menor en el caso del controlador PI. A su vez, este controlador demostró también un mejor comportamiento ante una perturbación (paso de suelo seco a mojado).

Conclusiones

En esta tesis se ha tratado sobre vehículos híbridos en tres niveles distintos: desarrollo, modelado y control. Así, el autor participó en el diseo y construcción de los tres coches híbridos con pila de combustible tratados en la tesis, lo que incluye elección de componentes, diseo software e integración.

Respecto al modelado, en esta tesis se presentan modelos relativos a tres aspectos de los vehículos híbridos: sistema de potencia, mecánico y térmico. Los dos últimos, además, se validaron con datos reales.

Por último se disearon dos tipos de controladores para los sistemas mencionados: control del comportamiento del coche y gestor de potencia, donde se probaron varias estrategias de control (heurística, linear, MPC...).

Summary

Introduction

Motivations

Since the wheel was discovered, the road transportation has had a vital role in the history, for the transportation of goods, animals or persons. In the 1880's, Karl Benz patented the first Internal Combustion Engine Vehicles, that will soon become the main tractive system.

Nowadays, the number of cars is continuously increasing, and their emissions suppose a serious problem. The price of petroleum and an increasing environmental concern is making the consumers and the car companies tend to manufacture/buy vehicles with fewer emissions.

However, consumers will not accept any downgrade. Therefore, the cars in the future must be at least as powerful as the current ones, while including new features about safeness and comfort.

Control systems in cars

The invention and development of microprocessors have changed all the technological fields, including the automotive. Nowadays, the cars have kilometres of cables, against the approximately 40 lines that used to be in the fifties, for supplying lights, spark plugs and the starter.

The first milestone in control was the introduction of the injection system in the 1960's. This system optimizes the fuel flow to the engine, increasing the power and the efficiency of the engine. In the seventies Bosch developed the second milestone: the ABS. This system was the first in actuating over the dynamics of the vehicle, avoiding the lock of the wheels. This shortens the braking distance and avoids the lost of control. In the following years hundreds of electronic systems were introduced to the cars: power windows, power lock doors, airbag, etc.

All these systems are controlled by an electronic system, named ECU. Modern cars have usually more than one hundred of these devices, that are responsible for certain works, at different levels. The most important one is the control of the engine (injection, etc). Each ECU reads the sensors related to their work, processes the information and sends the control signal to the actuators. Meanwhile, they can share information with other ECUs to actuate in a coordinate way, or for sharing the data of certain sensors.

Control systems in vehicles can be divided in three groups: systems that do not influence

directly over the dynamics of the vehicle (airbag, power windows), systems that help the driver (ABS) and systems that substitute the driver (autonomous driving). The first and the third ones are out of the field of study if this thesis. Regarding the second one, there are numerous open lines of development. In an ICEV, the controllers actuate over the injection and braking systems. Electric motors make that control easier, due to a better torque control, while in the case of cars with one motor per wheel, the actuation is done directly over each wheel, allowing a better control.

Hybrid cars

A hybrid car is defined as a kind of vehicle with more than one energy source (e.g. gasoline and batteries). Despite the first hybrid car was built more than 100 years ago, they have only been a real option against ICEVs since the Toyota Prius was launched, in 1997. Today, these cars are more common everyday, and almost all the manufacturers include at least one micro-hybrid, with the start-stop system, that stops the engine in case the vehicle is idle. Probably, the strongest trend at the moment is the Plug-in Hybrid Electric Vehicles, that offer the possibility of recharging the batteries from the net.

There are three basic architectures of hybrid vehicles: series, parallel and combined. In the first one the ICE drives a generator, whose electric power is sent to the DC bus, where it is distributed between the tractive motor and the recharge of the batteries. In the parallel configuration, both the ICE and the electric motor are connected to a mechanic system, so both supply mechanical power to the wheels. Finally, in the combined architecture the ICE drives both the generator and the wheels.

Despite fossil fuel and batteries are the most common energy storage sources, all the companies are developing other systems. At the moment, the strongest alternative is the hydrogen. Thus, fuel cells take this fuel and oxygen from the air, generating electric power and water. Considering that hydrogen can be obtained from renewable resources, the fuel cell car emerges as a vehicle that respects the environment and with an unlimited energy source.

Goals of the thesis

The goal of this thesis is to cover the main control problems for three kinds of hybrid vehicles: ICE PHEVs, FCHVs and vehicles with independent motors in each wheel. These cars represent the main automotive trends in the short and middle terms.

Power management in FCHVs

In this chapter, two FCHVs are presented. These vehicles belong to other two projects: Delfín and Hércules, developed with several public corporations and companies. In these projects, several configurations for this kind of vehicles are tested. Besides, a model of the power system is developed and a power management controller are also developed for the vehicle of Project Hércules.

Delfín projects

Projects Delfín I and II are based on a commercial BEV (GEM eL), to which several power devices have been added, becoming a hybrid vehicle.

Delfín I

In Delfín I a 12 kW fuel cell was introduced, as well as a hydrogen storage system and a power converter to couple the fuel cell to the pre-existent power system in the car. Besides, a control system was devloped to control de power fluxes between the devices and give the user an interactive graphical interface.

The vehicle was tested under different driving conditions, concluding that the system could supply the required power in all the circumstances.

Delfín II

Based on the same car as Delfín I, the hydrogen storage system and the electric motor are the only power elements that remain from the first version. The six original batteries were substituted by four gel 12V ones, and the power converter was completely redesigned. The fuel cell was also substituted, in this case by two 1.2 kW stacks.

The control system of the vehicle consists of three controllers operating at different levels. The upper level is devoted to the global power management among the different subsystems of the vehicle. It receives the throttle position as a reference (which means an estimation of the power required by the driver) and sends the power references to the fuel cells controllers and the power converters. The second controller splits the power computed by the upper controller between the two fuel cells, that is the power reference for each one of the fuel cells. Finally, the lower level controllers perform the internal control of the two fuel cells

Experimental tests of this system were performed, demonstrating a good performance of the fuel cells as well as of the power management, satisfying the requirements of the driver.

Project Hércules

Project *Hércules*, and in particular Subproject *El León* consist on the design and set up of the prototype of a FCHV. This is based on the chassis of a *Santana 350*, over which the following power devices are assembled:

- A 56 kW fuel cell and a hydrogen storage system (capacity: 2.4 kg of hydrogen).
- A pack of Li-ion batteries that consists on four modules in series of thirteen 3.7V cells also in series.
- A permanent magnet synchronous motor with a nominal power of 66 kW and a maximum torque of 460 Nm.

The power system of this car was modelled to try different configurations and control strategies. Over this model, a MPC was implemented for the power management. The

inputs of this controller are the required power and the SOC of the batteries, while the manipulated variables are the power references to the different devices: FC, batteries and braking resistance.

The controller penalizes the power required to each source and their rates. On the other hand, the constraints force the devices not to violate their limits and make the controller supply the required power.

This model was extended with the inclusion of a new source of energy: Ultra Capacitors, adapting the controller to this new system. Two new configurations were tested, substituting partially or completely the batteries by the UCs.

Power management of a plug-in hybrid electric vehicle based on cycle energy estimation

In this chapter, a power management control is design for the model of a PHEV. The model was provided by the organizers of a special benchmark session scheduled at E-Cosm 2012. The model included a virtual driver, whose output was the torque required to track the driving cycle. The controller should supply this torque, minimizing the total energy and fuel consumption, with the least possible memory and CPU time resources.

The vehicle has one ICE, two electric motors (motor and generator) and three clutches, allowing four operating modes: one and two-motor pure electric, range extender and power split. The inputs of the controller are the torque request, the maximum regenerative torque, the speed of the car, the SOC of the batteries and an estimation of the total distance and the average speed of the complete cycle. The outputs of the controller are the torque set points for the motors and the engine, the speed of the generator and the state of the three clutches (open/close) and the ICE (on/off).

The proposed controller is divided in two levels. In the highest level, the energy necessary to complete the cycle is estimated. This estimation is based on the approximate data of total distance and average speed. This estimation is being refreshed while the cycle advances. At the same time, the remaining energy in the batteries is calculated, based on the current SOC. With this information the controller calculates the energy that must be supplied by the engine, and will manage the energy of the batteries to allow the engine to work in the most efficient operating point.

The lowest level reads the set points from the highest, and manages the operating modes and the power of each device in the most efficient way, supervising the compliance of the constraints.

Several acceleration tests as well as different driving cycles were simulated in the model. The controller was able to comply with the requirements and constraints, consume few resources, due to its simplicity and specific algorithms to reduce CPU time, minimizing fuel consumption.

The development and validation of a thermal model for the cabin of a vehicle

In a ICEV the heat for the heating system is taken from the refrigeration circuit of the engine, while the compressor of the ACS is coupled to the engine by a clutch. In hybrid and electric cars the ICE (if any) is not always active and the electric motor does not transfer enough heat to supply the heating system. Moreover, it does not need idle speed. Therefore, a new HVAC system is necessary for these kinds of vehicles. The consumption of this device should be considered in the calculation of the global power fluxes. To estimate this consumption, the heat transfer in the air of the cabin of the vehicle should be calculated, and a thermal model of the cabin of the vehicle is necessary.

In this chapter a model for the cabin of a BMW 1 series is presented. For this model some assumptions have been done: the surfaces of the cabin are flat, the thermal inertia in the windows and in the roof are negligible and the only surfaces of the vehicle that transfer heat top the air of the cabin are the windows and the roof.

The air of the cabin transfers heat with:

- Occupants of the car. The transferred heat is found from the values calculated by ASHRAE.
- Internal elements of the vehicle. These are modelled as a surface with a certain thermal inertia. This inertia was estimated with experimental tests. It is assumed that the solar irradiation that enters the cabin hits on this surface.
- The external air (mass flow due to leaks and ventilation).
- Convective heat transfer with the internal surfaces of the roof and the windows.

The heat flux in the walls of the cabin is calculated using theoretical thermal equations and experimental correlations, considering the solar irradiation, the external convection, the conduction and finally, the internal convection.

A temperature sensor network was installed in a real vehicle to validate the model, doing three kinds of tests: empty car parked indoors, empty car parked outdoors and car with one occupant moving outdoors. The similarity between the experimental results and the simulations makes the model valid.

Power management in hybrid vehicles with HVAC

In this chapter the thermal model of the cabin of a vehicle is used to calculate the influence of the HVAC system over a hybrid car. With this aim, this model is included in the model of the power system of the vehicle in study.

Air conditioning model

The thermal model cannot be introduced directly. It is necessary to include a HVAC model between the thermal and the power system models, that calculates the power of the

compressor from the heat transference to the air of the cabin. The model of the cabin has been improved, adding the calculations of humidity and latent heat.

The model of the HVAC calculates this power usin the specifications of the own HVAC system (nominal power and nominal COP) and several corrective factors, that consider the influence of working in an non nominal operating point.

Integration and results

Both the models of the cabin and of the ACS were integrated in the power system models of two HVs, of different kinds and with different sources of energy. On one hand, they were included in the model of a BMW 1 series FCHV with the MPC control presented in Chapter 2. Several simulations were run, with different weather conditions, number of occupants and initial SOC, for a urban (FUDS) and a highway (ARTEMIS highway) driving cycles.

In the same manner, the thermal+HVAC models were integrated in the PHEV model described in Chapter 3 where several simulations were run, for different weather conditions and number of occupants, for the same cycles as the previous vehicle.

The same simulations were also run with the air conditioning system disconnected. Comparing the results, it is concluded that the ACS generates an increase in the global fuel consumption of about 3 to 9%, except in the urban cycle for the PHEV in which it reaches up to 35%.

Modelling and torque distribution control for a four in-wheel independent driving electric vehicle

Vehicle description

In this chapter, the vehicle FOX is introduced. This car is made as a test bench for different power management and torque distribution controllers. The FOX vehicle is based on the chassis of the Silver Car S2 racing car. It was slightly modified for the best fitting of the new elements and for adding a second seat. Four in-wheel motors, 7 kW each, have been installed as well as their respective controllers and power converters. These motors are fed by six LiFeMnPO4 battery modules, 12.8V and 100Ah each. Two more sources of energy will be added in the future: a fuel cell and a UC module.

The vehicle includes several sensor with two main aims: measure the position of the devices of the driver and the behaviour of the car. For the first aim three potentiometers that measure the position of the throttle and brake pedals as well as the angle of the steering wheel. For the second, four potentiometers are used to measure the of the suspensions, an IMU to measure the accelerations and rotational speeds and a GPS, included in the IMU (location and speed). This information is completed with the data transmitted by the controllers of the batteries (SOC, voltage, current) and the wheels (current, rpm).

CAD model

A CAD model was developed for this vehicle, using the software tool *Solidworks*. This design was based in the model of the chassis provided by the manufacturer. This model

has been completed with the new elements: suspension, steering, power devices and the models of two occupants. Two variants were made for the front suspension and the steering system. The simpler one assumes that the contact point between the road and the tyre is in the center of the tread, and a second variant, more similar to the real system. The CAD model will be ported to two simulation programs: *ADAMS/ADAMS Car* and *Matlab Simulink-Simmechanics*, using the complex and the simple variants respectively.

Simulink-Simmechanics model

The *Solidworks* model was ported to *Matlab Simulink-Simmechanics* with the *Simmechanics-link* tool. In Simmechanics all the solids of the CAD model are defined (bodies) as well as the joints between them.

On the contrary, the interaction between the ground and the tyre is not modelled directly, so it becomes necessary to create a new subsystem that calculates these forces. For this aim the Burckhardt tyre model was used. This model calculates the forces as a function of the slip and the slip angle.

For the steering system, an Ackermann configuration was assumed, based on the measurements of the real system.

Th model was validated comparing the trajectory of the simulated system with real trajectories in the same conditions, for rear wheel drive and 4WD.

Torque distribution controllers

The four in-wheel motors are mechanically independent. Therefore, it is possible to send any torque set point to any motor. Consequently, a controller should be developed in order to distribute the torque set points in a logical manner. In this section two controllers are proposed: open-loop and a closed-loop.

The open-loop controller sends the same torque reference to the four motors. This referencia is proportional to the travel of the throttle pedal. On the contrary, the closed-loop controller takes the set point of the driver as the average torque of the four wheels, distributing the torque in a manner for the behaviour of the car to be the closest possible to the wishes of the driver.

Se calculó para ambos controladores el gradiente de subviraje (magnitud que cuantifica el subviraje/sobreviraje de un vehículo), resultando tres órdenes e magnitud menor en el caso del controlador PI. A su vez, este controlador demostró también un mejor comportamiento ante una perturbación (paso de suelo seco a mojado).

To quantify the under/oversteering of the vehicle, the understeer gradient was calculated for both controllers. This gradient is three orders of magnitude smaller in the case of the closed-loop controller. Besides, the vehicle had a better performance against a disturbance (dry to wet road) with this controller.

Conclusiones

This thesis deals with HVs in three levels: **development, modelling and control**. Thus, the author was in involved in the design and set up of the three FCHVs mentioned in this thesis. It includes election of components, software design and physical integration.

Regarding modelling, three kinds of models have been implemented in this thesis, involving HVs: power system, mechanical and thermal. The latter two were also validated with real data.

Finally, two kind of controllers were designed for the mentioned systems: car performance and power management controllers, where different control strategies were used (heuristic, linear, MPC...).